

WASHINGTON UNIVERSITY IN ST. LOUIS

Department of Physics

Dissertation Examination Committee:

Lee Sobotka, Chair

Robert Charity

Willem Dickhoff

Joseph A. O'Sullivan

Martin Israel

OXYGEN ISOTOPES BEYOND THE PROTON DRIP LINE

by

Tyler Bryant Webb

A dissertation presented to the
Graduate School of Arts and Sciences
of Washington University in
partial fulfillment of the
requirements for the degree
of Doctor of Philosophy

September 25, 2019

Saint Louis, Missouri

©2019, Tyler B Webb

Contents

List of Figures	v
List of Tables	xv
Acknowledgements	xvii
1 Introduction	1
1.1 The Chart of the Nuclides and Stability	1
1.2 Nuclear Structure	3
1.2.1 Nuclear Masses	3
1.2.2 The Independent Particle Model	3
1.2.3 Isospin	6
1.3 $2p$ Decay	8
1.3.1 Proton Decay	8
1.3.2 Decay Correlations	9
1.4 Proton Therapy for Radiation Oncology	11
1.4.1 Fundamentals of Radiation Therapy	11
1.4.2 The Bragg Peak and Stopping Power	11
1.4.3 Fundamentals of CT Imaging	14
2 Experimental Methods	17
2.1 Overview	17

2.2	The Invariant-Mass Method	18
2.3	The High Resolution Array	20
2.3.1	The Silicons (ΔE)	22
2.3.2	The Scintillators (E)	25
2.3.3	Detector Calibration	25
3	^{11}Li	29
3.1	Overview	29
3.2	Ground State Structure	32
3.3	Excited States	32
4	^{11}O	34
4.1	Introduction	34
4.2	Decay Energy Spectrum and Contamination	35
4.3	Single State Fit	38
4.4	Theoretical Model	38
4.4.1	The Gamow Coupled Channel (GCC) Model	38
4.4.2	The Three-Body Gamow Coupled Channel (GCC) Model	40
4.4.3	The GCC Applied to ^{11}O	40
4.5	Results	42
4.6	Dinucleon Correlations	49
4.7	Conclusions	49
5	^{12}O	53
5.1	Introduction	53
5.2	^{12}O Structure	54
5.2.1	Calibration resonances	54
5.2.2	$2p + ^{10}\text{C}$ channel	56
5.2.3	$4p + 2\alpha$ channel	57

5.3	Momentum Correlations	61
5.4	Comparison to GCC predictions	69
6	$^{11,12}\text{N}$	71
6.1	Introduction	71
6.2	^{11}N Structure	73
6.2.1	$p+^{10}\text{C}$ spectrum	73
6.2.2	^{11}N ground state	74
6.3	^{12}N structure	77
6.3.1	$2p+^{10}\text{B}$ channel	77
6.3.2	$2p+\alpha+^6\text{Li}$ channel	80
6.3.3	$3p+^9\text{Be}$ channel	82
6.4	Analog States	84
7	^{10}N	88
7.1	Introduction	88
7.2	Invariant-mass Spectra	89
7.3	Discussion	92
8	Experimental Verification of the JSIR-BVM Approach for Computing Proton Stopping Power Ratios	96
8.1	Background	96
8.1.1	Goals	96
8.1.2	The JSIR-BVM	97
8.1.3	The BVM for Computing Proton SPR	99
8.2	Experimental Methods	100
8.2.1	CT Experiment	100
8.2.2	Proton Experiment	102
8.3	Analysis and Results	104

8.4 Conclusions	109
9 Conclusion	110
Appendix Glossary	112
Bibliography	113

List of Figures

1.1	The chart of the nuclides. Stable nuclei are shown as black squares. Proton number increases to the top, neutron number increases to the right.	2
1.2	The Woods-Saxon potential for neutrons (left) and protons (right) in ^{114}Sn . Note the Coulomb barrier for the proton potential.	4
1.3	A summary of the single-particle levels for the IPM with different potentials. The right-most set of levels correspond to the Woods-Saxon potential with spin-orbit coupling included.	5
1.4	Levels in ^{11}Li and its isobaric neighbor ^{11}Be . The isobaric analog states in the two nuclei are connected by the dashed line. Taken from [1].	7
1.5	The various types of $2p$ decay. (a) and (c) show direct $2p$ decay, b(b) shows sequential $2p$ decay, and (d) and (e) show “democratic” $2p$ decay. Taken from [2].	9
1.6	The Jacobi “T” and “Y” systems. Taken from [3].	10
1.7	A summary of the results of double-strand breaks due to external radiation in the nucleus of a cell. The cell can repair the break, or chromosomal anomalies can occur, which can cause cell death upon division. The cell could even undergo direct apoptosis as a result of the break. Taken from [4].	12
1.8	A dose-depth curve for protons. Note the prominent Bragg peak right before the end of the protons’ range. Taken from [5].	13

1.9	The fundamentals of a 3rd generation CT scanner. The x-ray tube and detector array rotate around the patient. Combining the signal seen in a detector with knowledge of the angle of the source-detector pair's rotation and the index of the detector allows a cross-sectional image of the patient to be reconstructed. Taken from [6]	15
1.10	An object and its sinogram. Taken from [7].	16
2.1	Schematic of the experimental setup. The stable ^{16}O beam (black) is accelerated by the K500 and K1200 coupled cyclotrons. It then impinges on a ^9Be target, fragmenting. The fragments produced are then separated by the A1900 magnetic separator by their charge-to-mass ratio. The radioactive ^{13}O beam (red) then passes through the radio frequency fragment separator (RFFS), which increases the purity from 10% to more than 80%. The beam is then transported to the experimental area, where it bombards a ^9Be secondary target, creating unbound decay products which are detected by HiRA.	18
2.2	(a) A zoomed-view of a $\Delta E - E$ plot used for particle identification. The three large bands at the left of the plot are the $^{1,2,3}\text{H}$. The two bands seen at the upper right are $^{3,4}\text{He}$. (b) A zoomed-in view of the carbon band. The small bands represent different isotopes of carbon.	21
2.3	The HiRA array. Note the Mylar shielding in front of the Si detectors, the cooling bars affixed to the back of the telescopes, and the copper mouthpiece at the center of the array.	23
2.4	A cartoon showing what is inside each of the 14 canisters that make up HiRA. A double-sided, segmented silicon detector is backed by 4 CsI(Tl) scintillators. The $65\ \mu\text{m}$ single-sided silicon detector shown in this figure was not used for this experiment.	24
2.5	A calibrated alpha spectrum for a typical silicon front (hole collecting) strip. The observed peaks are those given in Table 2.1	27

2.6	Pulser calibration for a typical silicon strip on the front of the detector. The data shown are taken from the low-gain channel. The pulses are in uniform increments of charge, and a non-linearity above half scale is clearly seen. The large peak in the center of the spectrum corresponds to a pulse run for twice as long as the other pulses.	28
3.1	The interlocking Borromean rings from which Borromean nuclei take their name. The Borromean rings are named for the aristocratic Borromeo family, the owners of three islands in Lake Maggiore.	30
3.2	The rms matter radius R_{rms}^r for He, Li, Be, and C for varying mass numbers. Taken from [8].	31
3.3	Levels and particle-decay thresholds for ^{11}Li . Taken from Ref. [9].	33
4.1	Total decay energy spectrum for the $2p$ decay of ^{11}O events. The black curve is generated from detected $2p$ and ^9C fragments, while the red and blue curves show contamination from $2p$ -decaying ^{12}O and ^{13}O nuclei respectively. This contamination is caused by heavier isotopes of carbon leaking into the ^9C gate. There is no transverse gate applied.	35
4.2	A detail of a $\Delta E - E$ plot created during a with the ^9C calibration beam. Notice the streaking heading off to the left. This is due to reactions in the CsI(Tl), the source of the contamination in the invariant mass spectrum of ^{11}O	36
4.3	The total decay energy spectrum for ^{11}O with the contamination removed. Shown on the same plot are theoretical predictions for the decay energy of the nucleus. No transverse gate is applied.	37
4.4	A fit to the decay energy spectrum of ^{11}O assuming the peak is created by the decay of a single state in ^{11}O . The curve is generated by Monte-Carlo simulations incorporating the detector response. The dashed line is a fitted background. No transverse gate is applied.	39

4.5	A fit to the ^{11}O decay energy spectrum assuming that the peak consists of two $3/2^-$ states. No transverse gate is applied.	43
4.6	A fit to the ^{11}O decay energy spectrum assuming that the peak consists of four states, two of $J^\pi = 3/2$ and two of $J^\pi = 5/2$. No transverse gate is applied.	45
4.7	(a) The IMME curve obtained by fitting the three neutron members of the $A = 11$, $T = 5/2$ sextet and the masses of the four known members and (b) the residuals of these masses with the curve. The mass for ^{11}O is taken from the first $J^\pi = 3/2^-$ level of the GCC calculation that reproduced the fit.	46
4.8	A fit to the ^{11}O decay energy spectrum (a) with no transverse gate and (b) for events decaying transversely to the beam ($\cos\theta_C < 0.2$). There is a clear enhancement of a high-lying feature relative to the spectrum that includes all events. This feature appears to sit at the energy of the second $5/2^+$ state.	47
4.9	(a) Predicted widths for the $3/2_1^-$ (both solutions) and $3/2_2^-$ resonant states of ^{11}O as a function of Q_{2p} . The arrows indicate the predicted Q_{2p} values of the $3/2_1^-$ and $3/2_2^-$ states. (b) GCC configuration weights (real parts of squared norms) of the $(s_{1/2})^2$ and $(Sl_x l_y) = (000)$ configurations in the $3/2_1^-$ wave function.	50
4.10	Two-nucleon density distributions (in fm^{-2}) in Jacobi coordinates predicted in GCC for low-lying resonant states in ^{11}O (left) and ^{11}Li (right).	51

5.1	<p>Excitation-energy spectra of calibration peaks for (a) the first $2p$-decaying levels of ^{13}O and (b) the first two excited states of ^{12}N reconstructed from transversely decaying $2p+^{11}\text{C}$ and $p+^{11}\text{C}$ events respectively. The red solid curves show the results of Monte Carlo simulations incorporating the detector response and known level properties. The blue dashed curves are fitted estimations of the background. Total decay energy spectra (c),(d) of ^{12}O reconstructed from transversely decaying $2p+^{10}\text{C}$ events. (c) shows a fit at the upper limit of the uncertainty for the 0_2^+ width while (d) shows the fit at the lower limit. The red solid curve shows the summed results of Monte-Carlo simulations of each resonance, shown by the solid green curves. The blue dashed curve shows the fitted background. A $\cos\theta_C < 0.2$ gate was applied for all spectra.</p>	55
5.2	<p>(a) Total decay energy spectrum reconstructed from coincident $4p+2\alpha$ events. The red solid curve shows the result of a Monte-Carlo simulation with a Breit-Wigner intrinsic line shape. The blue dashed curve shows the fitted background. (b) Coincident $4p+2\alpha$ events with a gate on and a gate vetoing $^8\text{Be}_{g.s.}$ intermediate states, and (c) the multiplicity of observed intermediate resonances assessed at five different points along the spectrum. Also included is the probability of observing a $^6\text{Be}_{g.s.}+^6\text{Be}_{g.s.}$ fission event. No $\cos\theta_C$ gate was employed.</p>	58
5.3	<p>Invariant-mass spectra showing intermediate states present in the $4p+2\alpha$ channel. (a) shows the correlation of the E_T values of two ^6Be's that can be reconstructed from the six detected particles. If the diagonal gate indicated by the dotted lines is applied, the projection on either one of the axes is shown in (b). (c) and (d) show invariant-mass spectra for $4p+\alpha$ and $2p+2\alpha$ subevents. The arrows label the peaks associated with known levels. No $\cos\theta_C$ gate was employed.</p>	60

5.4	Experimental momentum correlation plots for the ground-state $2p$ decays of ${}^6\text{Be}$, ${}^{12}\text{O}$, and ${}^{16}\text{Ne}$. Results are shown in both the Jacobi T (upper panels) and Jacobi Y (lower panels) representations. The ${}^{12}\text{O}$ data is from this work while the ${}^6\text{Be}$ and ${}^{16}\text{Ne}$ data are from Refs. [10, 11].	62
5.5	Projections of the (a) Jacobi T and (b) Jacobi Y 2D distributions on the energy axis. Ground-state $2p$ emitters are plotted as histograms while $2p$ emission from isobaric analogs is plotted as the data points.	63
5.6	Jacobi Y momentum correlations for E_T bins centered on (a) 0_1^+ , (b) 2_1^+ , and (c) 2_2^+ states. The 2_1^+ results in (b) contained contributions from the shoulder state. The energy gates for the spectra are $1.43 < E_T < 2.02$ MeV for (a), $3.45 < E_T < 4.04$ MeV for (a), and $5.85 < E_T < 6.06$ MeV for (c).	65
5.7	(a) Experimental 2D momentum correlations of the 2_2^+ state of ${}^{12}\text{O}$, and simulated momentum correlations of sequential decay through (b) a combination of the $\frac{1}{2}^-$ and $\frac{3}{2}^-$ second and fifth excited states of ${}^{11}\text{N}$, (c) the $\frac{1}{2}^-$ states alone, and (d) the $\frac{3}{2}^-$ state alone. The dashed lines show the expected ridgelines when decaying through the $3/2^-$ state, while the solid lines indicate the ridgelines expected when decaying through the $1/2^+$ state.	67
5.8	Efficiency-corrected projection of the Jacobi Y correlation plot for the 2_2^+ ${}^{12}\text{O}$ state on the $\cos\theta_k$ axis. Results are shown for (square data points) for a tight gate on the invariant-mass peak and for background gates on either side of this peak (triangles and open circles). An axis showing the relative angle θ_{pp} between the protons is also included.	68

6.1	Levels of interest in the $1p$ decay of ^{11}N states, $2p$ decay of ^{12}O states, and their analogs in ^{12}N . Green arrows show γ -ray decays of importance, while observed $1p$ decays are shown as the straight blue arrows. The dashed curves show possible sequential decay paths of ^{12}O states investigated in this work. The curved blue arrows indicate direct $2p$ decay. The 0_2^+ ^{12}O state from [12] is also shown.	72
6.2	$p+^{10}\text{C}$ invariant-mass spectra. (a) The raw spectrum is shown by the black histogram. The red and blue histograms show estimates of the contamination from $p+^{11}\text{C}$ events where the ^{11}C fragment was misidentified as a ^{10}C and from $^{12}\text{O}\rightarrow 2p+^{10}\text{C}$ events where one of the protons was not detected. (b) Fit to the contamination-subtracted spectrum with known ^{11}N peaks in ENSDF indicated by the labeled black arrows and new peaks by the unlabeled red arrows. The fitted peaks for individual levels are shown as the dotted black curves, while the blue dashed curve is the fitted background. A $ \cos\theta_C < 0.5$ gate was applied for all spectra.	75
6.3	Jacobi projections of experimental (black dots) and simulated (solid curves) of sequential decays through $^{11}\text{N}_{g.s.}$ where $\cos\theta_k > 0.5$. The different colored curves in (a) correspond to the different literature parameters given in Table 6.2. The red solid curve in (b) corresponds to a new fit to the data. The parameters for this new fit are also given in Table 6.2. The pink dashed curve corresponds to the fitted background, and the solid green curve corresponds to the total fit after subtraction of the background.	76
6.4	Comparison of invariant-mass spectra for the (a) $2p+^{10}\text{C}$ and (b) $2p+^{10}\text{B}$ exit channels. Fits using Breit-Wigner intrinsic line shapes are shown by the curves in both panels. A $ \cos\theta_C < 0.2$ gate was applied for both spectra. . .	79

6.5	The upper panels show (a) $2p+\alpha$ and (b) $2p+{}^6\text{Li}$ invariant-mass spectra for these subevents. No $\cos\theta_C$ gate was applied. (c,d) show invariant-mass spectra obtained from the $2p+\alpha+{}^6\text{Li}$ events gated on the ${}^6\text{Be}_{g,s}$ and ${}^8\text{B}_{IAS}$ invariant-mass peaks in (a) and (b), respectively. The curves in (c,d) are fits assuming a single Breit-Wigner lineshape.	81
6.6	(a) The multiplicity of the low-energy peak in (c) as a function of excitation energy. The dashed blue curve is a smooth fit to the data points beyond the observed ${}^{12}\text{N}$ peak in (b), the experimental $3p+{}^9\text{Be}$ invariant-mass spectrum with a fit assuming a single Breit-Wigner level and smooth background (blue dashed curve). (c) Invariant-mass spectrum obtained from the $p+{}^9\text{Be}$ subevents. The energies of known ${}^{10}\text{B}$ levels are indicated. A $ \cos\theta_C < 0.5$ gate was applied to both spectra.	83
6.7	Level schemes for $A = 12$ and $T=2$ states with excitation energy plotted relative to the first $J^\pi=0^+$ state. The results for ${}^{12}\text{O}$ and ${}^{12}\text{N}$ are from this work, the ${}^{12}\text{B}$ levels are from [13], and the ${}^{12}\text{Be}$ levels from [14, 15].	85
6.8	(a) Mass excesses of three lowest $A=12$ quintets as a function of isospin projection T_Z . The curve through the data points are fits with the quadratic IMME [Eq. (6.1)]. (b) Deviations from the IMME fit for the lowest quintets. The results for the 2^+ states have been shifted up along the Y -axis for clarity. The statistical and systematic errors for the ${}^{12}\text{O}$ and ${}^{12}\text{N}$ data points from this work are of similar magnitude. We have combined them in quadrature for these fits.	86

7.1	(a) Raw experimental $p+{}^9\text{C}$ invariant-mass distribution (black) and the estimated contamination from $p+{}^{10}\text{C}$ and $p+{}^{11}\text{C}$ events where the carbon fragment was misidentified as ${}^9\text{C}$. The contamination from ${}^{11}\text{O}\rightarrow 2p+{}^9\text{C}$ events where only one of the two protons is detected is also shown. (b,c) Contamination-subtracted spectrum (data points) with two-level fits (solid red curve). The contribution from each level is shown as the dotted curves while the fitted smooth background is shown as the blue-dashed curve. The fits are shown for ground-state lineshapes expected for (b) a $J^\pi=1^-$ level or (c) a $J^\pi=2^-$ level.	90
7.2	Excitation function for ${}^9\text{C}+p$ resonance elastic scattering. Data is from Ref. [16]. The black solid curve is the best R-matrix fit from Ref. [16] that was obtained using 2^- g.s. and 1^- excited state spin-parity assignment for the two broad s-wave resonances. (The $1^-/2^-$ solution is almost identical, so it is not shown). The red dashed curve is the 2^- ground state and 1^- excited state and the blue dotted curve is the 1^- ground state and 2^- excited state, but with parameters for the excited state taken from the invariant mass fit (Table 7.1).	93
8.1	A front-view image of the bottles containing the three soft tissue surrogates in their scan geometry. The x-ray source is above the bottles out of the frame, and the detector array is below out of the frame.	101
8.2	The setup used for the proton stopping power measurements. The water tank is on the left, with the the ion chamber apparatus near the right wall. The sample is sandwiched between where the blockers are placed and the water tank.	103
8.3	A reconstructed proton SPR map of the alcohol samples. The z-axis is the reconstructed proton SPR.	104

8.4	Normalized data taken using the setup shown in Fig. 8.2 for three different samples, denoted by the colored curves. The location of the Bragg peak clearly shifts between samples, moving closer to the proton source as the stopping power of the materials increase.	105
8.5	The WEPL discrepancy between the reconstructed SPR images and the SPR measured using the proton therapy machine for (a) the two highest-density bony tissue surrogates, (b) the two lower-density bony tissue surrogates, and (c) the three soft tissue surrogates.	107
8.6	The WEPL discrepancy between the reconstructed SPR images and the theoretical SPR for (a) the two highest-density bony tissue surrogates, (b) the two lower-density bony tissue surrogates, and (c) the three soft tissue surrogates.	108

List of Tables

2.1	The alpha energies, half-lives, and branching ratios for the ^{232}U decay chain. α particles with under 5% intensity are not included. α_0 and α_1 are the decays to the ground and first-excited state of the daughter.	26
3.1	A short summary of recent mass measurements and the two neutron separation energy of ^{11}Li	30
3.2	The excited states of ^{11}Li	33
4.1	The decay energies, Q_{2p} , and widths, Γ , of the four lowest-lying resonant states of ^{11}O	44
5.1	Comparison of fitted and literature decay energies and widths of calibration resonances used for detector characterization. Literature values for ^{12}N states come from [17] and values for ^{13}O states from [18].	54
5.2	The spin assignments, decay energies, intrinsic widths, and measured cross sections of the four observed states in ^{12}O	56
5.3	Decay energies for prompt $2p$ emitters in Fig. 5.5.	63
5.4	Structure of the the first third 2^+ states predicted with the Gamow coupled-channel approach [19]	69
6.1	Level parameters obtained from the fit to the $p+^{10}\text{C}$ invariant-mass spectrum of Fig. 6.2(b).	74

6.2	Decay energies and widths reported in the literature and in this work for the proton-decaying $1/2^+$ ground state of ^{11}N	77
6.3	Fitted parameters for ^{12}N states observed in the $2p+^{10}\text{B}$ invariant-mass spectrum of Fig. 6.4(b), the $2p+\alpha+^6\text{Li}$ spectra in Figs. 6.5(c) and 6.5(d), and the $3p+^9\text{Be}$ spectrum in Fig. 6.6.	78
7.1	Fitted R -matrix parameters for the 1^- and 2^- state with the two energy orderings. The centroid and width of the states calculated from the pole ($E_{pole} - i\frac{\Gamma_{pole}}{2}$) of the S -matrix are also shown.	94
7.2	Systematics for splitting due to interaction between a $2s_{1/2}$ -shell valence proton(neutron) with a $1p_{3/2}$ -shell unpaired neutron(proton) in light nuclei. . .	94
8.1	A summary of the properties of the aqueous solutions used in these experiments.	102
8.2	The reconstructed properties of the tissue surrogates and a comparison of the theoretical, the reconstructed, and the directly measured SPR.	105
8.3	The means of the WEPL distributions shown in Figs 8.5 and 8.6. They are very near zero.	109

Acknowledgements

I would like to thank my thesis advisor, Lee G. Sobotka, who has instructed, collaborated with, and supported me during my time at Washington University. I also thank Bob Charity, my closest mentor during the analysis presented in this work. I give special thanks to Kyle Brown, who, as a student at WUSTL and then a postdoc (and now assistant professor!) at MSU, has been an extremely valued collaborator, mentor, and friend, without whom this work would have been much more difficult. I thank the rest of my thesis committee, Willem Dickhoff, Joseph O’Sullivan, Marty Israel, and Bob again, for their feedback on this document.

I thank my collaborators at Michigan State University from the HiRA and Nazarewicz groups, especially Simin Wang. I also thank collaborators in the Wuosmaa group at the University of Connecticut. I also thank my collaborators on the medical physics work presented in this thesis including Ruirui Liu, Maria Medrano, Shuangyue Zhang, Mariela Porrás-Chaverri, Dave Politte, Jeffrey Williamson, Bruce Whiting, and Joseph O’Sullivan (again).

I thank my undergraduate advisors, Todd Tinsley and Damon Spayde. Their excitement for fundamental physics and skill in explicating the concepts therein are a large reason why I pursued this degree.

I have made valued friends in the Radiochemistry and Physics buildings at Wash U: Jordan Russell, Quin Abarr, Mack Atkinson, Nathan Walsh, Cole Pruitt, Dan Mulrow, Augusto Medeiros, Brendan Haas, and Dan Hoff. Thank you for making my time in these

old buildings far more enriching (and sometimes less productive) than it might have otherwise been.

I thank my friends away from campus, both within and outside St. Louis: Wil Chandler, Austin Rowe, Noah Johnston, Ryan Parker, Hannah Trout, Jesse Thomason, Kevin Seltzer, Jessica Maginity, Colton Faull, Kaylon Buckley, Kim Sukhum, Emily Russell, and Janie Walsh. Without your friendships, local or remote, my life would be far less rich and completing my degree would have been much harder.

I owe a great deal of thanks to my parents, Joe and Lisa Webb. Thank you for all your advice, encouragement, and steadfast, resolute support during these five years and the 22 preceding them. Your guidance and encouragement have been indispensable.

And finally, Lauren Williams. No thanks could be big enough.

Abstract

In this work, the decay of two proton-rich isotopes of oxygen, $^{11,12}\text{O}$ was studied. The structure of these nuclei was investigated by measurement of the decay energy, intrinsic width, and momentum correlations between decay fragments. The ground and low-lying excited states of ^{12}O were measured, including a newly observed 2^+ excited state. This work marks the first observation of ^{11}O . I also present the observation of analog states of ^{12}O in ^{12}N . These states decay by emission of one or two protons, and they were populated by knockout reactions of a ^{13}O beam produced by the coupled cyclotrons at the National Superconducting Cyclotron Laboratory. The decay fragments were detected in the High Resolution Array (HiRA), an array of 14 Si-CsI(Tl) telescopes. I also present work on the experimental verification of a sinogram-based iterative reconstruction of proton stopping power ratios from CT data.

Chapter 1

Introduction

1.1 The Chart of the Nuclides and Stability

Nuclear species are characterized by their proton number (Z) and neutron number (N). Figure 1.1 shows the chart of the nuclides, the standard way of displaying nuclear species according to their number of protons and neutrons. The black squares in the figure are stable nuclei, which, for light nuclei, usually have equal proton and neutron numbers. As the mass number ($A = N+Z$) increases, the Coulomb repulsion of the protons increases, and stable nuclei become more neutron-rich. This tendency toward neutron-richness as mass increases is opposed by the nuclear asymmetry energy

$$E_{asy} \propto \frac{(N - Z)^2}{A} \quad (1.1)$$

driving stability toward $N = Z$. Off stability are beta-unstable nuclei (the pink and blue squares on Fig. 1.1) which, when created, undergo radioactive decay back to stability. The further a nucleus is from stability, the shorter its beta-decay half-life, generally speaking. Similarly, the binding energy of the last proton (neutron) decreases as one looks further to the left (right) of the valley of stability. When far enough away from stability, the binding energy of the last nucleon goes to zero. The point where this occurs is known as the drip

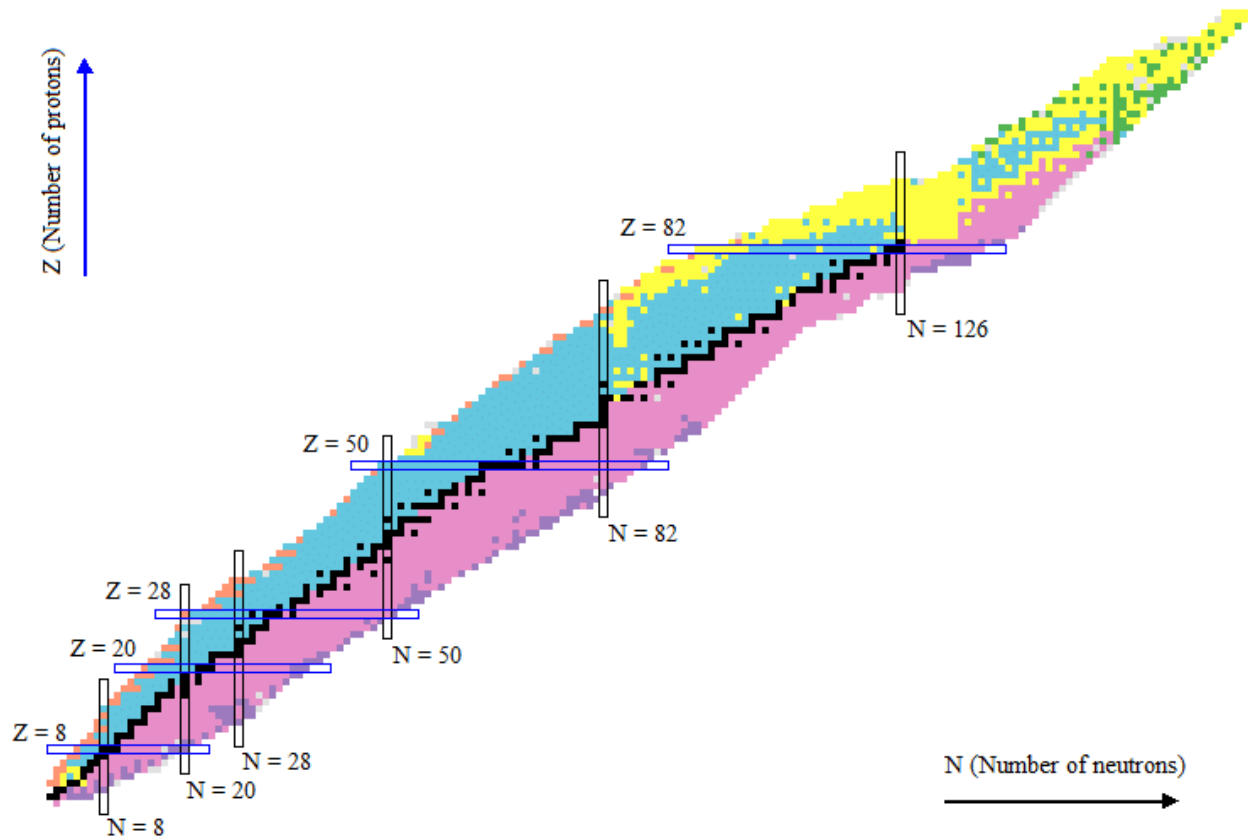


Figure 1.1: The chart of the nuclides. Stable nuclei are shown as black squares. Proton number increases to the top, neutron number increases to the right.

line. Nuclei beyond the drip line (the purple and orange squares on Fig. 1.1) are short-lived and decay by emitting one or more nucleons. The yellow and green squares on Fig. 1.1 are nuclei that decay through alpha emission and spontaneous fission respectively.

Unstable nuclei with short half-lives must be produced in the laboratory. Nuclei near stability can be produced by knockout and transfer reactions. Nuclei far from stability, like the nuclei beyond the proton drip line that are discussed in this work, can be produced via a two-step process. A stable nuclear species can undergo knockout reactions which create bound, beta-unstable nuclei. These nuclei then undergo additional knockout reactions to produce very short-lived exotic nuclei far from stability.

1.2 Nuclear Structure

1.2.1 Nuclear Masses

Nuclear mass is the arbiter of nuclear stability. It is the systematic reduction of nuclear mass through radioactive decay that leads to the valley of stability occupied by the black squares in Fig. 1.1. Therefore, it is perhaps useful to have a model of the nucleus that can predict the mass or binding energy of a nucleus. Such a model exists and is known as the Droplet-Model (DM), introduced in 1935 by Carl Friedrich von Weizsäcker [20]. The DM is macroscopic and does not attempt to quantum mechanically describe the nucleus. It begins with a term that describes the bulk properties of nuclear matter and then applies a series of corrective terms. These corrections include a surface correction (as nucleons on the surface are not exposed to the attractive force from all sides), a Coulomb correction (as the protons of a nucleus repel each other), and a correction for any proton/neutron asymmetry, as mentioned earlier. There is also a term which accounts for the pairing of neutrons and protons. The binding energy ($B(Z, A)$) given by the DM is as follows:

$$B(Z, A) = C_1 A - C_2 A^{2/3} - C_3 \frac{Z^2}{A^{1/3}} \left(1 - \frac{C_4}{C_3} A^{-2/3}\right) - C_1 k \frac{(N - Z)^2}{A} \left(1 - \frac{C_2}{C_1} A^{-1/3}\right) + \delta \quad (1.2)$$

In order, the terms are the volume term, the surface correction, the Coulomb correction, the asymmetry correction, and the pairing term. This model reproduces the binding energies of stable nuclei all across the chart of the nuclides (Fig. 1.1). It provides less insight into the quantum mechanical structure of nuclei than we might wish, however.

1.2.2 The Independent Particle Model

The quantum mechanical structure of the atom is made up of irregularly-spaced single-particle energy levels that electrons fill according to the aufbau rule. Atoms have a shell structure, in which closed shells confer extra stability, exemplified by the inert nature of

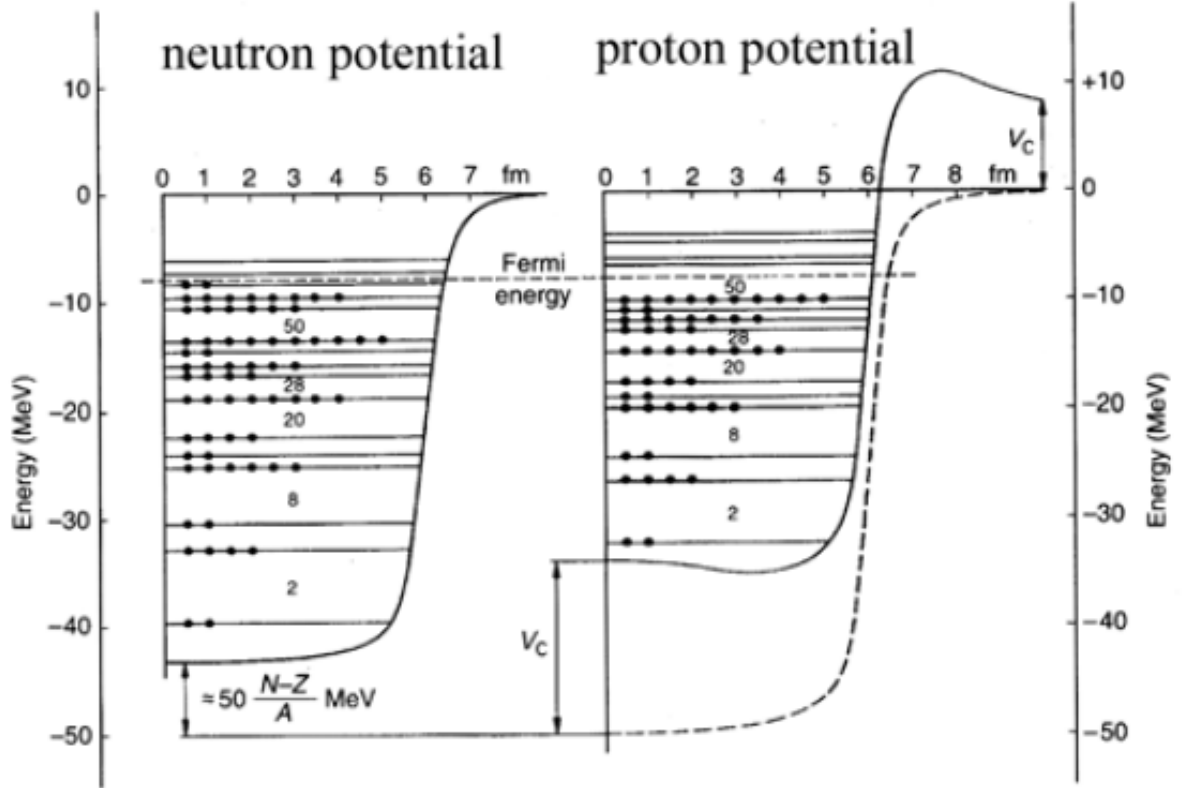


Figure 1.2: The Woods-Saxon potential for neutrons (left) and protons (right) in ^{114}Sn . Note the Coulomb barrier for the proton potential.

the noble gases. While the nuclear problem is more spatially compact, defined by a nuclear interaction different than the Coulomb interaction, and features two types of fermions (as opposed to a single type, the electron), there exists experimental evidence for shell structure of nuclei. The evidence points to so-called “magic numbers”, with there being large natural abundances of isotopes and elements with Z_{magic} and N_{magic} . These numbers are $Z_{magic} = N_{magic} = 2, 8, 20, 28, 50,$ and $82,$ and $N_{magic} = 126$. Other observable quantities display strange discontinuities near magic numbers, including drops in single-nucleon separation energies for $Z_{magic+1}/N_{magic+1}$ relative to the neighboring magic isotone/isotope, and drastic decreases in the thermal neutron capture cross-section for N_{magic} nuclei. The presence of these “magic numbers” suggests a nuclear shell structure.

The most common quantum mechanical description of the nucleus which satisfies this shell structure is known as the independent-particle model (IPM). A mean-field theory, the

IPM treats each nucleon a single-particle subject to an average potential created by all the other nucleons in the nucleus. This potential is a rounded square well known as the Woods-Saxon potential, with a Coulomb interaction included for the protons in the nucleus. This potential is shown in Fig. 1.2. This potential produces unevenly-spaced single-particle levels analogous to the atomic problem. The addition of spin-orbit coupling produces the large gaps in energy at the magic numbers, describing the shell structure observed experimentally. Figure 1.3 provides a nice summary.

1.2.3 Isospin

Isospin, represented as T , is a quantum number related to the strong nuclear force. Isospin is so named because it obeys the same algebraic rules as angular momentum and spin. Bare nucleons have $t=1/2$, with projections of $t_Z=-1/2$ and $t_Z=+1/2$ for a proton and a neutron respectively. The isospin projection for a nucleus is thus

$$T_Z = \frac{(N - Z)}{2}. \quad (1.3)$$

The isospin of a nuclear state must be larger than or equal to the magnitude of the projection. The isospin of a nuclear state increases with excitation energy, with the lowest-lying states having isospin equal to the projection T_Z . Isospin symmetry is not exact: this is exemplified in the larger mass of the neutron compared to the proton.

If a nuclear state has isospin T , it is part of a set of $2T+1$ nuclear states in different nuclei of the same isobar (nuclei with the same mass number, A), all of which have isospin T . This set is known as an isospin multiplet. Figure 1.4 shows an abbreviated example of this concept. The ground state of ^{11}Li has a spin and parity, J^π , of $3/2^-$. According to Eq. 1.3, its isospin projection is $T_Z = \frac{5}{2}$ (as it has 3 protons and 8 neutrons), and total isospin of $T = \frac{5}{2}$. The dashed line in Fig. 1.4 connecting the ground state of ^{11}Li to the $3/2^-$ excited state in ^{11}Be signifies that this state is part of the same isospin multiplet as $^{11}\text{Li}_{g.s.}$, in this

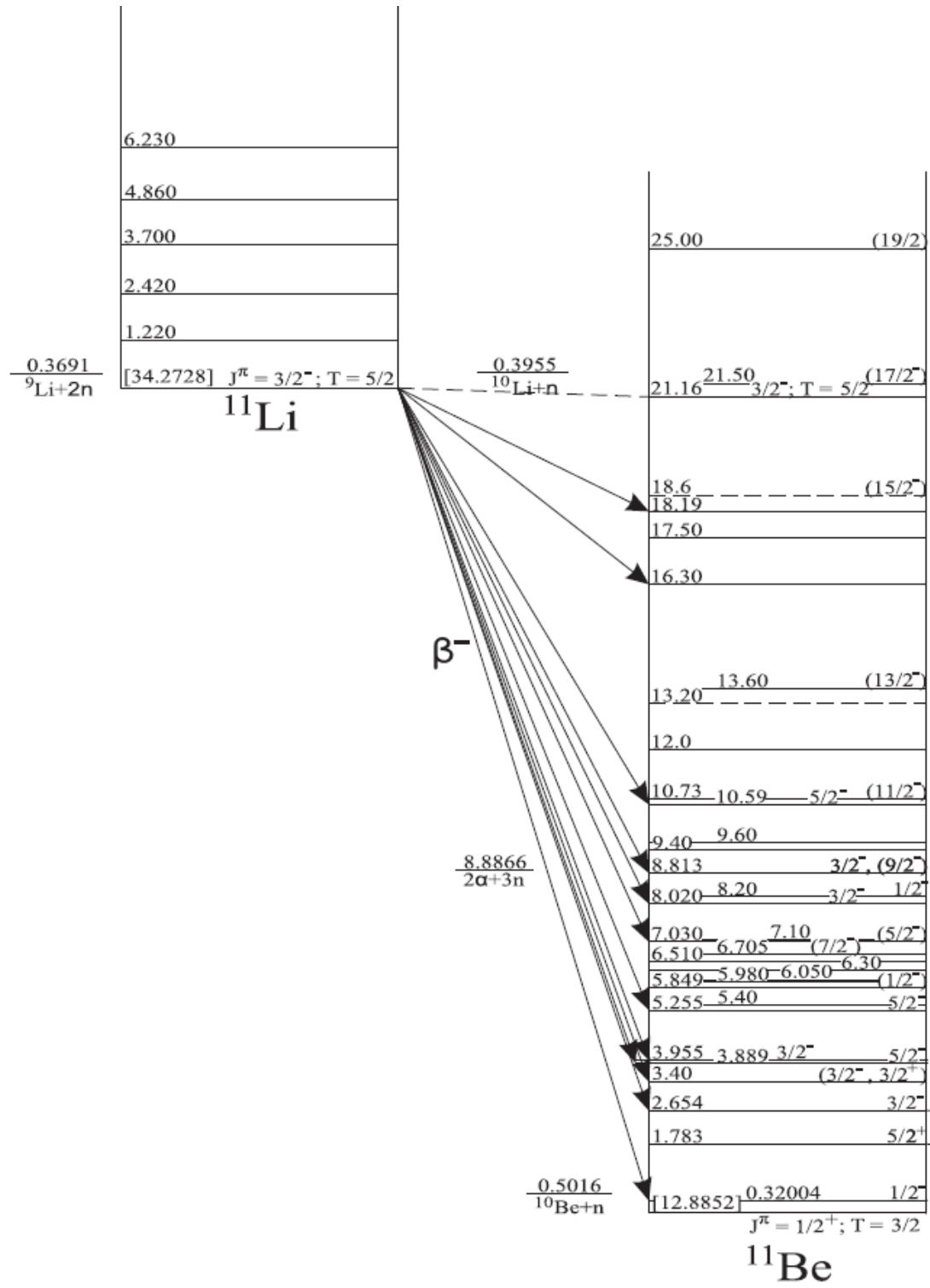


Figure 1.4: Levels in ^{11}Li and its isobaric neighbor ^{11}Be . The isobaric analog states in the two nuclei are connected by the dashed line. Taken from [1].

case an isospin sextet, as $T = 5/2$. As the neighboring nucleus to ^{11}Li in the sextet, the state in ^{11}Be at 21.16 MeV of excitation is called the *isobaric analog state* of $^{11}\text{Li}_{g.s.}$.

If isospin were a good quantum number and the Coulomb energy could be ignored, the masses of each member of a multiplet would be identical. This is obviously not the case as the Coulomb force cannot be ignored and has a real effect on nuclear masses. Wigner found that if two-body forces are responsible for charge-dependent effects on the mass of a nucleus, then the masses of the members of an isospin multiplet are expected to follow a quadratic dependence $M(T, T_Z) = a + bT_Z + cT_Z^2$, called the isospin multiplet mass equation (IMME). The IMME has been verified for a number of quartets and quintets with few deviations. With four observed members, the $A=11$ sextet is the most complete at present, and the masses of the three members with the largest isospin projection, T_Z , have provided a determination of the IMME parameters for the sextet [21]. The addition of a fourth member would allow us to probe deviations from the IMME in an isospin sextet for the first time. A large portion of this thesis details the examination of the structure of the fourth added member of the $A = 11$ sextet, ^{11}O .

1.3 $2p$ Decay

1.3.1 Proton Decay

When the separation energy of a proton, S_p , becomes negative, and energy can be released by emitting a proton, proton decay occurs. Nuclei that decay via proton emission are said to be beyond the “proton drip line.” Nuclei beyond the proton drip line can release a single proton ($1p$ decay) or several depending on their level of instability. Quantum mechanically speaking, protons leaving the nucleus must tunnel through the Coulomb barrier, which becomes higher with increasing Z . The half-life for a proton decaying nucleus at fixed S_p thus increases with Z .

Two-proton ($2p$) decay is the emission of two protons from a nucleus. The decay mode

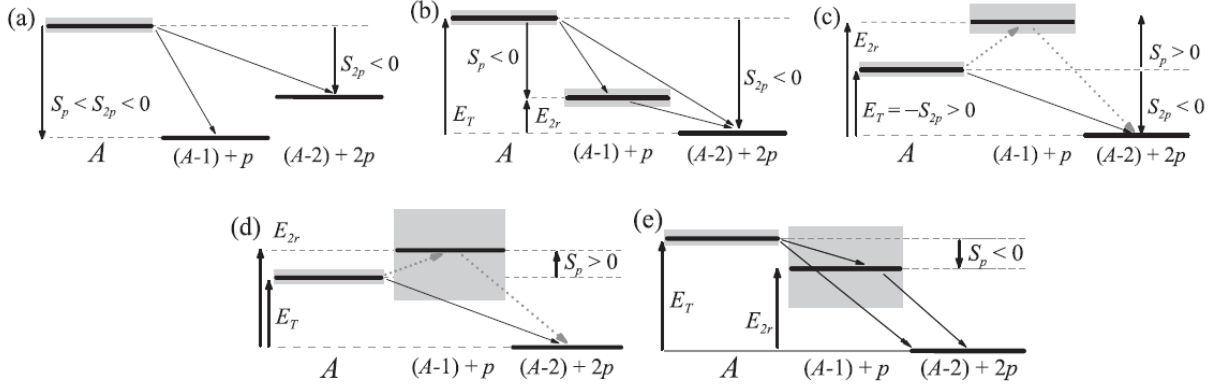


Figure 1.5: The various types of $2p$ decay. (a) and (c) show direct $2p$ decay, b(b) shows sequential $2p$ decay, and (d) and (e) show “democratic” $2p$ decay. Taken from [2].

was first predicted to occur in even- Z nuclei by Goldansky in 1960 [22]. The reasoning behind this prediction is that even- Z nuclei near the drip line could emit two protons when the $1p$ -decay channel is energetically forbidden due to pairing of the protons. This is the case illustrated in Fig. 1.5(c). In cases where the $2p$ -decaying nucleus has an energetically available $1p$ -decay channel, the nucleus may decay through a sequence of $1p$ -decays through the available intermediate state (Fig. 1.5(b)). If the intermediate state is lower in energy than the final state, but both are energetically available, the possibilities for decay look like Fig. 1.5(a). In this case, the $2p$ and $1p$ channels compete. If the intermediate state is very wide, the decay looks like Fig. 1.5(d)/(e), and it is unclear if the decay is sequential or simultaneous.

1.3.2 Decay Correlations

To probe the dynamics of a $2p$ -decaying nucleus, one can examine the momentum correlations between the decay fragments (the two emitted protons and the heavy core). These correlations describe the relative motion of the three bodies involved in the decay, and can be accessed by a change of coordinate system in the center of mass frame. Two common systems, the Jacobi “T” and “Y” systems, used for describing this relative motion are shown in Fig. 1.6. The energies, masses, and angles for the Jacobi momenta labeled in Fig. 1.6 are

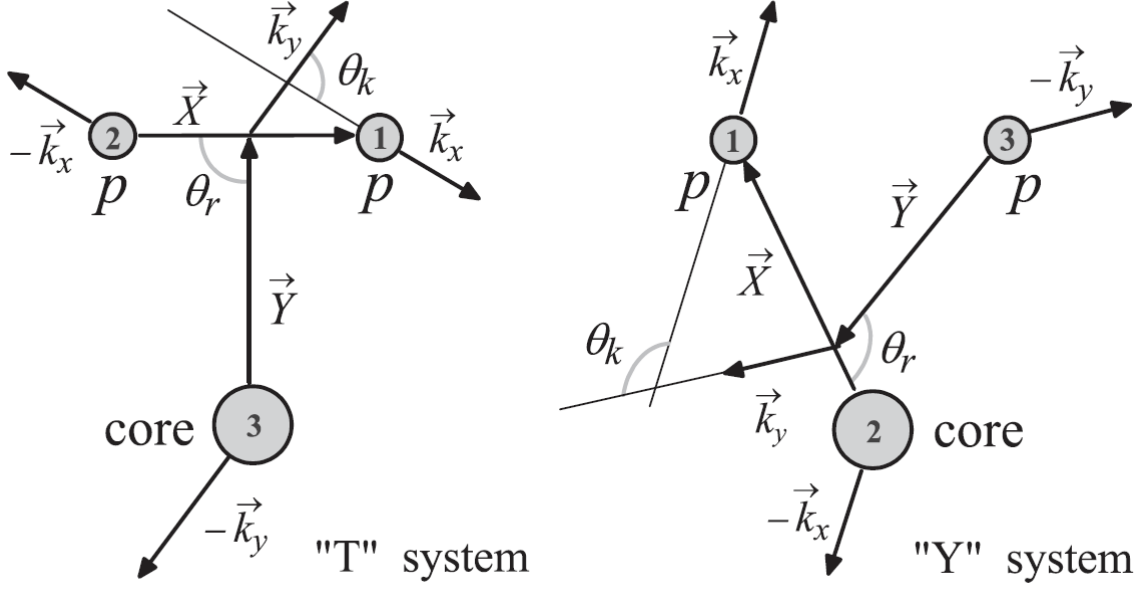


Figure 1.6: The Jacobi “T” and “Y” systems. Taken from [3].

described by

$$\varepsilon = E_x/E_T, \quad \cos(\theta_k) = (\mathbf{k}_x \cdot \mathbf{k}_y)/(k_x k_y),$$

$$E_T = E_x + E_y = k_x^2/2M_x + k_y^2/2M_y, \quad (1.4)$$

$$M_x = \frac{A_1 A_2}{A_1 + A_2} M, \quad M_y = \frac{(A_1 + A_2) A_3}{A_1 + A_2 + A_3} M, \quad (1.5)$$

$$\mathbf{k}_x = \frac{A_2 \mathbf{k}_1 - A_1 \mathbf{k}_2}{A_1 + A_2}, \quad \mathbf{k}_y = \frac{A_3 (\mathbf{k}_1 + \mathbf{k}_2) - (A_1 + A_2) \mathbf{k}_3}{A_1 + A_2 + A_3}, \quad (1.6)$$

where M_x and M_y are the reduced masses of the X and Y subsystems respectively, A_i are the particles’ mass numbers, and M is the nucleon mass.

The quantities described in the above equations can be plotted in a way that sheds light on the type of $2p$ decay, that is, differentiating prompt decay from sequential decay. We generally consider a 2D distribution of ε and $\cos(\theta_k)$. The clear kinematic signature of prompt decay is that the protons equally share the decay energy [22], while the indicator of sequential decay is that each proton has a clear and consistent fraction of the total decay

energy determined by the relative spacing in energy of the parent, intermediate, and daughter levels. Examining these two quantities also allows us to differentiate between the first and second emitted proton in sequential decays. These features will be shown more explicitly in a later chapter.

1.4 Proton Therapy for Radiation Oncology

1.4.1 Fundamentals of Radiation Therapy

Radiation therapy's function in cancer treatment is to kill malignant cells via external ionizing radiation. The ionizing radiation damages the DNA of tumor cells, usually by breaking both strands of DNA, causing cell death upon division or apoptosis if the strand break is not repaired. A nice summary is shown in Fig. 1.7. The DNA damage can be effected through a few different ionizing radiation modalities, some internal, like brachytherapy or unsealed source radiotherapy, and others external, most notably external beam therapy, which is the subject of the rest of this section.

External beam therapy can be easily divided into two groups, photon or x-ray therapy and charged-particle therapy. Photon therapy involves creating a polyenergetic beam of photons using an x-ray tube that is sent through a tumor inside a patient. The photons in the beam deposit energy in the tumor, damaging the DNA of the tumor cells and causing the effects detailed in Fig. 1.7. The amount of energy per unit mass deposited by the radiation is called the dose. The photon beam also passes through tissue in front of and behind the tumor, depositing a dose to and possibly damaging healthy tissue.

1.4.2 The Bragg Peak and Stopping Power

When trying to spare healthy tissue, charged-particle therapy provides a clear theoretical advantage. Instead of depositing relatively large amounts of dose in random, discrete events all along the beam path, like photons, charged particles deposit their energy continuously

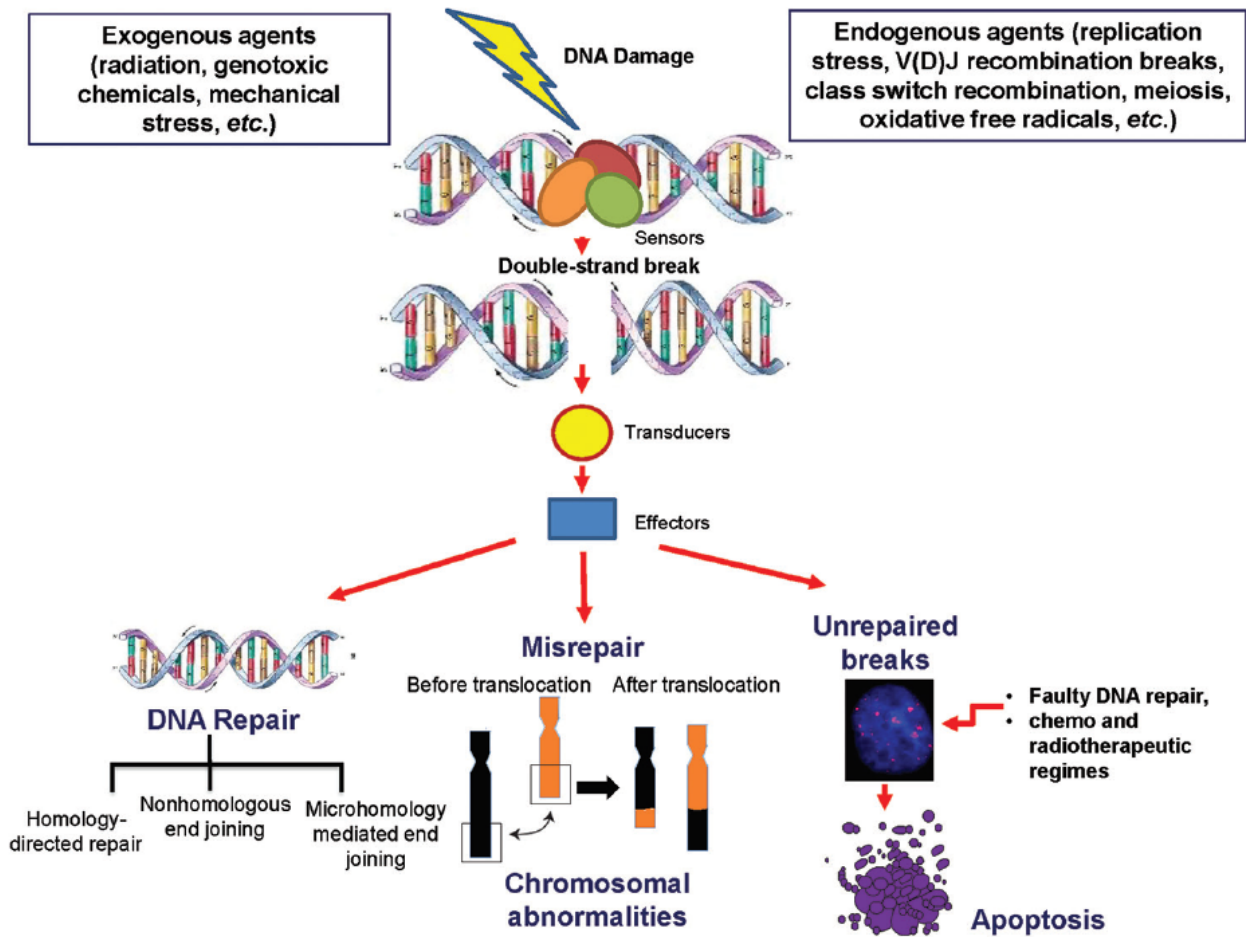


Figure 1.7: A summary of the results of double-strand breaks due to external radiation in the nucleus of a cell. The cell can repair the break, or chromosomal anomalies can occur, which can cause cell death upon division. The cell could even undergo direct apoptosis as a result of the break. Taken from [4].

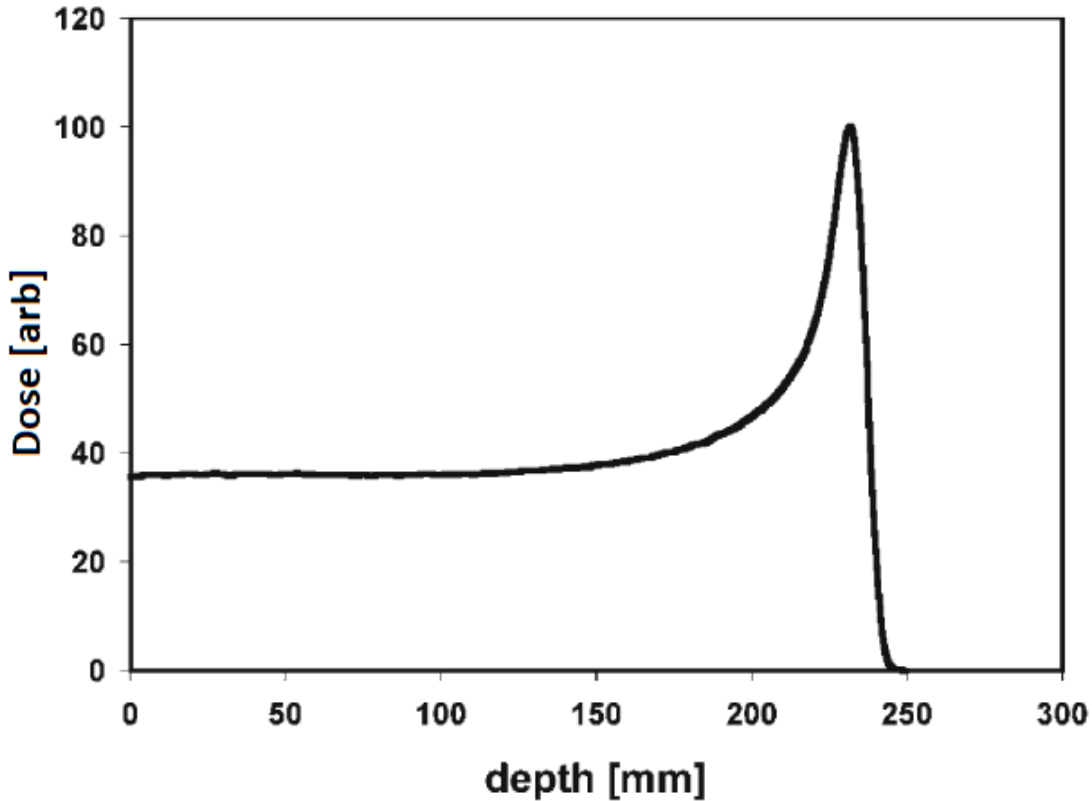


Figure 1.8: A dose-depth curve for protons. Note the prominent Bragg peak right before the end of the protons' range. Taken from [5].

as they pass through tissue, depositing most of their energy in a region called the the Bragg peak located right at the end of the particles' range. A Bragg peak is seen in the generic dose-depth curve for protons shown in Fig. 1.8. You can see that the dose delivered remains relatively constant until the Bragg region is reached. The dose then rises and falls very rapidly. You can see that, if the Bragg region is focused on the tumor site, the tissue behind the tumor can be spared radiation damage. This is one of the principal advantages of proton therapy.

The energy loss of protons in matter is dependent on both the energy of the protons and quantities associated with the matter. The amount of energy lost per unit distance traveled by a proton is given by the stopping power (S_p) calculated from the Bethe equation [23]

according to

$$S_p(E_p) = \frac{dE_p}{dx} = \rho_e \frac{k_1}{\beta^2} \left[\frac{1}{2} \ln \frac{k_2 \beta^2 T_{max}}{I^2 (1 - \beta^2)} - \beta^2 \right], \quad (1.7)$$

where E_p is the proton's kinetic energy, β is the proton's speed as a fraction of the speed of light (v/c), T_{max} is the maximum amount of kinetic energy that the proton can impart to an electron, k_1 and k_2 are products of physical constants, and ρ_e and I are the electron density and mean excitation energy respectively of the matter the proton is passing through. There are shell and density corrections often added to 1.7 that we omit here because they are negligible at the energy of clinical proton machines. Note that as the kinetic energy (speed) of the proton decreases, the stopping power increases.

The stopping power ratio (SPR) is a clinically useful quantity defined as the stopping power of a material relative to the stopping power of water. This will be the quantity most often discussed in this work.

1.4.3 Fundamentals of CT Imaging

X-ray computed tomography (CT) imaging is a powerful and important tool in medical imaging. The fundamental pieces of a CT system are an x-ray source and a detector array that co-rotate, as shown in Fig. 1.9. The x-ray tube generates a burst of x-rays that pass through the patient and enter the detectors. The measurement for a given detector is given by an integral for all emitted energies along a line through the patient, given by

$$I_d = \int_0^{E_{max}} S_0(E) E \exp \left[- \int_0^d \mu(s; E) ds \right] dE, \quad (1.8)$$

where $S_0(E)$ is the spectrum of the x-ray source, $\mu(s; E)$ is the energy-dependent linear attenuation coefficient along the line between the source and detector, and E_{max} is the maximum energy of the polychromatic x-ray spectrum. Equation 1.8 is usually simplified by using the concept of the effective energy, \bar{E} , the single energy that, in some given material, will yield

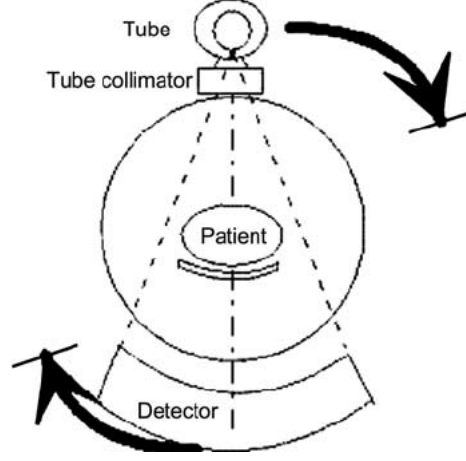


Figure 1.9: The fundamentals of a 3rd generation CT scanner. The x-ray tube and detector array rotate around the patient. Combining the signal seen in a detector with knowledge of the angle of the source-detector pair's rotation and the index of the detector allows a cross-sectional image of the patient to be reconstructed. Taken from [6]

the measured intensity of the full polychromatic source [24]. The simplified equation is

$$I_d = I_0 \exp \left[- \int_0^d \mu(s; \bar{E}) ds \right]. \quad (1.9)$$

This equation can be rearranged to yield

$$g_d = - \ln \left(\frac{I_d}{I_0} \right) = \int_0^d \mu(s; \bar{E}) ds, \quad (1.10)$$

where g_d is now our measured quantity of interest.

It is possible to reconstruct a picture of μ across an entire cross section by using a 2-D Radon transform. The relevant Radon transform for CT reconstruction [24] is summarized by

$$g(\ell, \theta) = \int_{-\infty}^{\infty} \int_{-\infty}^{\infty} \mu(x, y, \bar{E}) \delta(x \cos \theta + y \sin \theta - \ell) dx dy, \quad (1.11)$$

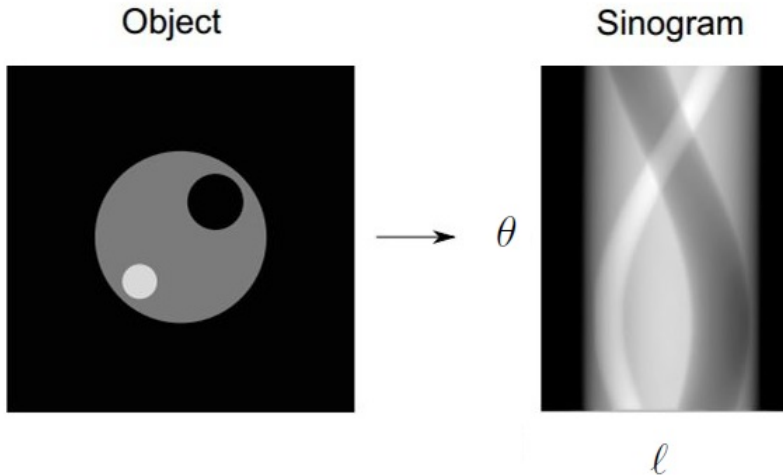


Figure 1.10: An object and its sinogram. Taken from [7].

where

$$x(s) = \ell \cos \theta - s \sin \theta, \tag{1.12}$$

$$y(s) = \ell \sin \theta + s \cos \theta. \tag{1.13}$$

Here ℓ can be thought of as a detector index and θ as the angle of rotation of the source-detector pair.

When $g(\ell, \theta)$ is plotted with ℓ and θ as the coordinates, the resulting image is called a sinogram. An example sinogram is shown in Fig. 1.10. The x-axis corresponds to a detector index (ℓ) while the y-axis corresponds to the rotation angle of the source-detector pair relative to the patient. The sinogram has clearly visible structures, and provides all the information that we need to reconstruct an image of the original cross section. There are a variety of ways to reconstruct an image from a sinogram, including exact, analytical methods like filtered and convolutional backprojection, and also iterative methods, like the one discussed in this work.

Chapter 2

Experimental Methods

2.1 Overview

The principal goal of the experiment presented in this thesis was a measurement of the decay energy, intrinsic width, decay mode, and decay correlations of ^{11}O , the mirror of ^{11}Li . Previous studies have observed the single and double isobaric analog states (IAS) of ^{11}Li in ^{11}Be [25] and ^{11}B [21] respectively, and the addition of $^{11}\text{O}_{gs}$ would make the $A = 11$, $T = 5/2$ levels the most complete isobaric isospin sextet at present. ^{11}O is $2p$ -unbound and decays in $< 10^{-21}\text{s}$, so it must be observed by reconstructing coincident $2p + ^9\text{C}$ events.

The experiment was performed at the National Superconducting Cyclotron Laboratory (NSCL) at Michigan State University. A schematic of the experiment is shown in Fig. 2.1. The coupled cyclotrons (K500 + K1200) at the NSCL delivered a ^{16}O primary beam at 150 MeV/A which bombarded a ^9Be target. Reactions between the beam and the target produced light fragments, and the ^{13}O fragments were selected by the A1900 magnetic separator [26]. The A1900 works by selecting fragments using a large bending magnet which then pass through an energy degrading “wedge”. The fragments which leave this wedge then pass through another bending magnet, providing isotopic separation. Upon extraction from the separator, the 69.5 MeV/A secondary beam had a purity of only 10%. To remove the

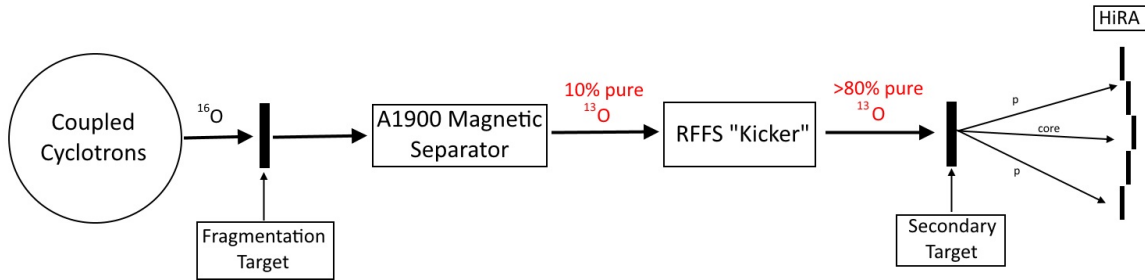


Figure 2.1: Schematic of the experimental setup. The stable ^{16}O beam (black) is accelerated by the K500 and K1200 coupled cyclotrons. It then impinges on a ^9Be target, fragmenting. The fragments produced are then separated by the A1900 magnetic separator by their charge-to-mass ratio. The radioactive ^{13}O beam (red) then passes through the radio frequency fragment separator (RFFS), which increases the purity from 10% to more than 80%. The beam is then transported to the experimental area, where it bombards a ^9Be secondary target, creating unbound decay products which are detected by HiRA.

substantial contamination, the beam was sent into an electromagnetic time-of-flight filter, the Radio Frequency Fragment Separator [27], and emerged with a purity greater than 80% and a rate of 3000 pps. The secondary beam impinged on a 1mm thick ^9Be target. Two neutron knockout reactions between the secondary beam and the target produced ^{11}O .

2.2 The Invariant-Mass Method

The invariant-mass method is ideal for measuring the decay energy of very short-lived particle-unbound states. By measuring the momenta and determining the particle type of all products of a decay, the mass of the parent can be reconstructed in its rest frame. This invariant mass is given in Eq. 2.1.

$$Mc^2 = \sqrt{(\sum_i E_i)^2 - (\sum_i \vec{p}_i c)^2} \quad (2.1)$$

In the above equation, E_i and p_i are the total (mass + kinetic) energy and momentum of each particle, indexed by i .

Frequently, rather than using the invariant-mass proper, we find it more convenient to

consider the total kinetic energy released in the decay and shared by the decay fragments in the center-of-mass frame of the fragments

$$E_T = M_{inv} - \sum M_i \quad (2.2)$$

where M_i are the rest masses of the detected fragments. If the ground state rest mass of the parent, $M_{g.s.}^{parent}$, is well known, we can also consider

$$E_{n\gamma}^* = M_{inv} - M_{g.s.}^{parent}. \quad (2.3)$$

Equation 2.3 only represents the true excitation energy if all the detected fragments were produced in their ground states rather than particle-stable excited states. Some detected fragments discussed in this work (${}^6\text{Li}$, ${}^{10}\text{B}$, ${}^{10}\text{C}$) have γ -decaying levels. When considering decays involving these fragments, the true excitation energy is obtained by adding the sum of the γ -rays' energies

$$E^* = E_{n\gamma}^* + \sum_i E_\gamma^i \quad (2.4)$$

where E_γ^i are the energies of the γ rays emitted by the deexcitation of the fragments. ${}^6\text{Li}$ and ${}^{10}\text{C}$ have a single γ -decaying excited state each, limiting the number of possible excitation values for decays to two that involve one of these fragments.

A major degrading factor of the resolution of invariant-mass spectra is the energy loss of the fragments as they leave the target, specifically changes in the fragments' relative velocities [28]. Protons have much smaller velocity losses relative to the heavy cores. We make an average correction to the fragments' energies, assuming that the reaction we are reconstructing takes place in the center of the target material. This gives the correct average invariant mass. The effect of relative velocity loss on the resolution can be minimized by selecting events in which the emission angle of the core relative to the beam axis, θ_C , in the center-of-mass frame is transverse to the beam axis. We can apply a gate to $\cos \theta_C$ to select

these transverse events. Events where $\theta_C \sim 0^\circ$ ($\cos \theta_C \sim 0$) have the best resolution [28]. The gates used, if any, are specified in the figure captions.

The momentum of each fragment can be determined by measuring the energy deposited in the Si and CsI(Tl) telescopes which make up HiRA and using the segmented Si detectors to determine the vector's direction. Particle identification is obtained with the $\Delta E - E$ technique, using the fact that different particle species deposit energy in matter differently based on the stopping power relation, given in Eq. 2.5.

$$\frac{dE}{dx} \propto \frac{Z^2 A}{E} \quad (2.5)$$

where Z is the fully-stripped fragment's charge, A is its mass number, and E its kinetic energy. If the energy dropped in a thin detector by an incident particle (ΔE) is plotted against the remainder of its energy left in a thick detector (E), the particles separate into bands determined by their mass and charge. An example $\Delta E - E$ plot is shown in Fig. 2.2. Note the excellent separation between the isotopes of carbon shown in panel (b). This clear isotopic separation is essential in the analysis of the different particle-decay channels discussed in this work.

2.3 The High Resolution Array

The High Resolution Array (HiRA) [29] was used to detect the fragments produced by reactions between the beam and the target. In this experiment, 14 of HiRA's Si-CsI(Tl) telescopes were arranged in five towers, as shown in Fig. 2.3. The array was located 85 cm downstream of the secondary target and subtended a polar angular range of 2.1° to 12.4° . Each telescope consisted of a 1.5-mm-thick double-sided silicon strip ΔE detector backed with four 4-cm-thick CsI(Tl) E detectors. Each CsI(Tl) spans a quadrant of the Si detector. Both the Si detector and the CsI(Tl) scintillators are necessary to perform the $\Delta E - E$ particle identification method discussed in the preceding section. Fig. 2.4 shows

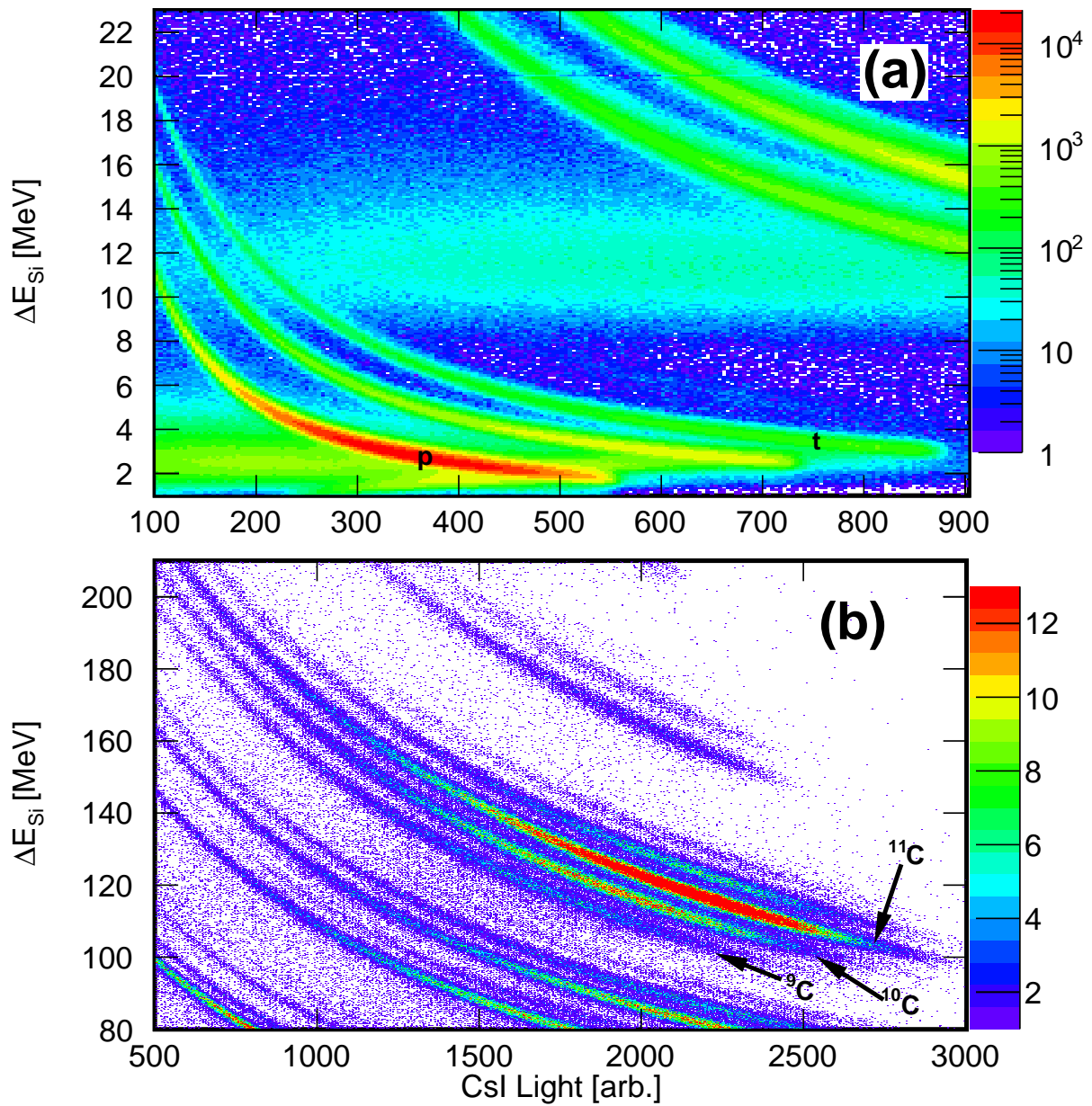


Figure 2.2: (a) A zoomed-view of a $\Delta E - E$ plot used for particle identification. The three large bands at the left of the plot are the $^{1,2,3}\text{H}$. The two bands seen at the upper right are $^{3,4}\text{He}$. (b) A zoomed-in view of the carbon band. The small bands represent different isotopes of carbon.

the configuration described here. The 65 μm Si detector shown in the figure was not used in this experiment.

The signals produced in the Si were processed by the HINP4 chip electronics designed by our group in collaboration with Southern Illinois University Edwardsville. The HINP4 chips possess a dual-gain amplification system so that signals generated by both light and heavy fragments can both be amplified and processed. Signals from the CsI(Tl) detectors were processed using charge-sensitive amplifiers (CSAs) placed directly behind the crystals.

As can be seen in Fig. 2.3, the setup is slightly more complex than initially described. The Si detectors are shielded by Mylar foils drawn over aluminum frames, which are affixed at the front of the telescopes. The CSAs must be cooled during operation, so copper bars that provide water cooling are placed in contact with the plate holding the CSAs. There is also a copper mouth piece that is placed in the center of the array to prevent the beam from scattering into the central CsIs.

2.3.1 The Silicons (ΔE)

The thin ΔE detectors of HiRA are ion-implanted silicon semiconductors made by Micron Semiconductor [30]. Each detector has a 6.4 cm x 6.4 cm face and is 1.5 mm thick. Both the front and back of the detector are subdivided into 32 strips orthogonal to one another. This segmentation gives angular resolution on the order of 0.1° and allows each detector to detect multiple particles.

As charged particles move through the semiconductor detectors, they create electron-hole pairs within the detector. The number of pairs is linearly proportional to the energy deposited (E_d) and depends on the band gap the detector material. Because of Coulombic attraction, the electron and hole will try to recombine, but application of an electric field ($E \approx 2000 \text{ V/cm}$ for a HiRA silicon) across the detector will cause the electron and hole to drift to opposite surfaces of the detector for collection. Because the number of pairs is proportional to E_d , the amount of collected charge can be used to determine the energy

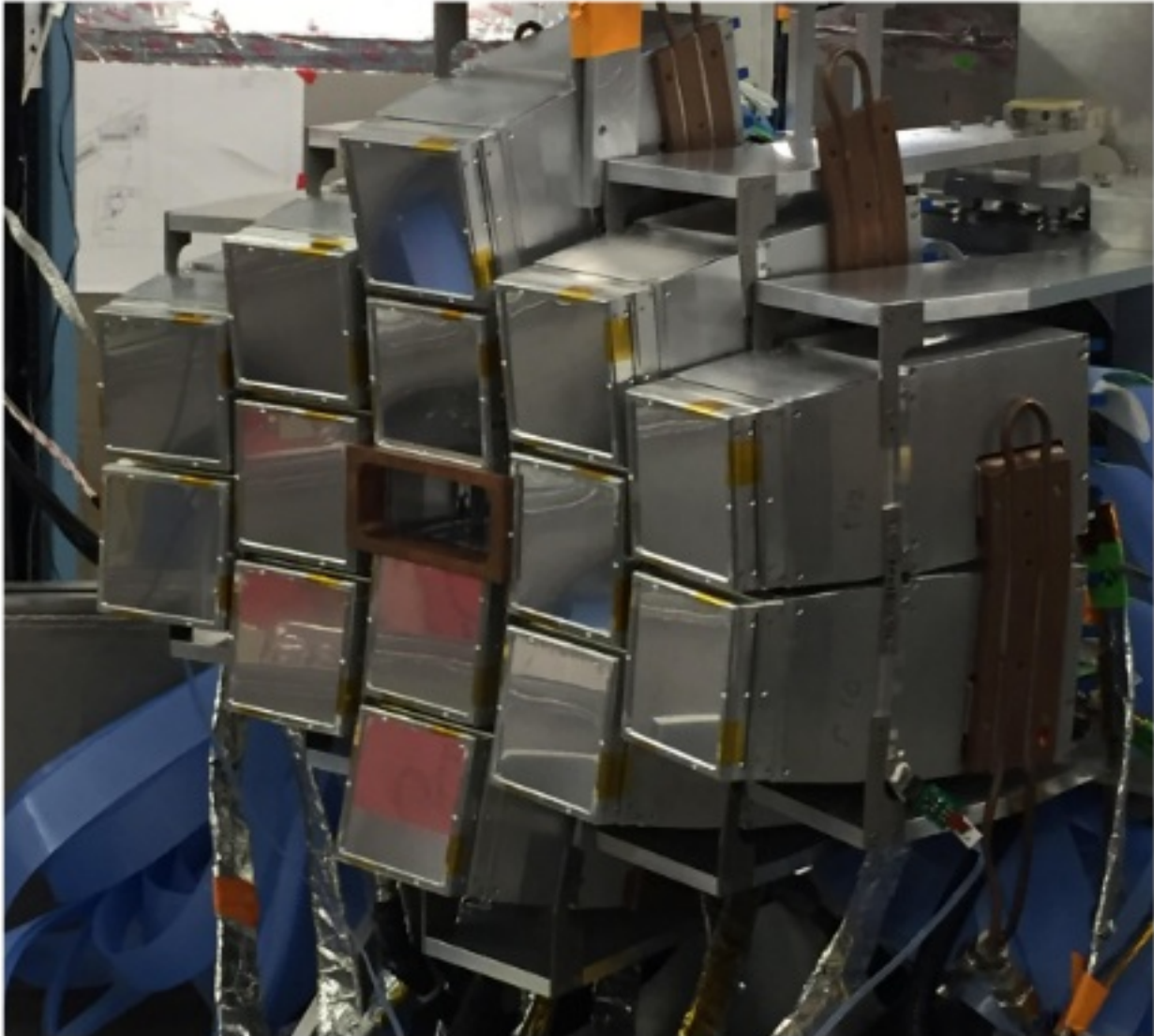


Figure 2.3: The HiRA array. Note the Mylar shielding in front of the Si detectors, the cooling bars affixed to the back of the telescopes, and the copper mouthpiece at the center of the array.

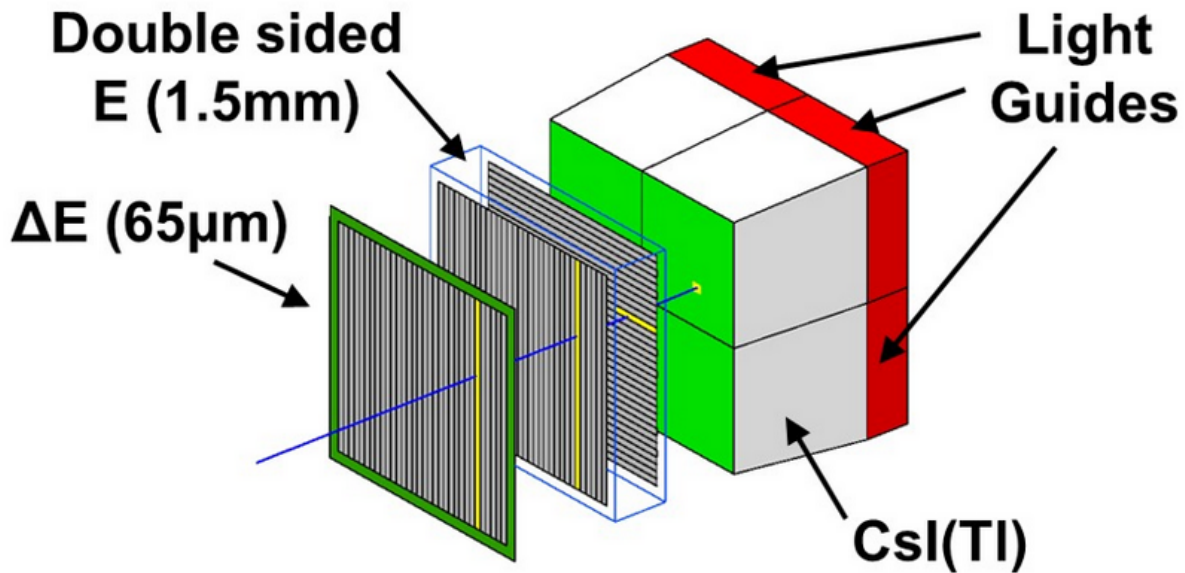


Figure 2.4: A cartoon showing what is inside each of the 14 canisters that make up HiRA. A double-sided, segmented silicon detector is backed by 4 CsI(Tl) scintillators. The $65\ \mu\text{m}$ single-sided silicon detector shown in this figure was not used for this experiment.

deposited by the charged particles passing through the detector.

Silicon detectors are sandwiches of two differently doped silicon crystals, forming a p-n junction. The n-type crystal is made by adding a group V element impurity into the Si bulk, and the p-type by doping the Si with a group III element. Thermal diffusion drives electrons from the n-type crystal to the p-type, creating a region between without charge carriers. This is known as the depletion region and forms a barrier to current flow across the junction. If a positive potential is applied to the n region and a negative potential to the p region, the depletion region can be enhanced. This is a process called reverse biasing, and can be used to extend the depletion region across the entire bulk of the detector. When a charged particle passes through a reverse-biased detector and creates electron-hole pairs, they are swept from the bulk to opposite surfaces and collected with metal contacts attached to the faces of the detector. The HiRA detectors thus determine how much energy was dropped by a charged particle in the silicon, and the segmented faces provide position information by

determining which strips on the front and back collected charge.

2.3.2 The Scintillators (E)

HiRA's stopping detectors are 4-cm-thick CsI(Tl) crystals doped with thallium. The crystals are trapezoidal, 3.5 cm x 3.5 cm in the front and 3.9 cm x 3.9 cm in the back. Each crystal has a 3.9 cm x 3.9 cm x 1.3 cm light guide optically coupled to its back by BC 600 optical cement. A 1.8 cm x 1.8 cm Si photodiode is glued to the light guide with RTV615 silicon rubber. Each crystal is optically separated from the others in its telescope by a wrapping of cellulose nitrate on the long sides and an aluminized Mylar foil on the front. The light guides are painted with reflective BC-260 paint. Each telescope consists of four of these crystals wrapped together with Teflon tape and placed behind a silicon.

Scintillators produce visible light proportional to the amount of energy absorbed by the material. Charged particles incident on the crystal create bound electron-hole pairs called excitons which move within the crystal until they are trapped by dopant impurities (Tl in this case) or a crystal defect. The excitons then de-excite, emitting a visible photon. This light is then guided to and collected by the photodiode, creating electron-hole pairs in the diode which can be read out as a current.

2.3.3 Detector Calibration

Because the invariant-mass method requires determinations of energy deposited by charged particles, the detectors must be accurately calibrated. The silicon detectors were calibrated with a ^{232}U source, the decay chain of which is given in Table 2.1. These alphas of known energies and intensities can be assigned to the lines present in an alpha spectrum measured by the silicons, and a linear calibration of ADC channel number to energy can be extracted. A typical calibrated alpha spectrum taken with a HiRA silicon is shown in Fig. 2.5. The chip electronics used to process the signals from the silicon detectors have nonlinearities, as seen in Fig. 2.6. To probe and correct for these nonlinearities, known, evenly spaced

Parent	$t_{1/2}$	E_{α_0} (MeV)	E_{α_1} (MeV)	f_{α_0}	f_{α_1}	f_{β}
^{232}U	68.9 y	5.320	5.263	0.682	0.316	0
^{228}Th	1.912 y	5.423	5.340	0.734	0.260	0
^{224}Ra	3.632 d	5.686	5.449	0.949	0.506	0
^{220}Rn	55.6 s	6.288	-	0.999	0	0
^{216}Po	0.145 s	6.778	-	0.999	0	0
^{212}Pb	10.64 h	-	-	0	0	1
^{212}Bi	60.55 m	6.089	6.050	0.098	0.251	0.641
^{212}Po	0.229 μs	8.784	-	1	0	0
^{208}Tl	3.053 m	-	-	0	0	1
^{208}Pb	stable					

Table 2.1: The alpha energies, half-lives, and branching ratios for the ^{232}U decay chain. α particles with under 5% intensity are not included. α_0 and α_1 are the decays to the ground and first-excited state of the daughter.

voltages were pulsed into the chips and the output spectra were examined. A typical pulser spectrum is shown in Fig. 2.6. The electronics are linear for low voltages and compressive for higher ones.

CsI(Tl) scintillator's light output depends on the charge and mass of the ion entering the detector. Heavier ions have a higher rate of energy loss than light ones, creating a larger ionization density. This leads to quenching of the light emitted by the scintillator. Because of this quenching, the light output, and therefore the energy calibration, of the CsI(Tl) is particle dependent. To account for this particle dependence, calibration beams which contain all the isotopes of interest are used. For this experiment we used three calibration beams. Each beam was a cocktail beam containing a few isotopes at the same rigidity ($B\rho$). The major component of each beam were 80 MeV/A protons, 80 MeV/A ^4He , and 85 MeV/A ^{12}C .

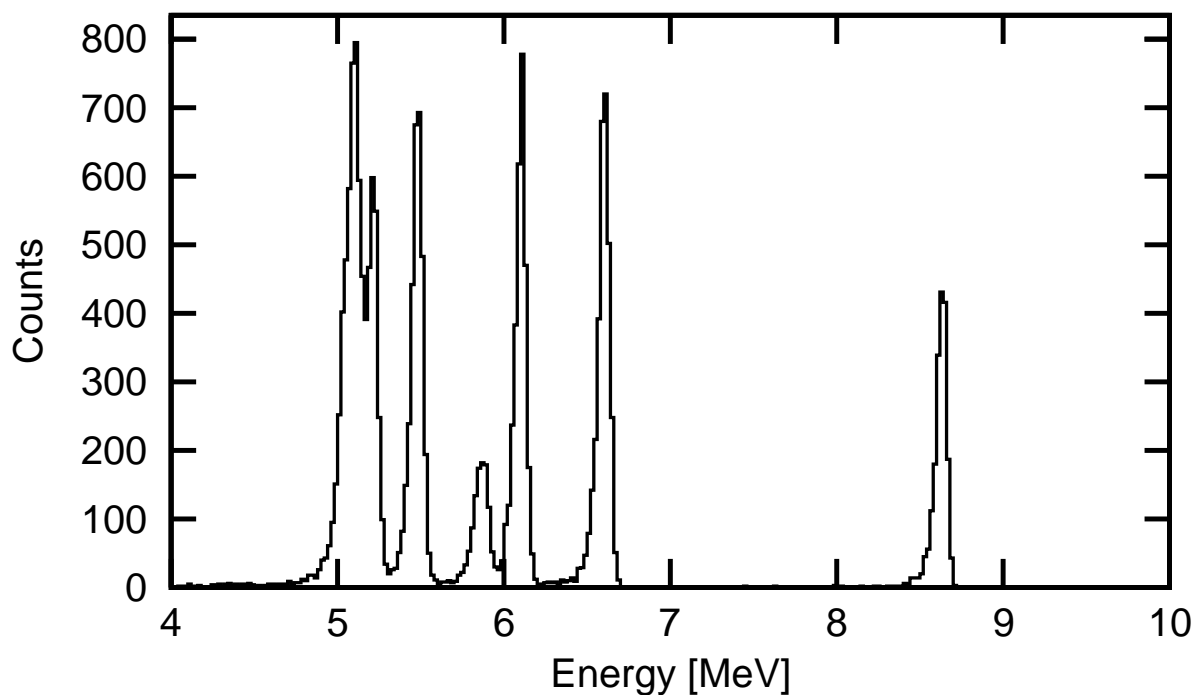


Figure 2.5: A calibrated alpha spectrum for a typical silicon front (hole collecting) strip. The observed peaks are those given in Table 2.1

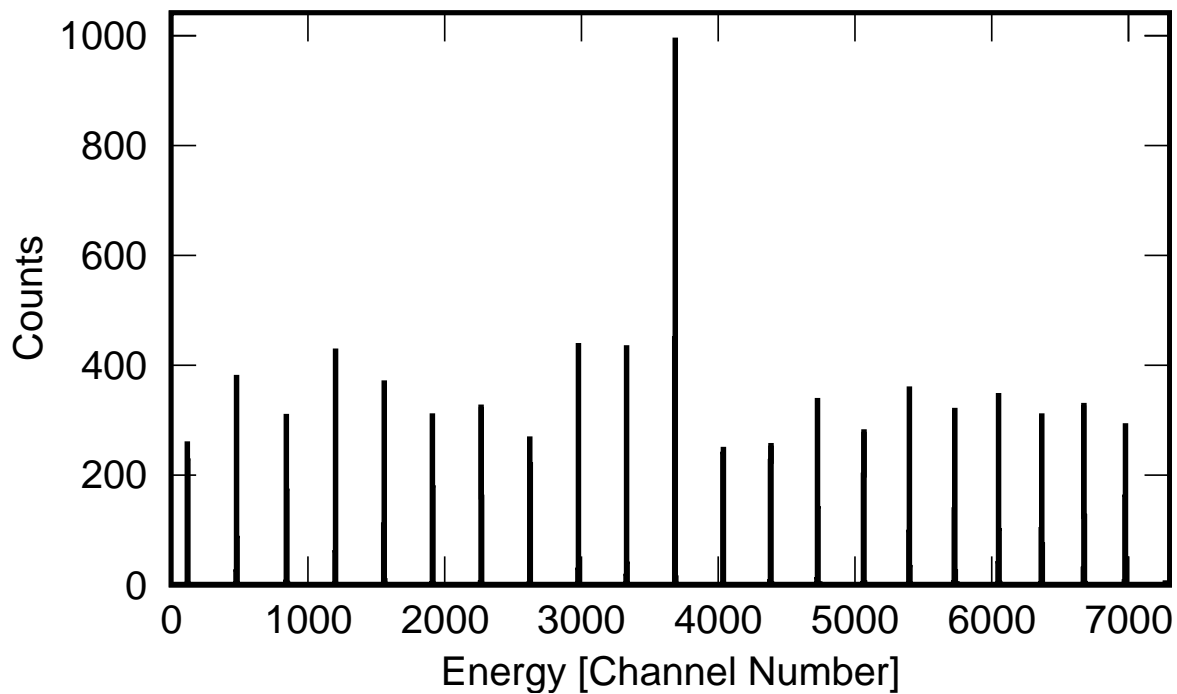


Figure 2.6: Pulser calibration for a typical silicon strip on the front of the detector. The data shown are taken from the low-gain channel. The pulses are in uniform increments of charge, and a non-linearity above half scale is clearly seen. The large peak in the center of the spectrum corresponds to a pulse run for twice as long as the other pulses.

Chapter 3

^{11}Li

3.1 Overview

^{11}Li is a classic example of a halo nucleus, possessing a weakly bound two-neutron halo which extends well past the matter radius of the ^9Li core. Though the neutron-rich nuclide was first observed in 1966 [31], ^{11}Li 's unusual structure was not suggested until an interaction cross section measurement in 1985 revealed the nucleus to have an unusually large matter radius for an $A = 11$ nuclide, as shown in Fig. 3.2 [8]. This large matter radius is explained by treating the nucleus as two neutrons very weakly bound to a ^9Li core, forming what is known as a Borromean nucleus, a configuration that takes its name from the famed Borromean rings (shown in Fig. 3.1) which can only exist when all three bodies are present and interacting [32]. In the nuclear or atomic case, this means that the three-body system is bound but none of the 2-body sub-systems are bound. Other classic Borromean nuclei include ^6He and ^{22}C . Recent measurements of the two neutron separation energy S_{2n} are given in Table 3.1. S_{2n} is on the order of hundreds of keV, much smaller than binding energies per nucleon at stability (on the order of several MeV).

The two-neutron halo picture was supported by a projectile fragmentation experiment using a ^{11}Li beam on a C target [36]. The experimenters measured the transverse momentum



Figure 3.1: The interlocking Borromean rings from which Borromean nuclei take their name. The Borromean rings are named for the aristocratic Borromeo family, the owners of three islands in Lake Maggiore.

Reference	Method	ΔM (keV)	S_{2n} (keV)
[33]	Penning trap	40728.28(64)	369.15(65)
[34]	Mass Spec.	40719(5)	378(5)
[35]	Mass Spec.	40716(5)	375(5)

Table 3.1: A short summary of recent mass measurements and the two neutron separation energy of ^{11}Li .

distribution of ^9Li fragments and found its width to be much narrower than the widths of the distributions of the other observed heavy fragments. For nucleon knockout reactions, the momentum distribution of the nucleon-removal fragments reflects the distribution of the removed nucleon at the nuclear surface [37], so the neutron fragments must have similarly narrow distributions. By the uncertainty principle, a narrow momentum distribution requires a large spatial distribution for the two neutrons, which supports the picture that ^{11}Li has a two-neutron halo. More recent proton scattering and laser spectroscopy experiments [38, 39] have probed the charge and matter radii of ^{11}Li and found a charge radius consistent with other lithium isotopes while confirming the extended matter radius, providing further evidence for the two-neutron halo picture.

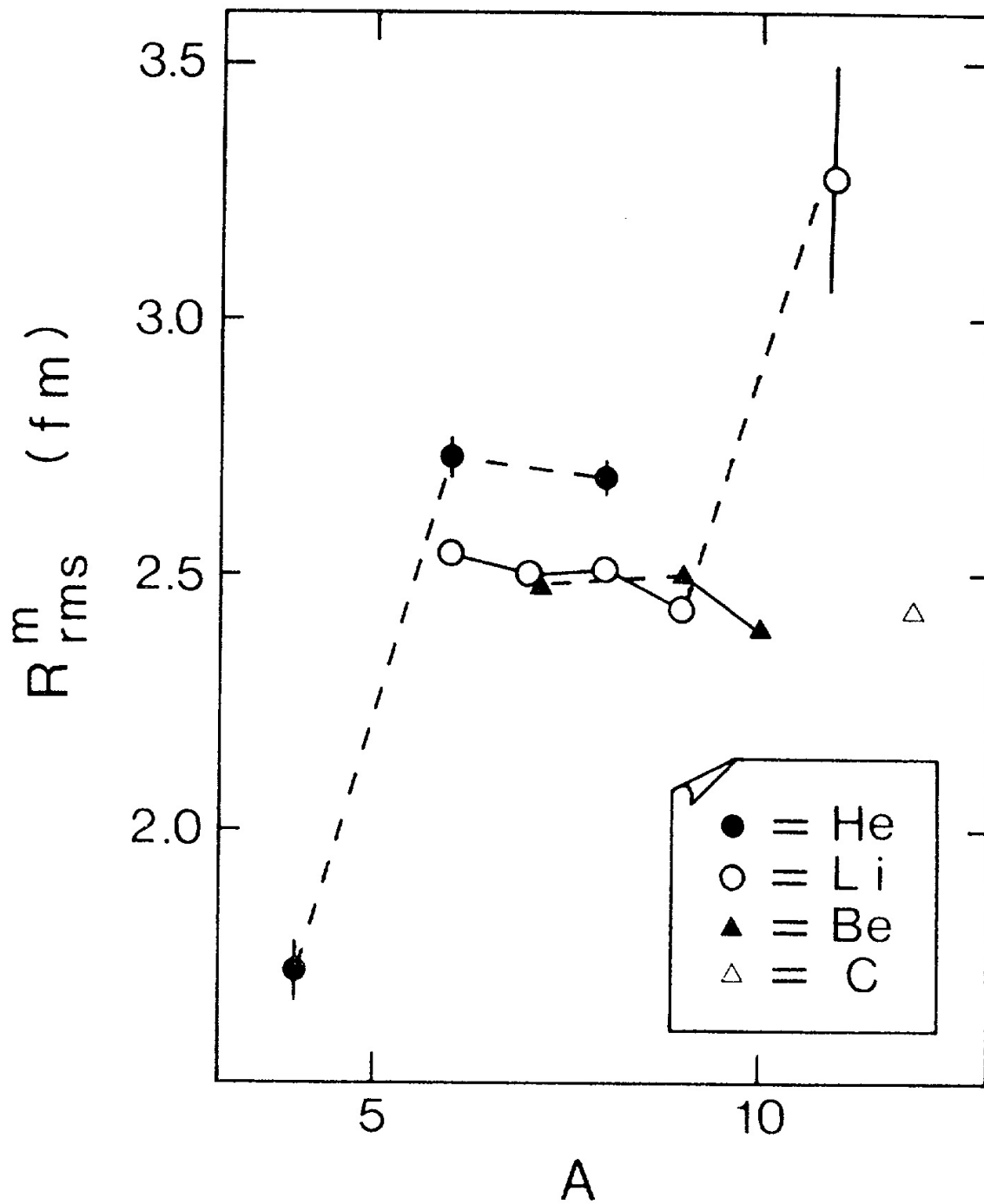


Figure 3.2: The rms matter radius R_{rms}^m for He, Li, Be, and C for varying mass numbers. Taken from [8].

3.2 Ground State Structure

^{11}Li 's extreme $\frac{N}{Z}$ ratio results in a nuclear structure drastically different from the Li isotopes near stability. As an $N=8$ nucleus, the shell model predicts that the valence neutrons should occupy the $p_{\frac{1}{2}}$ states, closing the p shell. Fragmentation experiments, however, report momentum distributions that can only be explained by a significant s^2 component in the $2n$ valence wavefunction [40, 41]. Reports of the degree to which the s^2 intrusion contributes to the wavefunction depend on the model being used and the observable being analyzed, with reasonable predictions varying widely from 25% [42] to 80% [43]. Reference [44] presents an analytical three-body wavefunction of the $^{11}\text{Li}_{g.s.}$ obtained by fitting much of the existing experimental data for $^{11}\text{Li}_{g.s.}$. These data include the two-neutron separation energy, charge and matter radii for $^{9,11}\text{Li}$, momentum correlations, and interaction cross sections. The calculated wavefunction gives an s^2 strength of 37% with good agreement to all experimental data.

3.3 Excited States

Table 3.2 gives a short summary of the observed excited states of ^{11}Li . The measurements were made using a variety of experimental probes including proton elastic scattering [45], projectile fragmentation [46, 47], and pion capture [48]. The spin assignments given in the table are described in all citations as soft or conjectural. Figure 3.3 gives a summary of the levels plus the various thresholds for the single and multi-neutron decay thresholds for ^{11}Li . An additional $\frac{3}{2}^-$ state has been predicted to lie at $E^* \sim 2.5\text{-}2.8$ MeV [49].

Reference	Reaction	J^π	E^* (MeV)	Γ (MeV)	E_{beam} (AMeV)
[50]	$^{14}\text{C}(\pi^-,pd)$		0.92(15)	~ 0.3	-
[46]	$^{208}\text{Pb}(^{11}\text{Li},^9\text{Li}2n)$		1.0(1)	0.7(2)	281
[48]	$^{14}\text{C}(\pi^-,pd)$	$(\frac{3}{2}^-)$	1.02(7)		-
[47]	$^{12}\text{C}(^{11}\text{Li},^{11}\text{Li}')$		1.24(5)	0.26(24)	265
[45]	$p(^{11}\text{Li},p)$	$(\frac{3}{2}^+)$	1.25(15)	0.75(60)	75
[48]	$^{14}\text{C}(\pi^-,pd)$	$(\frac{3}{2}^+)$	2.07(12)		-
[50]	$^{14}\text{C}(\pi^-,pd)$		2.29(25)	~ 0.7	-
[46]	$^{208}\text{Pb}(^{11}\text{Li},^9\text{Li}2n)$		2.4(1)	2.1(6)	281
[47]	$^{12}\text{C}(^{11}\text{Li},^{11}\text{Li}')$		2.45(27)	2.91(72)	265
[45]	$p(^{11}\text{Li},p)$		3.0(2)		75
[48]	$^{14}\text{C}(\pi^-,pd)$	$(\frac{5}{2}^+)$	3.63(13)		-
[45]	$p(^{11}\text{Li},p)$		4.90(25)		75
[45]	$p(^{11}\text{Li},p)$		6.40(25)		75
[45]	$p(^{11}\text{Li},p)$		~ 11.0		75

Table 3.2: The excited states of ^{11}Li .

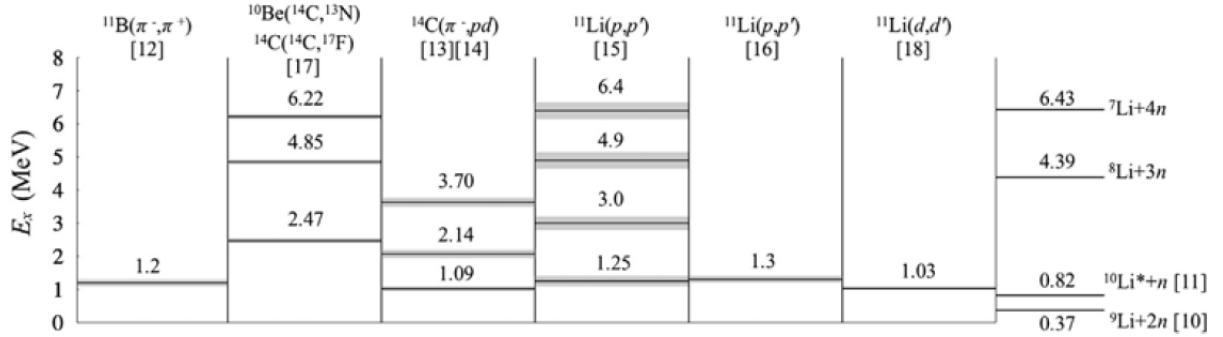


Figure 3.3: Levels and particle-decay thresholds for ^{11}Li . Taken from Ref. [9].

Chapter 4

^{11}O

4.1 Introduction

Exotic nuclei with large differences in their proton and neutron numbers can have unusual structures including halos and low-energy intruder states. ^{11}Li is a textbook example of one of these exotic nuclei, possessing a two-neutron halo which grants it a matter radius commensurate with ^{208}Pb [51]. The halo neutrons have a large probability of inhabiting the $(s_{1/2})^2$ configuration [52]. The mirror of ^{11}Li , ^{11}O , is beyond the proton drip line, and is expected to have a similar structure to ^{11}Li by isospin symmetry. The ground state of ^{11}O , like ^{12}O , is unbound to $2p$ -emission [53].

These unbound protons create a challenge for nuclear theory [54, 55]. Interactions between shell-model states and the continuum can lead to mirror-symmetry breaking due to the Thomas-Ehrman shift [56, 57]. This symmetry breaking due to the continuum is typified by ^{12}O , which has significantly more $(s_{1/2})^2$ occupancy (on the order of tens of percents) than its bound mirror, ^{12}Be . The isospin mass multiplet equation (IMME), obtained by fitting the three neutron-rich members of the $A = 11$ sextet, predicts the ground state of ^{11}O to be unbound by 3.21(84) MeV [21], larger than the decay energy of $^{12}\text{O}_{g.s.}$ by ~ 1.5 MeV. Thus, given that ^{11}O is predicted to be more unbound than ^{12}O , it could be expected

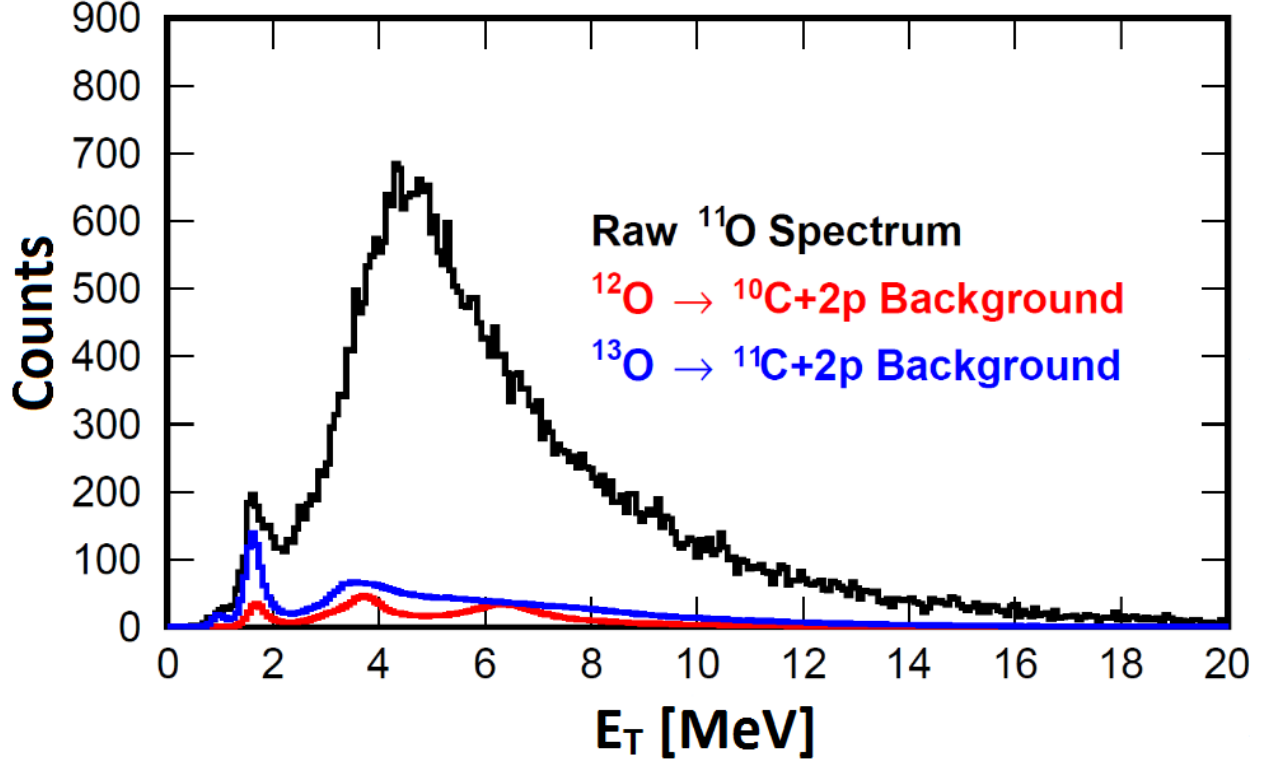


Figure 4.1: Total decay energy spectrum for the $2p$ decay of ^{11}O events. The black curve is generated from detected $2p$ and ^9C fragments, while the red and blue curves show contamination from $2p$ -decaying ^{12}O and ^{13}O nuclei respectively. This contamination is caused by heavier isotopes of carbon leaking into the ^9C gate. There is no transverse gate applied.

that its degree of continuum-triggered mirror-symmetry breaking would be even larger. To understand the impact of the continuum on the nuclear structure of ^{11}O , an experimental and theoretical study has been carried out.

4.2 Decay Energy Spectrum and Contamination

The decay energy (E_T) spectrum for ^{11}O , reconstructed from detected $^9\text{C} + 2p$ events using the invariant-mass method, is shown in the black curve in Fig. 4.1. The peak seen at ~ 1.8 MeV is due to a contamination of decaying $^{12,13}\text{O}$. The red and blue curves that are also displayed show this contamination. In these contaminating events, $^{10,11}\text{C}$ is mistaken for ^9C due to reactions in the CsI(Tl).

These reactions are detailed in Fig. 4.2, which shows ^9C beam elastically scattered into

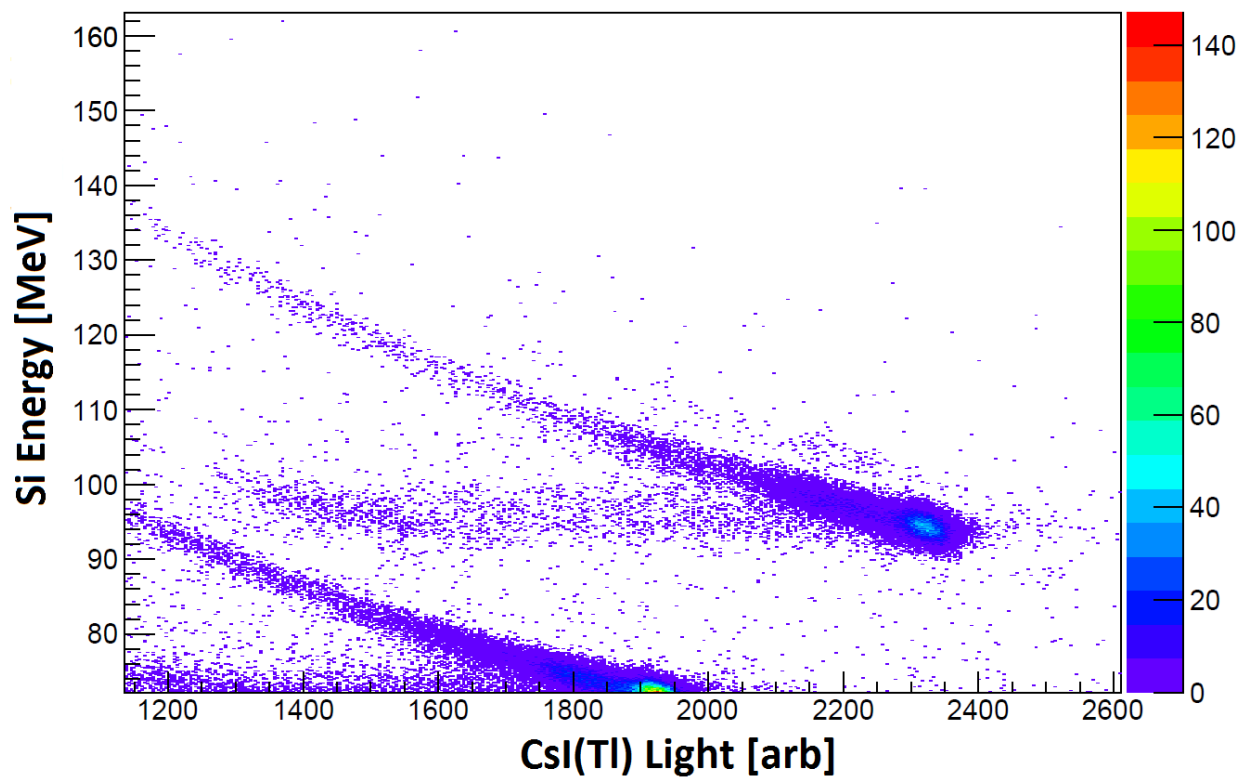


Figure 4.2: A detail of a $\Delta E - E$ plot created during a with the ^9C calibration beam. Notice the streaking heading off to the left. This is due to reactions in the CsI(Tl), the source of the contamination in the invariant mass spectrum of ^{11}O .

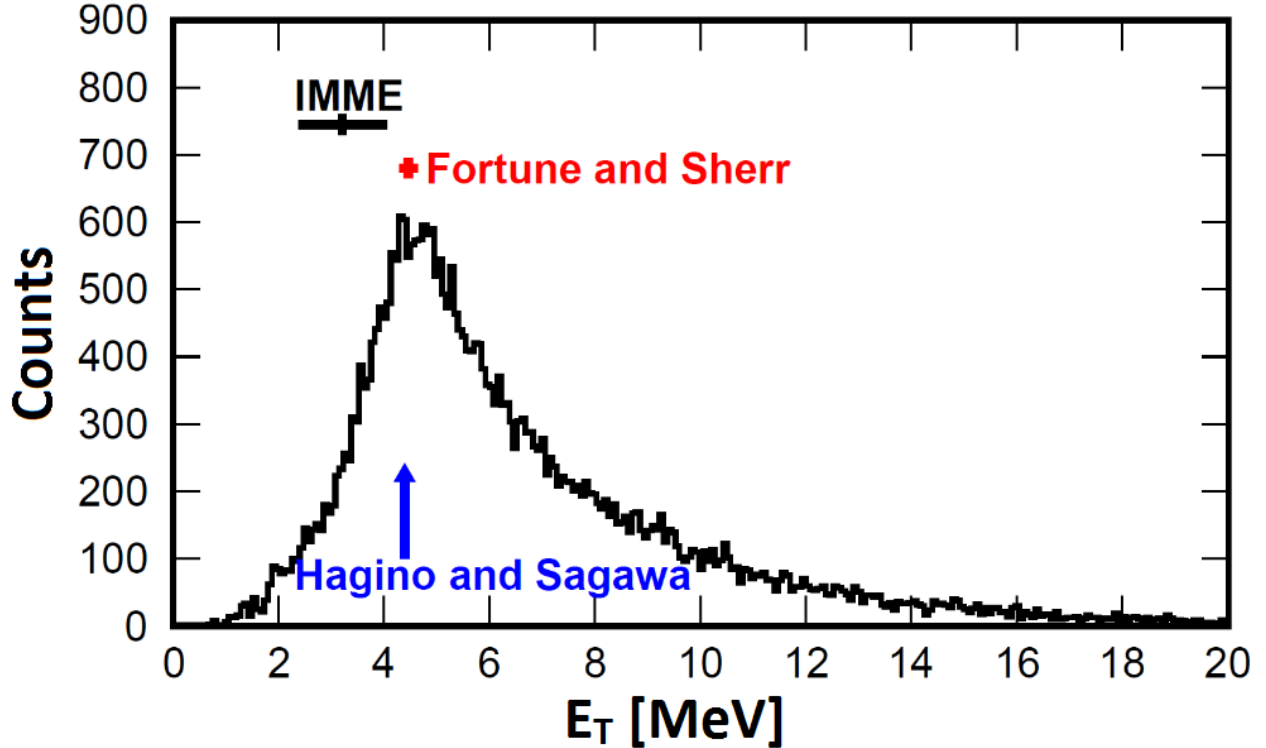


Figure 4.3: The total decay energy spectrum for ^{11}O with the contamination removed. Shown on the same plot are theoretical predictions for the decay energy of the nucleus. No transverse gate is applied.

the central detectors. The streaking along the abscissa is due to reactions in the scintillator which cause light loss. This leads to heavier isotopes of carbon being mistaken for ^9C , as they leak into the PID gates. The red and blue curves in Fig. 4.1 are created by analyzing $^{10,11}\text{C} + 2p$ events as though they are $^9\text{C} + 2p$ events and then scaling the resulting spectra using the ratio of the amount of reacting ^9C beam (the streak shown in Fig. 4.2 to the amount of elastically scattered beam. The ratio is 0.5% for each of the heavy carbon isotopes. The red and blue spectra in Fig. 4.1 were then subtracted from the black spectrum to create an uncontaminated ^{11}O spectrum. This spectrum is shown in Fig. 4.3.

Figure 4.3 also shows three theoretical predictions for the decay energy of $^{11}\text{O}_{g.s.}$. The IMME prediction mentioned earlier is shown in black [21], a prediction using a simple potential model assuming mirror symmetry is shown in red [58], and a three-body model prediction is shown in blue [52].

4.3 Single State Fit

Figure 4.4 shows the subtracted spectrum with a curve fit to the data. This curve is generated by a Monte Carlo simulation using a realistic detector geometry and assuming a diproton decay using the R-matrix prescription [59]. The peak energy is ~ 4.5 MeV, higher than the IMME prediction, and the width (FWHM) is ~ 3 MeV. The experimental resolution at $E_T = 4.5$ MeV is $FWHM = 0.45$ MeV. To obtain a curve from the R-matrix formalism that could fit a width this large, it was necessary to model the diproton lineshape as a delta function centered at $E_{pp} = 0$. This deviates from the assumption of the lineshape based on the $p - p$ phase shift detailed in [59]. This arouses suspicion that the peak is not a singlet, though Fortune was able to obtain a reasonable fit to the data with a single Breit-Wigner peak that models the decay as a coherent sum of simultaneous and sequential $2p$ decay processes [60]. His fit to the data remains too narrow, however, missing data points on the low energy side of the peak.

4.4 Theoretical Model

4.4.1 The Gamow Coupled Channel (GCC) Model

The calculations in this work were performed by Simin Wang of the Nazarewicz group at Michigan State University. The model used was the three-body Gamow Coupled Channel (GCC) model with a ${}^9\text{C}$ core and two protons. The following sections will provide details about the GCC and its application to the ${}^{11}\text{O}$ system. See [19, 61, 62] for greater detail.

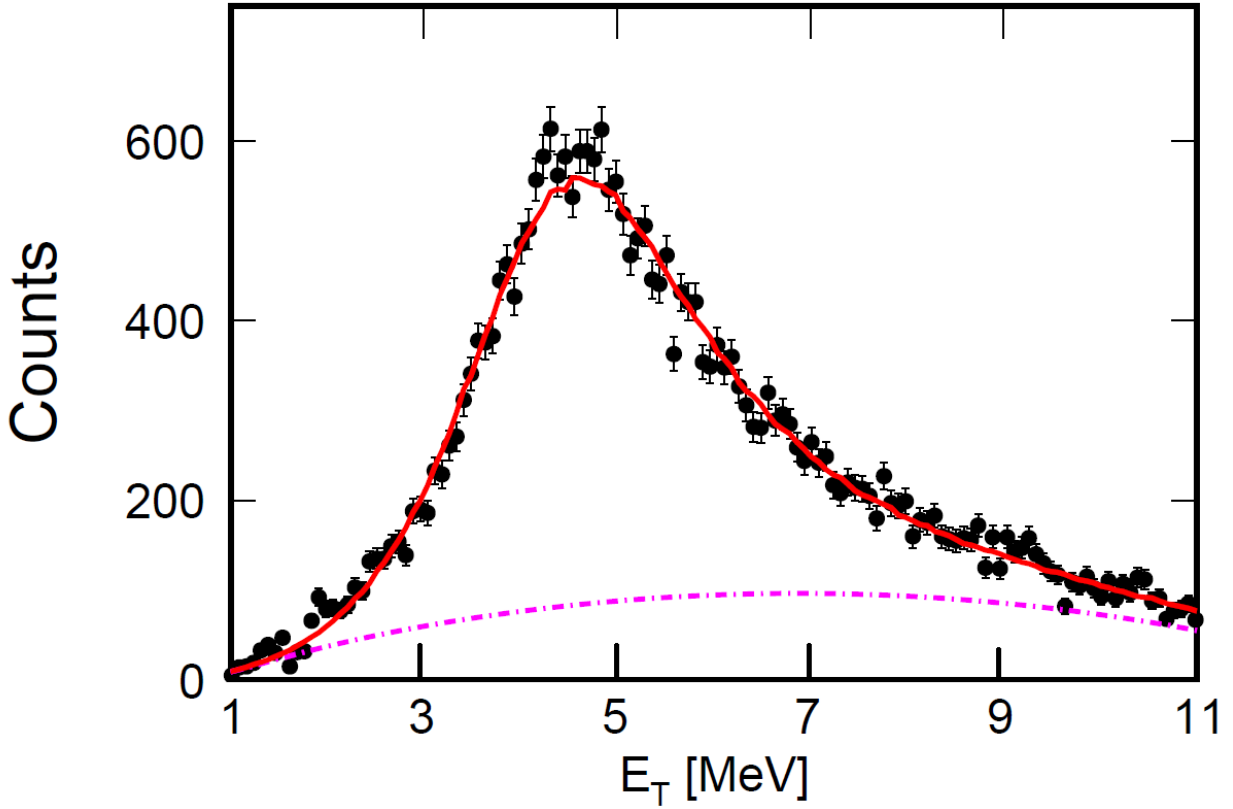


Figure 4.4: A fit to the decay energy spectrum of ^{11}O assuming the peak is created by the decay of a single state in ^{11}O . The curve is generated by Monte-Carlo simulations incorporating the detector response. The dashed line is a fitted background. No transverse gate is applied.

4.4.2 The Three-Body Gamow Coupled Channel (GCC) Model

The three-body GCC models the nucleus as a core and two valence nucleons (or clusters).

The Hamiltonian can be written as

$$\hat{H} = \sum_{i=c,p_1,p_2}^3 \frac{\hat{p}_i^2}{2m_i} + \sum_{i>j=1}^3 V_{ij}(r_{ij}) + \hat{H}_c - \hat{T}_{c.m.} \quad (4.1)$$

where the first sum is the kinetic energy term for each cluster, the second sum describes the two-body interactions between each of the clusters, \hat{H}_c is the core Hamiltonian with associated core excitation energies $E^{j_c\pi_c}$, and $\hat{T}_{c.m.}$ is the center-of-mass term.

The wavefunction of the parent (in our case, the $2p$ -decaying nucleus) is given as $\Psi^{J\pi} = \sum_{J_p\pi_p, j_c\pi_c} [\Phi^{J_p\pi_p} \otimes \phi^{j_c\pi_c}]^{J\pi}$. $\Phi^{J_p\pi_p}$ and $\phi^{j_c\pi_c}$ are the wavefunctions for the valence protons and the core respectively, with $\Phi^{J_p\pi_p}$ being constructed in Jacobi coordinates with a hyperangle piece described by hyperspherical harmonics $\mathcal{Y}_{\gamma K}^{J_p M}(\Omega)$ [63, 64]. The hyperradial piece $\psi_{\gamma K}(\rho)$ is expanded in the Bergren basis $\mathcal{B}_{\gamma n}^{J_p\pi}(\rho)$, a complete ensemble in the complex momentum plane that includes bound, resonant, and scattering states [61]. It is this completeness that makes the Bergren basis useful for describing $2p$ decay, as it reproduces the correct asymptotic behavior and treats reactions and structure on the same footing.

Using hyperspherical harmonics and the Bergren basis allows the Schrödinger equation to be rewritten as a coupled-channel equation with couplings among both the hyperspherical basis and the core's collective states. The complex eigenvalues obtained from solving this equation contain information about the parent resonances' energies and widths.

4.4.3 The GCC Applied to ^{11}O

The core was modeled as a deformed rotor, which allows the coupling of the pair of protons to collective states of the core. As stated before, the wave function is constructed in Jacobi coordinates with a complex-energy basis, which can give exact asymptotic behavior of the wave functions and treats structure and reaction aspects on the same footing. The nuclear

two-body interaction between the valence nucleons is the finite-range Minnesota force [65] augmented by their Coulomb interaction. The effective core-valence potential is a deformed Woods-Saxon (WS) form including the spherical spin-orbit term. The Coulomb core-proton potential is calculated assuming the core charge is uniformly distributed inside its deformed nuclear surface [66].

To analyze Thomas-Ehrman effects [57, 67, 68, 69], the mirror nucleus ^{11}Li has been studied in a similar way with two valence neutrons. The deformed core is described by the quadrupole deformation β_2 , and the couplings to the low-lying rotational states are included. The core rotational energies are taken from Ref. [14]. In the coupled-channel calculations, the g.s. band of the core is included with $J \leq j_c^{max} = 11/2^-$. According to previous work [62], the higher-lying rotational states have little influence on the final energy spectrum and g.s. mass.

Apart from the depth, the other parameters of the core-valence potential were optimized to fit the spectrum of ^{11}N [14]. The resulting values are $V_{S,O} = 15.09$ MeV, $a = 0.7$ fm, the WS (and charge) radius $R = 2.3$ fm, and the quadrupole deformation $\beta_2 = 0.52$. These values are similar to those in Ref. [70], which reasonably reproduces the intruder state of ^{11}Be . The depth V_0 , initially adjusted to fit the spectra of the core+nucleon systems $^{10,11}\text{N}$, is discussed below.

The GCC configurations can be described both in the original Jacobi coordinates (S, l_x, l_y) and the cluster orbital shell model coordinates (j_1, j_2) , where S is the total spin of the valence nucleons and l_x and l_y are, respectively, the orbital angular momenta of two-protons about their center of mass and the center of mass about the core. The calculations have been carried out in the model space of $\max(l_x, l_y) \leq 7$ with the maximum hyperspherical quantum number $K_{max} = 20$. For the hyperradial part, the Berggren basis is used for the $K \leq 6$ channels and the harmonic oscillator basis with the oscillator length $b = 1.75\text{fm}$ and $N_{max} = 40$ for the higher-angular-momentum channels. The complex-momentum contour of the Berggren basis is defined as $k = 0 \rightarrow 0.4 - 0.2i \rightarrow 0.6 \rightarrow 2 \rightarrow 4 \rightarrow 8$ (all in fm^{-1}), with each

segment discretized with 60 points. To study antibound states and broad resonant states in the core-valence potential, the deformed complex-momentum contour is used, as in Refs. [71, 72].

4.5 Results

To benchmark the theory, the g.s. energy of ^{12}O was calculated. The experimental g.s. was fitted with a Breit-Wigner resonance with a centroid of $Q_{2p}=1.688(29)$ MeV and an intrinsic width of $\Gamma=51(19)$ keV. These values for Q_{2p} and Γ are discussed in the next chapter. The GCC calculations give $Q_{2p}=1.97$ MeV and $\Gamma=120$ keV, values in reasonable agreement with experiment. If the depth V_0 of the Woods-Saxon potential is adjusted to reproduce the experimental Q_{2p} value, the theoretical width is now 18_{-3}^{+4} keV, closer to the extracted value. The $(s_{1/2})^2$ strength is now predicted to account for 35% of the wavefunction compared to 20% for the mirror nucleus ^{12}Be calculated with the same parameters, an amount of mirror symmetry violation in accord with the predictions of Ref. [56].

Using the initial estimate of V_0 , values of $Q_{2p}=3.17$ MeV, $\Gamma=0.86$ MeV are obtained for $^{11}\text{O}_{g.s.}$, which does not explain the experimental peak. To investigate whether the peak can be a singlet, the depth of the WS potential was varied to examine how the decay width changes. When Q_{2p} is set at 4.55 MeV, near the maximum of the experimental peak, the decay width is only 1.29 MeV, with 67.7% strength in the $(K, S, l_x) = (0, 0, 0)$ configuration. Because this configuration is largely responsible for the decay rate [56], a maximum value of $\Gamma=1.29/0.67\approx 1.9$ MeV is obtained. Another estimate for the width can be obtained by assuming no valence-nucleon interaction and recoil term. Based on the three-body model, the g.s. energy and decay width of ^{11}O would be two times larger than that of ^{11}N . Thus, the decay energy Q_{2p} should be ~ 4 MeV with a width of ~ 1.5 MeV, significantly less than the experimental values. Due to the difficulty in the theory reproducing the experimental peak, the observed spectrum must contain multiple components.

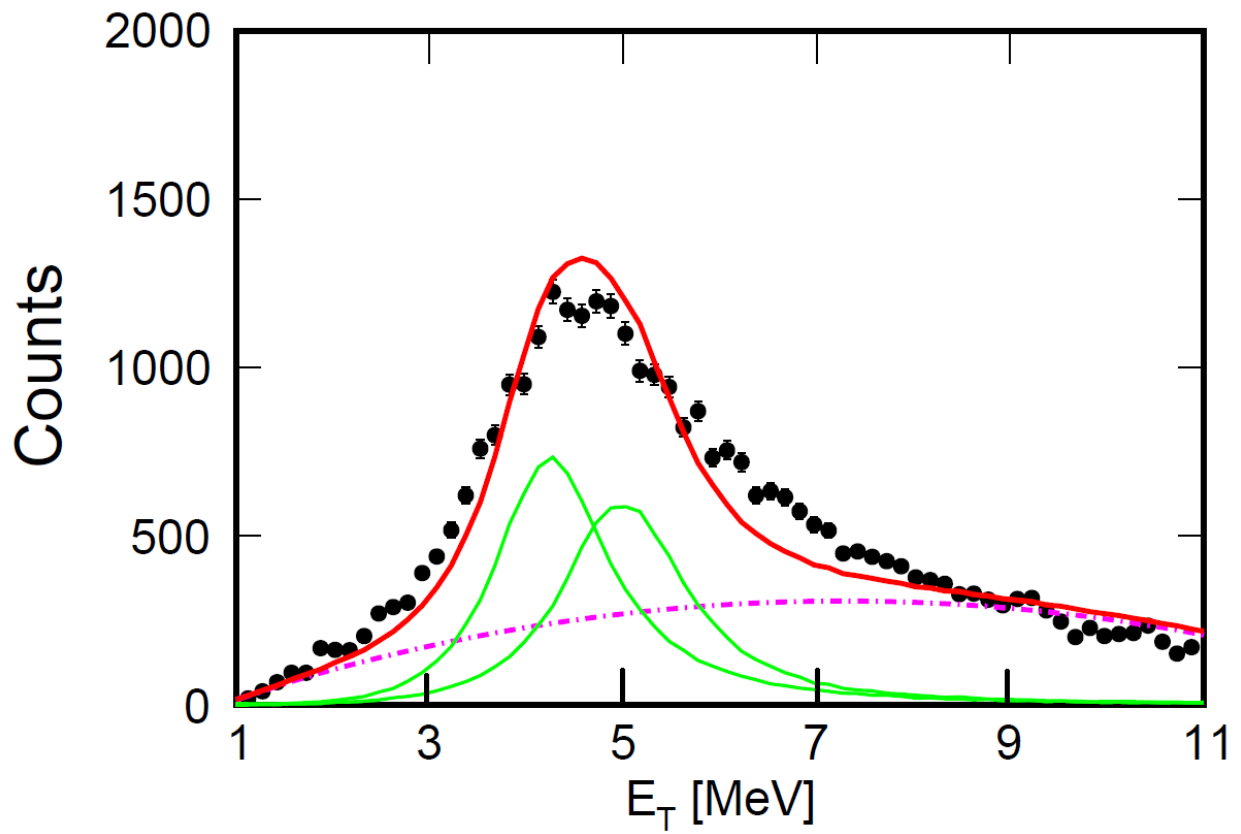


Figure 4.5: A fit to the ^{11}O decay energy spectrum assuming that the peak consists of two $3/2^-$ states. No transverse gate is applied.

J^π	Q_{2p} (MeV)	Γ (MeV)
$3/2_1^-$	4.16	1.30
$5/2_1^+$	4.65	1.06
$3/2_2^-$	4.85	1.33
$5/2_2^+$	6.28	1.96

Table 4.1: The decay energies, Q_{2p} , and widths, Γ , of the four lowest-lying resonant states of ^{11}O .

The possibility that the experimental peak is a doublet of two predicted $3/2^-$ states was considered. Attempts to reproduce the experimental peak by varying the depth of the WS potential to change Q_{2p} and using the calculated line shapes to fit the data failed as the best-fit spectrum is still too narrow, as seen in Fig. 4.5. Thus, contributions from two $5/2^+$ states must be included. To populate these states, the two neutrons knocked out of the ^{13}O beam must come from different shells to conserve parity. An analogous state was observed in the mirror reaction, the two-proton knockout from ^{13}B populating the first excited state of ^{11}Li , which has positive parity [73, 74, 9]. This state is consistent with the $5/2_1^+$ ^{11}Li state obtained by GCC calculations. Table 4.1 gives the energies, Q_{2p} , and widths, Γ , for the four lowest-lying resonant states obtained with V_0 optimized to the observed decay energy spectrum. Figure 4.6 shows the best fit to the data with the contributions from all four of these levels. The line shapes are generated using a Monte-Carlo code that takes experimental resolution into account. With a smooth background, the data are well described. The $3/2_1^-$ and $5/2_2^+$ states make up most of the yield, at 39% and 32% strength respectively. The $3/2_2^-$ and $5/2_1^+$ levels have similar widths and centroids and cannot be well distinguished. Figure 4.7 shows the IMME curve obtained from a fit to the three neutron-rich members of the $A = 11$, $T = 5/2$ sextet: ^{11}Li , $^{11}\text{B}_{IAS}$, and $^{11}\text{Be}_{DIAS}$ [33, 25, 21]. The value shown for ^{11}O is that of the ground state, the state labeled $3/2_1^-$ in Table. 4.1. It appears that the IMME under-predicts the mass.

A decay energy spectrum of transversely decaying $2p+^9\text{C}$ events ($\cos\theta_k < 0.2$) is shown in Fig. 4.8(b). There is a clear enhancement of a high-energy feature near $E_T = 6$ MeV. This is near the energy of the $5/2_2^+$ state predicted by the GCC. Indeed, when fit with the

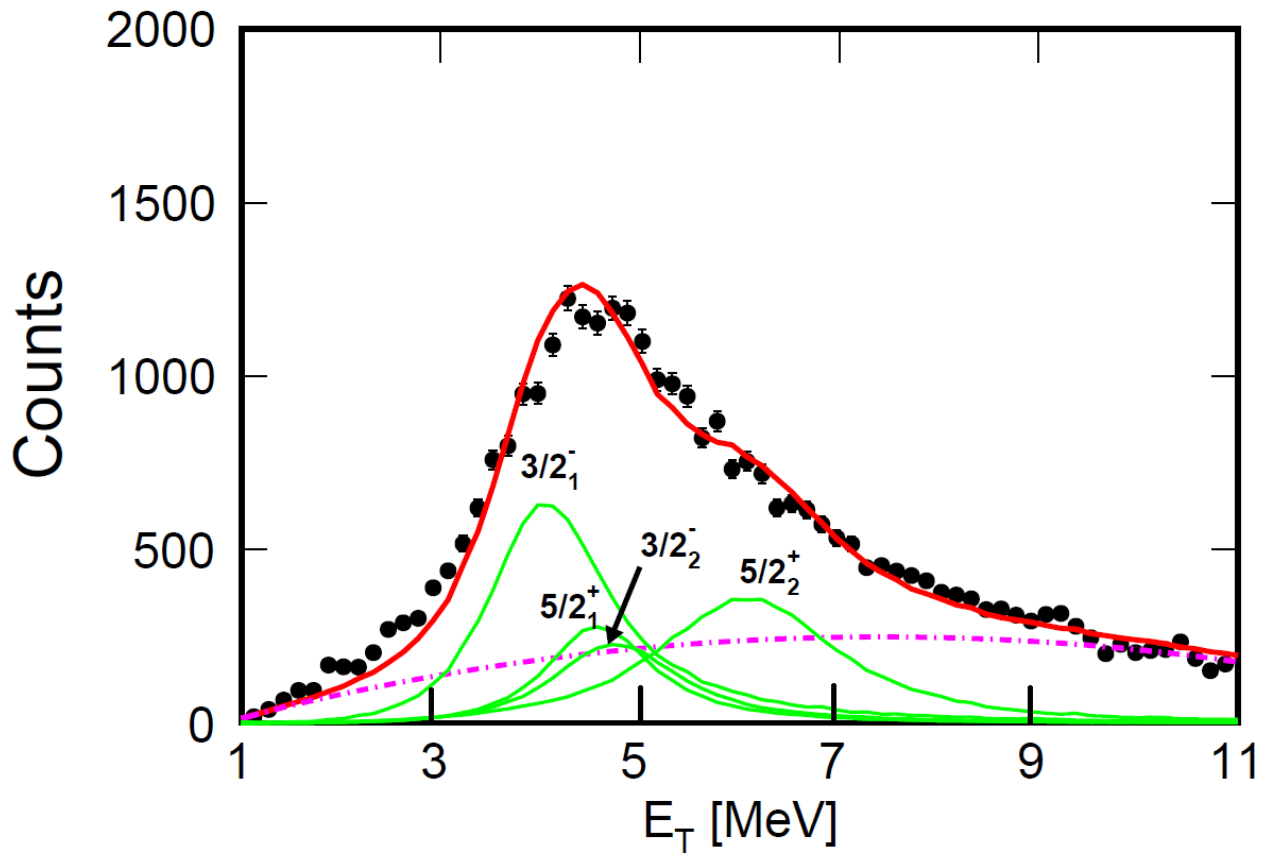


Figure 4.6: A fit to the ^{11}O decay energy spectrum assuming that the peak consists of four states, two of $J^\pi = 3/2$ and two of $J^\pi = 5/2$. No transverse gate is applied.

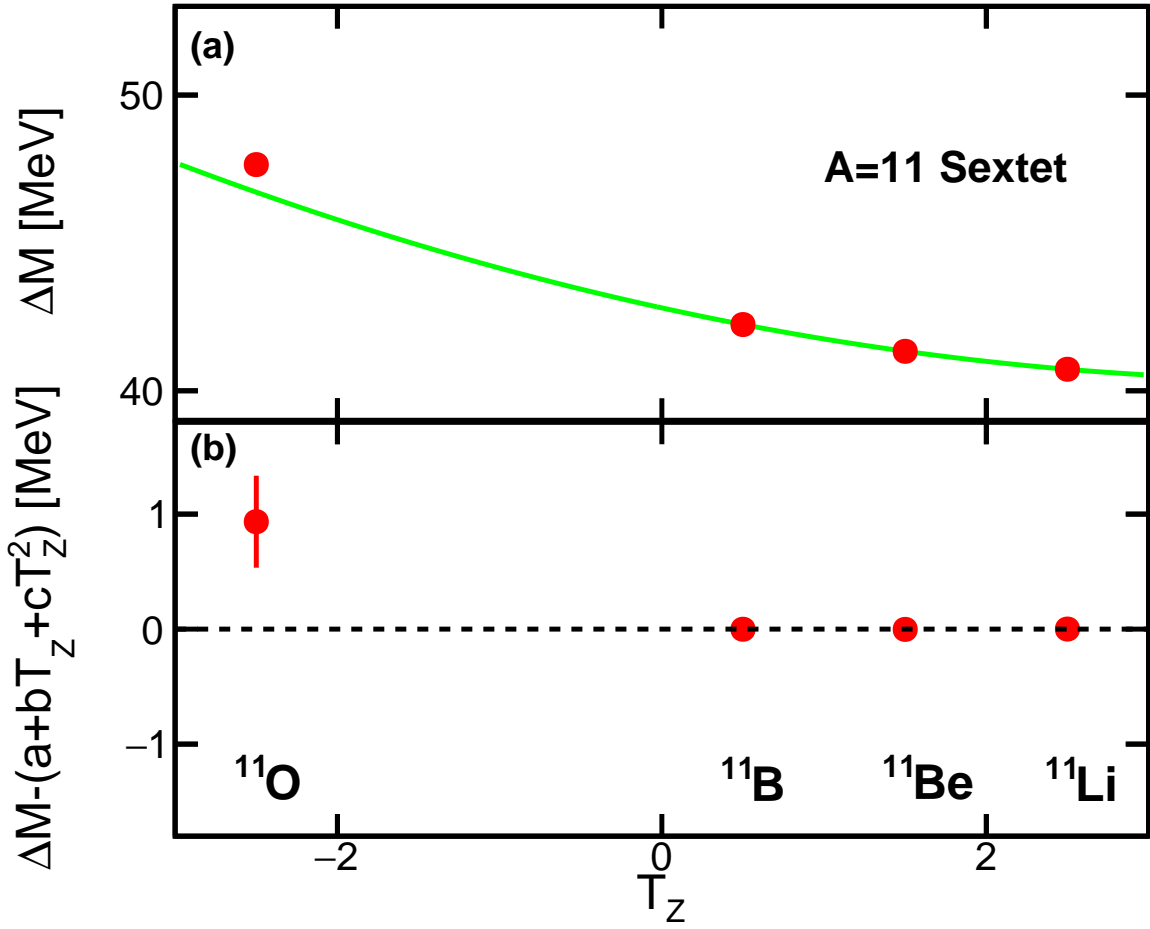


Figure 4.7: (a) The IMME curve obtained by fitting the three neutron members of the $A = 11$, $T = 5/2$ sextet and the masses of the four known members and (b) the residuals of these masses with the curve. The mass for ^{11}O is taken from the first $J^\pi = 3/2^-$ level of the GCC calculation that reproduced the fit.

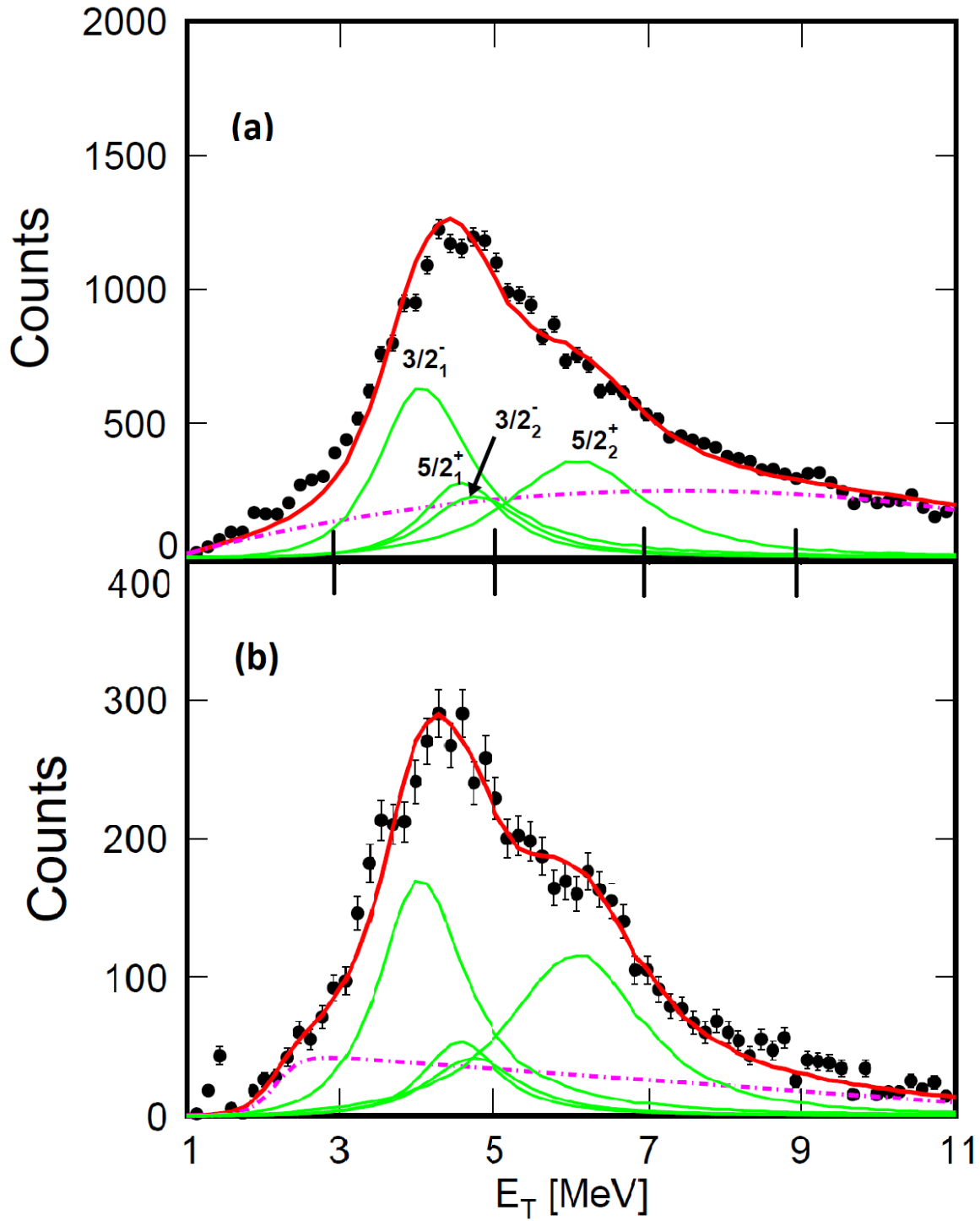


Figure 4.8: A fit to the ^{11}O decay energy spectrum (a) with no transverse gate and (b) for events decaying transversely to the beam ($\cos\theta_C < 0.2$). There is a clear enhancement of a high-lying feature relative to the spectrum that includes all events. This feature appears to sit at the energy of the second $5/2^+$ state.

four states predicted by the GCC, we obtain a reasonable fit also shown in Fig. 4.8. This adds further support to our claim that the broad peak is in fact a multiplet.

The dependence of the predicted widths on Q_{2p} is complicated by the presence of broad threshold resonant states in ^{10}N , which affect the behavior of the $l = 0$ single-particle channel. Figure 4.9(a) shows the $2p$ partial decay widths of the $3/2^-$ resonant states of ^{11}O as a function of Q_{2p} . The predicted decay width of the $3/2_1^-$ g.s. increases rapidly with Q_{2p} below the Coulomb barrier (~ 3.2 MeV). This increase is accompanied by a rapid configuration change, shown in Fig. 4.9(b). The wave function of this state is dominated by the single $(S, l_x, l_y) = (000)$ Jacobi-coordinate component. For $Q_{2p} < 2.2$ MeV, the weight of the $(s_{1/2})^2$ shell-model component is around 20%, similar to predictions for the ^{11}Li . As Q_{2p} gets larger, the $(s_{1/2})^2$ strength rapidly increases. Close to the Coulomb barrier, the state becomes a pure $(s_{1/2})^2$ configuration. Above the barrier, the wave function has a small amplitude inside the nuclear volume and can no longer be associated with an outgoing solution; it dissolves into the scattering continuum. Interestingly, as seen in Fig. 4.9(a), a second branch of the $3/2_1^-$ solution appears at higher Q_{2p} values. This behavior is attributed to the presence of a broad resonant state in the $l = 0$ p - ^9C scattering channel, which is an analog of the antibound state of ^{10}Li . When steadily increasing the Coulomb interaction from zero (n - ^9Li) to the full p - ^9C value at $V_0 = -52.17$ MeV ($Q_{2p} = 4.13$ MeV), this resonant pole evolves in the complex- k plane from the antibound state in ^{10}Li with $k = -0.222i$ fm $^{-1}$ ($E = -1.022$ MeV), passing the region of subthreshold resonances $\text{Re}(E) < 0$ and $\Gamma > 0$, located below the -45° line in the momentum plane[75, 76], and eventually becoming the broad s -wave threshold resonant state in ^{10}N with $k = 0.252 - 0.213i$ fm $^{-1}$ ($E = 0.38$ MeV, $\Gamma = 4.45$ MeV), see Ref. [77]. The antibound-state analog is present in the broad range of Q_{2p} values, and is the source of the discontinuity between the two branches for the $3/2_1^-$ state when it gets close to the -45° line.

The second $3/2_1^-$ solution shows a similar trend to the first one, with the amplitude of the $(s_{1/2})^2$ configuration increasing with Q_{2p} . The fitted value of Q_{2p} for the g.s. corresponds

to the second solution in Fig. 4.9 and contains 29% of the $(s_{1/2})^2$ configuration compared to a similar value of 25% for the mirror ^{11}Li . However, at other values of Q_{2p} , the degree of isospin symmetry breaking would have been substantial. The $3/2_2^-$ state exhibits a similar discontinuity as the $3/2_1^-$ solution; the dependence of the $3/2_2^-$ $(s_{1/2})^2$ strength on Q_{2p} is roughly inverted to that for the $3/2_1^-$ state in Fig. 4.9(b), with the excited-state component dropping to zero when the ground-state approaches the pure $(s_{1/2})^2$ configuration.

4.6 Dinucleon Correlations

One can see the Thomas-Ehrman effect directly in the wave functions of the valence nucleons. Figure 4.10 shows that the predicted two-nucleon density distributions in Jacobi coordinates for the $3/2_1^-$, $5/2_1^+$, and $3/2_2^-$ resonant states of ^{11}Li and ^{11}O . The two $3/2^-$ states show strong correlations between the valence nucleons with either diproton or dineutron characteristics. As expected, the diproton peak in the unbound ^{11}O is slightly less localized than that of the dineutron configuration in the bound mirror halo system. However, the secondary peak strength for cigar-like arrangements is significantly reduced in ^{11}O . The two-nucleon correlations for the $5/2_1^+$ state are weak, with the maximum density occurring for large separations between the two valence nucleons. The $5/2_1^+$ wave function is more extended spatially in ^{11}O than in ^{11}Li . This resonance is dominated by the $(s_{1/2}, p_{1/2})$ component, while the $5/2_2^+$ level in ^{11}O is dominated by the $(s_{1/2}, p_{3/2})$ component.

4.7 Conclusions

The proton-unstable isotope ^{11}O has been observed for the first time. It was produced by two-neutron knockout reactions from a ^{13}O beam. The invariant-mass spectrum of its $2p+^9\text{C}$ decay products measured with the HiRA detector contained a single broad peak with a width of 2.9 MeV. The low-energy structure of ^{11}O was also studied theoretically with the Gamow coupled-channel approach and it was shown that the observed peak is most likely

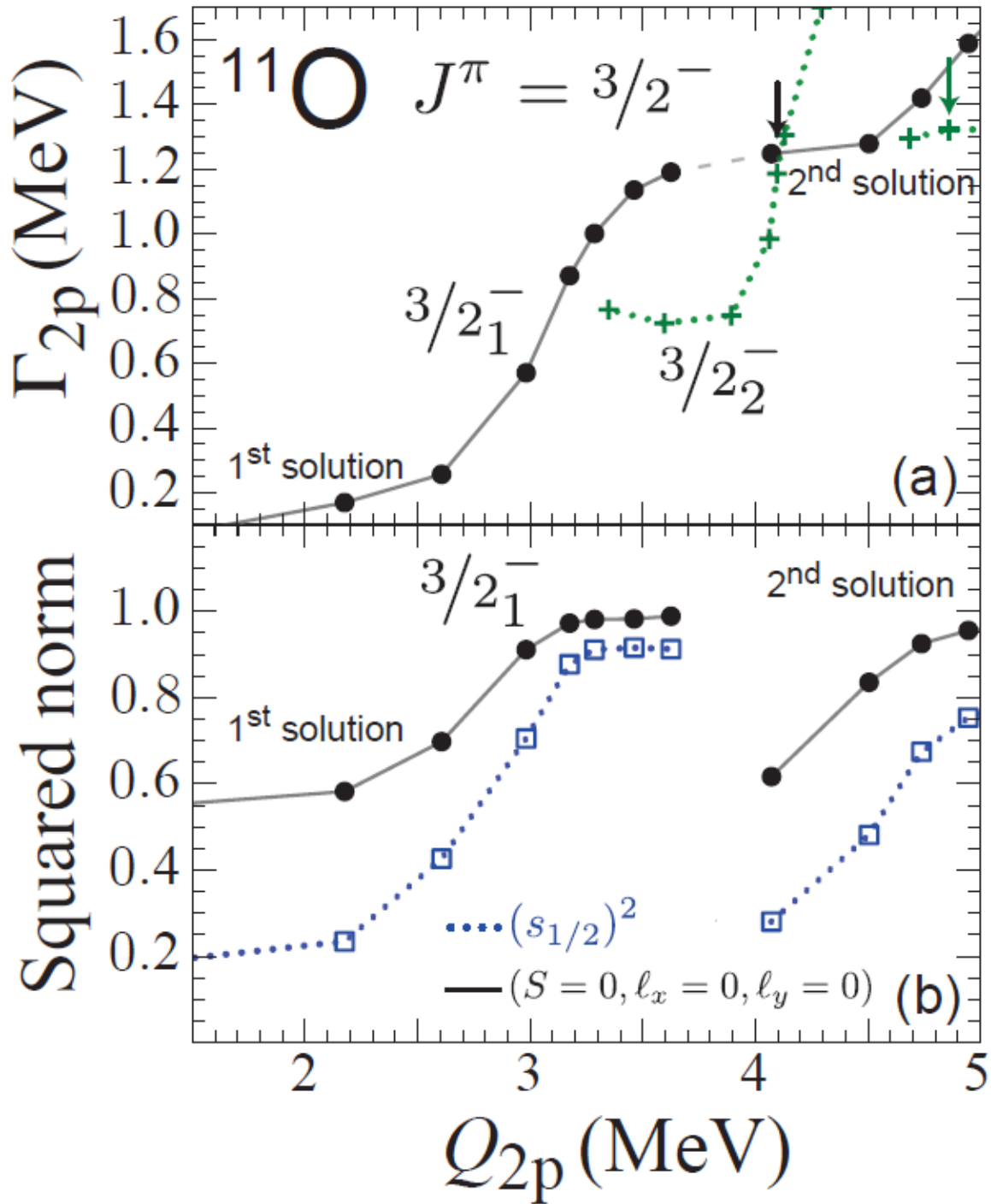


Figure 4.9: (a) Predicted widths for the $3/2_1^-$ (both solutions) and $3/2_2^-$ resonant states of ^{11}O as a function of Q_{2p} . The arrows indicate the predicted Q_{2p} values of the $3/2_1^-$ and $3/2_2^-$ states. (b) GCC configuration weights (real parts of squared norms) of the $(s_{1/2})^2$ and $(Sl_x l_y) = (000)$ configurations in the $3/2_1^-$ wave function.

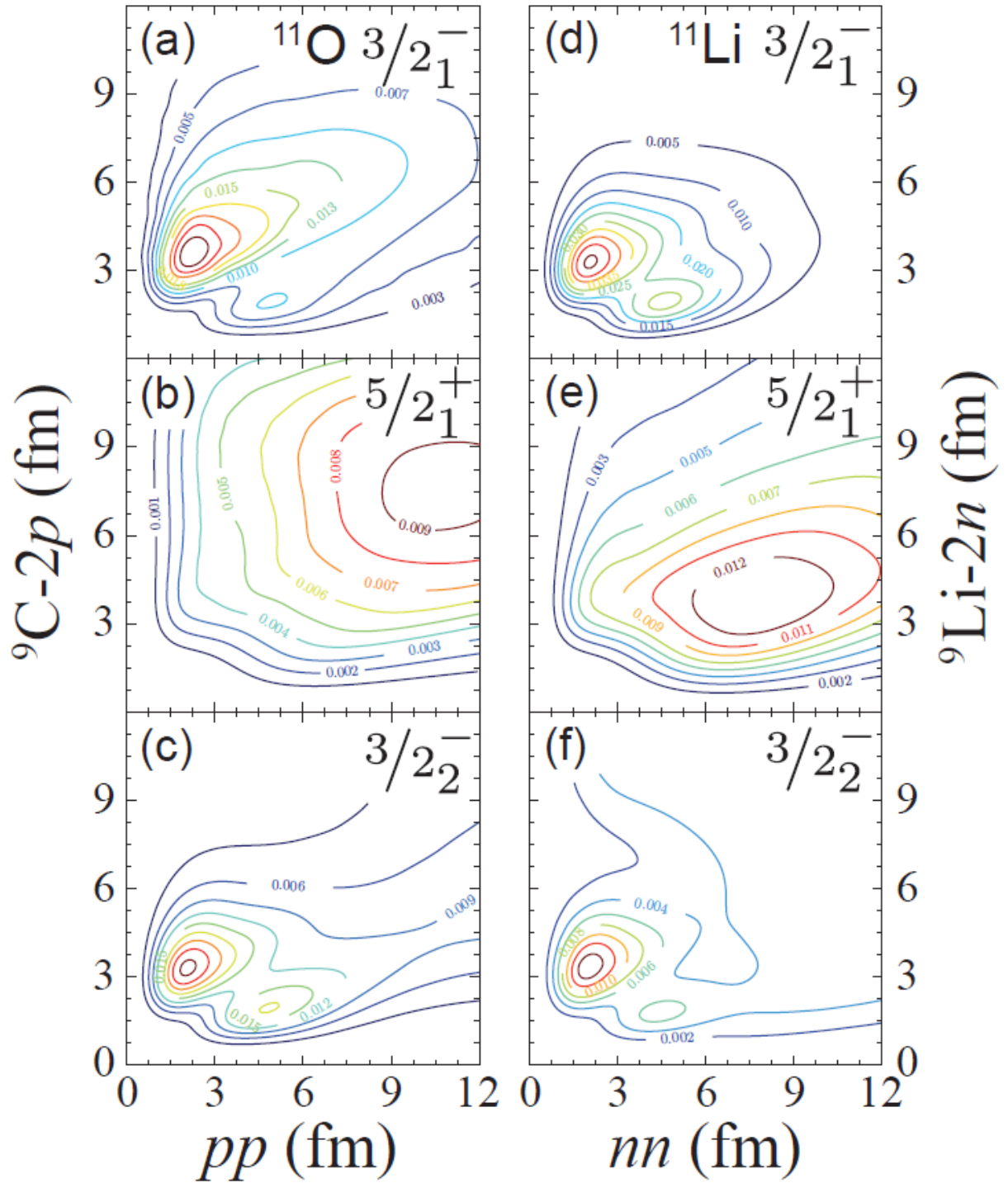


Figure 4.10: Two-nucleon density distributions (in fm^{-2}) in Jacobi coordinates predicted in GCC for low-lying resonant states in ^{11}O (left) and ^{11}Li (right).

a multiplet. An excellent fit to this structure was obtained, with contributions from the four-lowest excited resonant GCC states ($J^\pi = 3/2_1^-, 5/2_1^+, 3/2_2^-, 5/2_2^+$).

The predicted width of the $3/2_1^-$ g.s. shows complicated variation with the depth of the confining potential due to the presence of broad resonant states in the p - ^9C scattering $l = 0$ channel. With the fitted depth, the g.s. configuration was found to be similar to its mirror system ^{11}Li . However, significantly different configurations were predicted for other values of the depth. These results demonstrate the importance of the coupling to the continuum for states beyond the drip lines and the role that $l = 0$ near-threshold resonant states can play in constructing the many-body wave functions. The Thomas-Ehrman effect was also studied directly in the wave functions of the valence nucleons in the mirror ^{11}O - ^{11}Li pair. According to the calculations, the strength in the diproton (cigar) configuration is relatively stronger (weaker) in the g.s. of ^{11}O than in ^{11}Li .

Chapter 5

^{12}O

5.1 Introduction

Isotopes near and beyond the drip lines can show unusual properties like extended halos, two-nucleon emission, and low-energy intruder states. They also present a theoretical challenge as coupling to the continuum needs to be included, which can result in clusterization [78] and the breaking of isospin symmetry due to Thomas-Ehrman effects [79, 80].

The $2p$ decay of ^{12}O has been previously observed [81, 53]. The invariant-mass method can be used in 3-body decays to investigate the momentum correlations between the decay fragments. These correlations can capture information about the decay dynamics and the parent states' structure. High-statistics measurements of these correlations have been made for the democratic $2p$ decay of the ground states of ^6Be and ^{16}Ne , and the correlations were compared to predictions from three-body calculations [10, 11]. Momentum correlation measurements have only been made for the ground state in ^{12}O with low statistics [81].

The isobaric analog of ^{12}O in ^{12}N was shown to undergo prompt $2p$ decay to the isobaric analog state (IAS) in ^{10}B [53]. This is the second observed case of prompt $2p$ decay from one IAS to another, the first case being $^8\text{B}_{IAS} \rightarrow 2p + ^6\text{Li}_{IAS}$ [82, 83]. It is interesting to determine if the $2p$ decays of these analog states have the same momentum correlations

Nuclide	J_π	E_{lit}^* [MeV]	Γ_{lit} [keV]	E^* [MeV]	Γ [keV]
^{12}N	2^+	0.960(12)	<20	0.962(3)	
^{12}N	2^-	1.179(17)	55(14)	1.186(7)	77(12)
^{13}O		3.025(16)	<0.050	3.038(9)	
^{13}O		3.669(13)	<0.050	3.701(10)	

Table 5.1: Comparison of fitted and literature decay energies and widths of calibration resonances used for detector characterization. Literature values for ^{12}N states come from [17] and values for ^{13}O states from [18].

as their ground-state cousins. It is also interesting to learn about the decay dynamics of the higher-lying analog states, that is if they undergo prompt or sequential $2p$ decay to the $^{10}\text{B}_{IAS}$.

5.2 ^{12}O Structure

5.2.1 Calibration resonances

The structure of ^{12}O can be investigated via the invariant-mass spectra of the decay fragments. Peaks corresponding to particle-decaying states found in the invariant-mass spectra were fit to extract the resonance energy and intrinsic width of the states. The experimental resolution and efficiency are included via Monte-Carlo simulation. These simulations are benchmarked by comparing their results to well-known resonances that decay through similar decay channels.

Figures 5.1(a) and (b) show the excitation-energy spectra for particle-decaying states of ^{13}O and ^{12}N from detected $2p+^{11}\text{C}$ and $p+^{11}\text{C}$ events respectively. The curves show fits assuming Breit-Wigner line shapes. A comparison of the fitted parameters for these states and the ENSDF values are shown in Table 5.2.1. The width of the peak corresponding to the 2_1^+ state is essentially only from the experimental resolution, as the reported width of the state is much smaller than the experimental resolution.

The peaks in the $2p+^{11}\text{C}$ spectrum have only been seen in a single previous study [18]. Again, the width is dominated by the experimental resolution. The centroid for the lower-

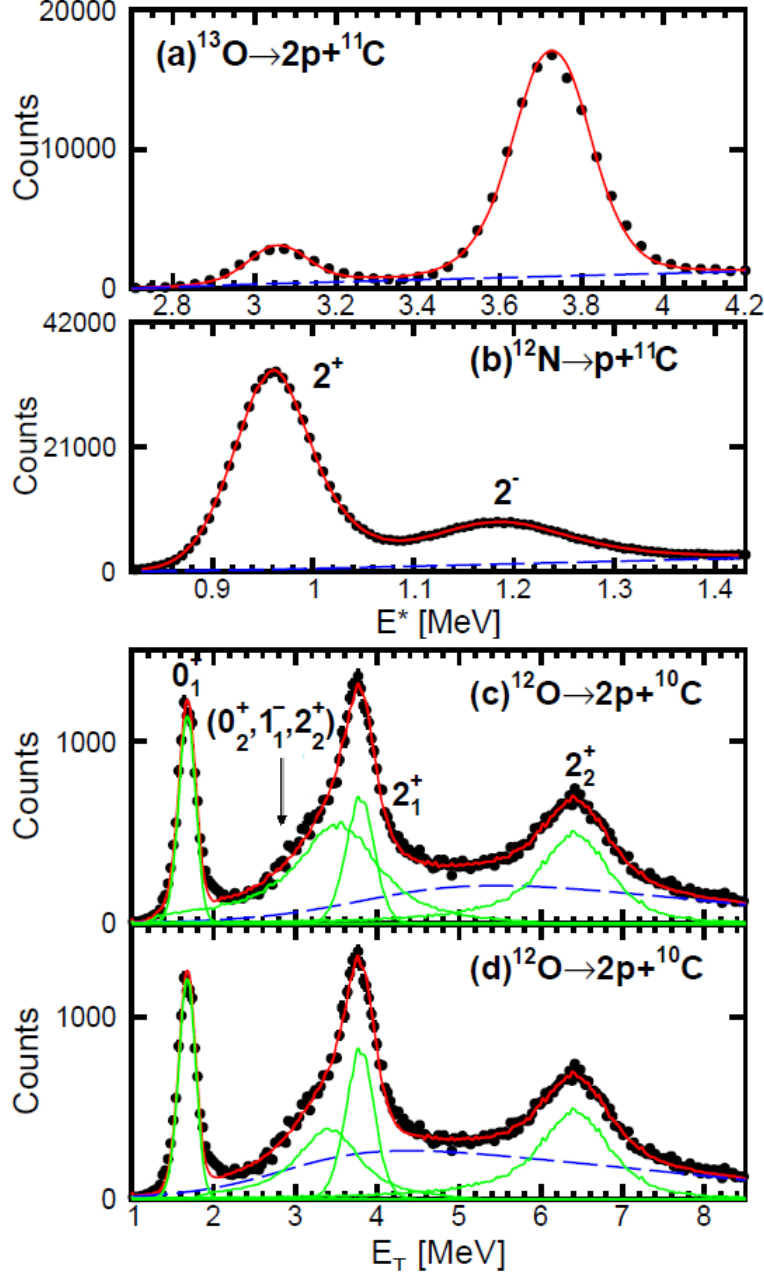


Figure 5.1: Excitation-energy spectra of calibration peaks for (a) the first $2p$ -decaying levels of ^{13}O and (b) the first two excited states of ^{12}N reconstructed from transversely decaying $2p+^{11}\text{C}$ and $p+^{11}\text{C}$ events respectively. The red solid curves show the results of Monte Carlo simulations incorporating the detector response and known level properties. The blue dashed curves are fitted estimations of the background. Total decay energy spectra (c),(d) of ^{12}O reconstructed from transversely decaying $2p+^{10}\text{C}$ events. (c) shows a fit at the upper limit of the uncertainty for the 0_2^+ width while (d) shows the fit at the lower limit. The red solid curve shows the summed results of Monte-Carlo simulations of each resonance, shown by the solid green curves. The blue dashed curve shows the fitted background. A $|\cos\theta_C| < 0.2$ gate was applied for all spectra.

energy peak is consistent with the previous value, while the higher-energy one is slightly higher than the previously reported value. From previous experience, we expect a systemic error of ~ 10 keV, which is not included in the uncertainties listed in Table 5.2.1. The reproduction of these known resonances thus assures us that our simulations are correctly incorporating the detector response.

5.2.2 $2p + {}^{10}\text{C}$ channel

The total decay energy (E_T) spectrum for the $2p$ -decay of ${}^{12}\text{O}$ is shown in Figs. 5.1(c) and (d). There are four peak structures in the spectrum. The spin assignments of the three prominent features come from an analysis of the mirror nucleus ${}^{12}\text{Be}$ [84], the predictions of [19, 85, 86], and previous measurements [53]. The low-energy shoulder on the 2_1^+ peak is at the approximate location of the second 0^+ state, reported at $E^* = 1.62(13)$ MeV [12]. It is also at the approximate location of the 1_1^- state predicted by GCC calculations ($E_T=3.256$ MeV)[19]. The shoulder could also be a decay branch of the 2_2^+ excited state to the particle-bound first excited state of ${}^{10}\text{C}$ ($E^* = 3.353$ MeV, $J^\pi = 2^+$), as the shoulder is located ~ 3.353 MeV lower than the ground state decay channel of the 2_2^+ state.

J_π	E_T [MeV]	E^* [MeV]	Γ [MeV]	σ [mb]
0_1^+	1.718(15)	0	0.051(19)	0.72(1)
0_2^+ ¹	3.519(67)	1.801(67)	0.980(182)	2.01(78)
2_1^+	3.817(18)	2.099(18)	0.155(15)	1.25(10)
2_2^+	6.493(17)	4.775(17)	0.754(25)	2.13(9)
2_2^+ ²	6.493(17)	4.775(17)	0.754(25)	2.88(9)
	7.792(40) ³	6.254(40)	0.81(11)	0.40(5)

¹ Assuming the shoulder peak is the second 0^+ ;

² Assuming the shoulder peak is a decay branch of the second 2^+ ;

³ Through the $4p + 2\alpha$ decay channel.

Table 5.2: The spin assignments, decay energies, intrinsic widths, and measured cross sections of the four observed states in ${}^{12}\text{O}$.

The data were fit with Monte-Carlo simulations using Breit Wigner intrinsic line shapes that account for the detector response, as previously described. The numerics, extracted decay energies, widths, and cross sections are given in Table 5.2. The decay width of the shoulder is subject to large uncertainty, as demonstrated by the fits with different backgrounds in Figs. 5.1(c) and (d). The fitted decay energy and width are consistent with the values of $E^*=1.62(3)$ and $\Gamma=1.2$ MeV given for the 0_2^+ state in [12]. If the shoulder is in fact actually a decay branch of the second 2^+ , we can fix its decay energy and width and refit the spectrum, obtaining a branching ratio of 0.27(1).

This work also presents the first observation of a second 2^+ state, which was predicted to be produced in ^{13}O knockout reactions in [85]. The analysis of [85] predicts four 2^+ states, though only two are expected have significant strength (the first and fourth). The fourth (presumably the new 2_2^+ state) should have four times the yield of the 2_1^+ state, which is not observed.

5.2.3 $4p + 2\alpha$ channel

Figure 5.2(a) shows the reconstructed decay energy spectrum of coincident $4p+2\alpha$ events found in our detectors. The spectrum shows a clear peak sitting on top of a large background. A fit with a single level with a Breit-Wigner line shape is shown as the solid red curve, and has parameters $E_T=7.972(40)$ MeV, $\Gamma=0.81(11)$ MeV.

It is not easy to disentangle how this state decays due to the large multiplicity of exit-channel fragments and the large background. Among the most interesting of the possible decay scenarios include sequential decay pathways initiated by the fission-like $\alpha+^8\text{C}/^6\text{Be}+^6\text{Be}$ or $2p$ decay to higher-lying excited states of ^{10}C . In these scenarios, sequential decays of the unstable decay products lead to the observed exit channel.

Of the possible intermediate states, $^8\text{Be}_{g.s.}$ is the easiest to isolate because there is only one possible α - α subevent in each $4p+2\alpha$ event. The α - α invariant-mass peak also has no background under it. The $4p+2\alpha$ spectrum gated on and vetoed by the presence of a ^8Be

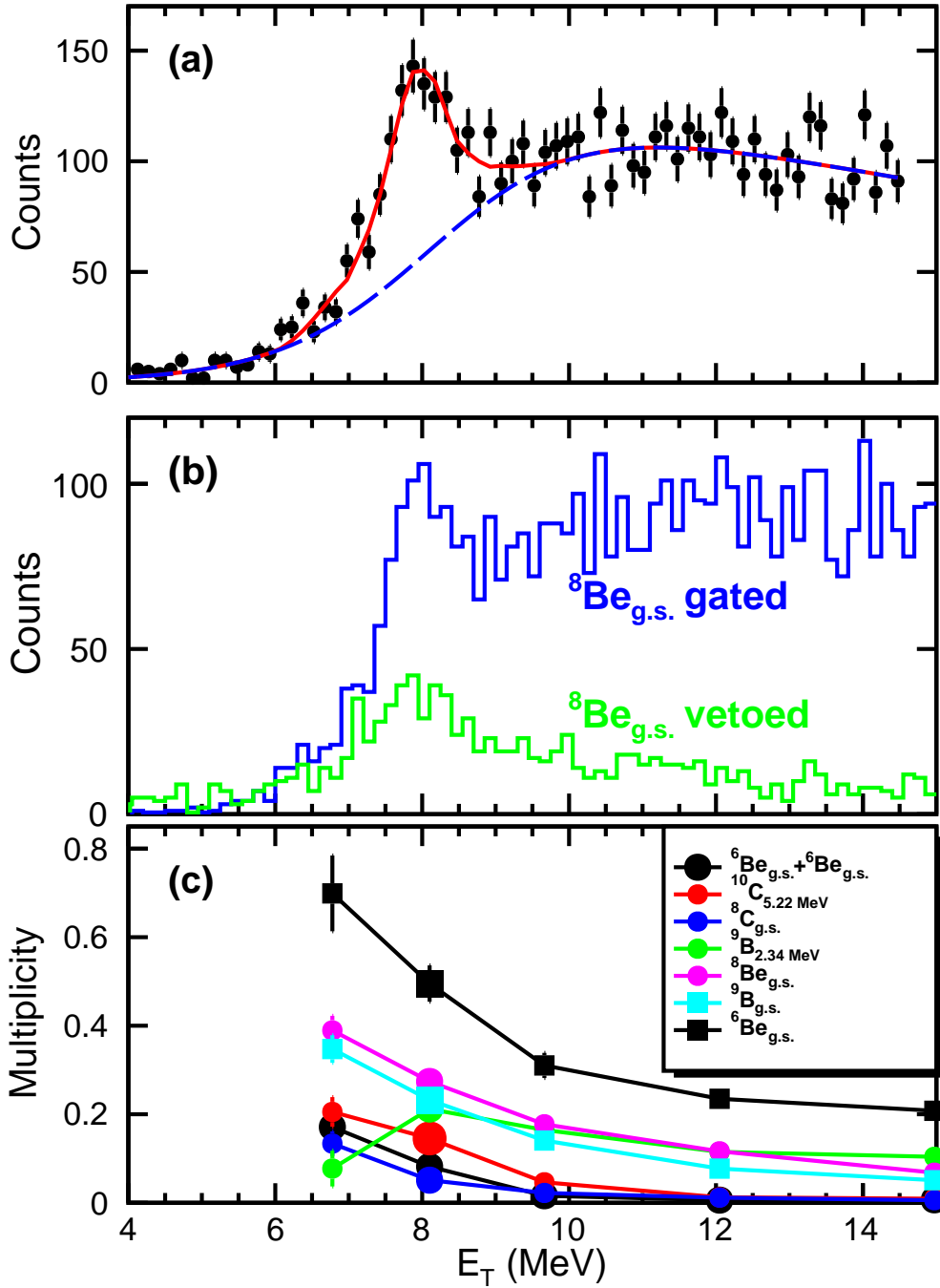


Figure 5.2: (a) Total decay energy spectrum reconstructed from coincident $4p+2\alpha$ events. The red solid curve shows the result of a Monte-Carlo simulation with a Breit-Wigner intrinsic line shape. The blue dashed curve shows the fitted background. (b) Coincident $4p+2\alpha$ events with a gate on and a gate vetoing ${}^8\text{Be}_{g.s.}$ intermediate states, and (c) the multiplicity of observed intermediate resonances assessed at five different points along the spectrum. Also included is the probability of observing a ${}^6\text{Be}_{g.s.}+{}^6\text{Be}_{g.s.}$ fission event. No $\cos\theta_C$ gate was employed.

intermediate state is shown in Fig. 5.2(b). The prominent peak is present in both spectra, which indicates that there are at least two decay pathways. As we will see shortly, there are in fact many more.

We can identify other possible intermediate states by examining other combinations of the decay fragments. As an example, consider the invariant-mass spectrum of $4p+\alpha$ events shown in Fig. 5.3(c). There are two ways to reconstruct $4p+\alpha$ events from each detected $4p+2\alpha$ event. There is a peak in this spectrum at $E_T=3.449$ MeV, which is associated with the decay of ${}^8\text{C}_{g.s.}$ [87]. As another example, the combinatorics yield 6 $2p+2\alpha$ events for each decay event that passes through a ${}^{10}\text{C}$ intermediate state. Rather than deal with all these subevents, the invariant-mass spectrum in Fig. 5.3(d) shows only $2p+2\alpha$ subevents where one of the $p+2\alpha$ sub-subevents has an invariant-mass corresponding to a ${}^9\text{B}_{g.s.}$ decay. There is a prominent peak at $E_T=1.45$ MeV, corresponding to the sequential proton decay of the 5.18 MeV state of ${}^{10}\text{C}$ through ${}^9\text{B}_{g.s.}$ to ${}^8\text{Be}_{g.s.}$ [88].

There are also 6 ways to separate a detected event into two subgroups of $2p+\alpha$ events from which one can search for the fission of ${}^{12}\text{O}$ into two ${}^6\text{Be}$ fragments. When the decay energies of the prospective ${}^6\text{Be}$ fragments are plotted against each other, the plot shown in Fig. 5.3(a) is produced. A sharp peak can be seen in the lower left corner, corresponding to when the two ${}^6\text{Be}$ fragments are in their ground states ($E_T=1.37$ MeV). To examine this further, we use a diagonal gate shown by the dotted lines and projected onto either axis. The resulting projected spectrum is shown in Fig. 5.3(b). The g.s.+g.s. peak is clearly seen at $E_T=1.37$ MeV, and there is also a broad peak at ~ 3.5 MeV. This peak is above the expected energy if both ${}^6\text{Be}$ fragments are in the $E^*=1.16$ MeV, $J^\pi=2^+$ state. The origin of this large peak is unclear.

A multiplicity for each observed intermediate resonance and a probability for the ${}^6\text{Be}_{g.s.}+{}^6\text{Be}_{g.s.}$ can be determined by subtracting a smooth background under all the peaks Fig. 5.3. These multiplicities are shown plotted against E_T in Fig. 5.2(c). Multiplicities for the occurrence of a single ${}^6\text{Be}_{g.s.}$ and for the $J^\pi=5/2^-$, $E^*=2.345$ MeV state of ${}^9\text{B}$ were determined in addition

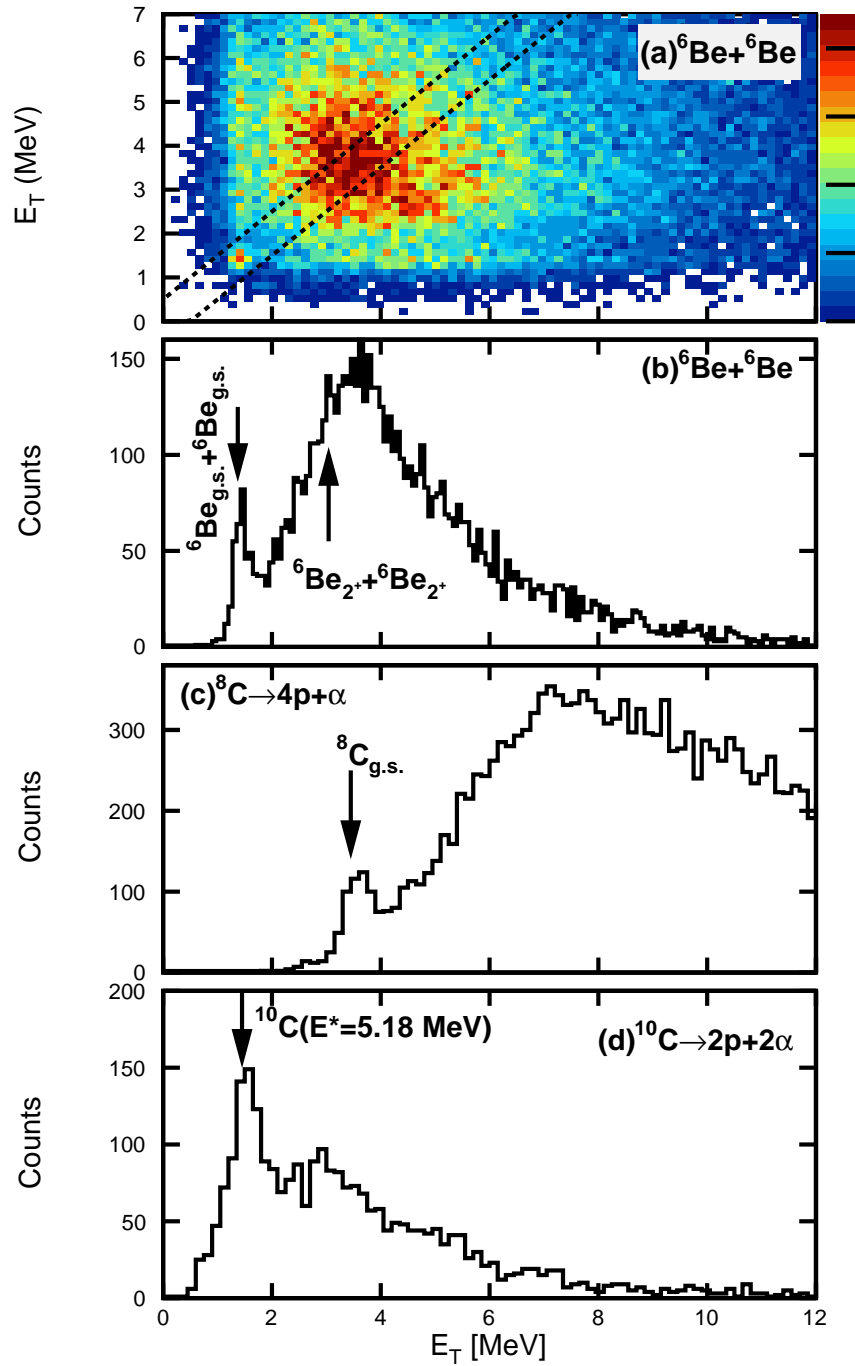


Figure 5.3: Invariant-mass spectra showing intermediate states present in the $4p+2\alpha$ channel. (a) shows the correlation of the E_T values of two ${}^6\text{Be}$'s that can be reconstructed from the six detected particles. If the diagonal gate indicated by the dotted lines is applied, the projection on either one of the axes is shown in (b). (c) and (d) show invariant-mass spectra for $4p+\alpha$ and $2p+2\alpha$ subevents. The arrows label the peaks associated with known levels. No $\cos\theta_C$ gate was employed.

to the previously discussed resonances. The multiplicities are inclusive, so, as an example, the ${}^8\text{Be}_{g.s.}$ yield from the decay of ${}^9\text{B}_{g.s.}$ is included in the ${}^8\text{Be}_{g.s.}$ multiplicity.

The E_T bin centered on the observed peak is marked by the fatter data points near 8 MeV. If the intermediate resonances are associated mainly with the ${}^{12}\text{O}$ peak and not with the background beneath it, the multiplicities should have a maximum at the E_T value for the peak (E_T^{peak}). This is clearly not the case. If the intermediate resonances come purely from the background, the multiplicities should have a minimum at E_T^{peak} . According to the fit in Fig. 5.2(a), the peak to background yield for the E_T bin centered on the peak is $\sim 1:1$. So we expect a suppression of 50% at the peak E_T relative to the trend from the other E_T bins. Again, this is also not the case. We can then conclude that all these intermediate resonances are found in the peak and background with similar magnitudes. It is not possible to make a more quantitative statement as the overall trend is non-linear. It is thus difficult to determine if the peak multiplicities are larger or smaller than the overall trend.

We conclude that $\sim 50\%$ of the events in the ${}^{12}\text{O}$ peak decay by producing at least one ${}^6\text{Be}_{g.s.}$ and another $\sim 20\%$ have a ${}^9\text{B}_{g.s.}$ fragment. The latter is responsible for most of the ${}^8\text{Be}_{g.s.}$ yield. The fision-like channels ${}^6\text{Be}_{g.s.} + {}^6\text{Be}_{g.s.}$ and $\alpha + {}^8\text{C}_{g.s.}$ are responsible for $\sim 9\%$ and $\sim 6\%$ of the yield respectively. The above analysis might miss wider intermediate states that are subsumed by the background.

5.3 Momentum Correlations

The momentum correlations in a $2p$ decay can be presented as a 2D distribution [2] and are usually given as energy (E_x/E_T) versus angle [$\cos \theta_k = \mathbf{p}_x \cdot \mathbf{p}_y / (p_x p_y)$] plot where these quantities are defined in the introduction. As a reminder, the quantity E_x in the Jacobi T representation is the relatively energy between the protons ($E_x = E_{pp}$), while in the Jacobi Y representation it is the relative energy between the core and one of the protons ($E_x = E_{p-core}$). In the Jacobi Y case, $\cos \theta_k \sim -1$ corresponds to a small relative angle

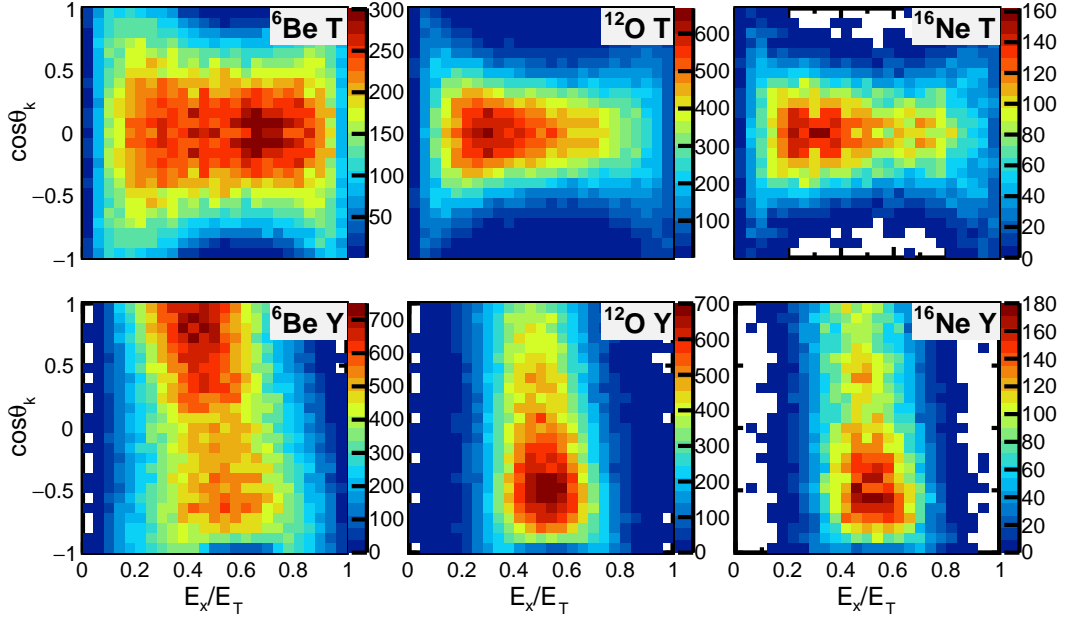


Figure 5.4: Experimental momentum correlation plots for the ground-state $2p$ decays of ${}^6\text{Be}$, ${}^{12}\text{O}$, and ${}^{16}\text{Ne}$. Results are shown in both the Jacobi T (upper panels) and Jacobi Y (lower panels) representations. The ${}^{12}\text{O}$ data is from this work while the ${}^6\text{Be}$ and ${}^{16}\text{Ne}$ data are from Refs. [10, 11].

between the momentum vectors of the two protons. Figure 5.4 shows a comparison between the Jacobi 2D plots for ${}^{12}\text{O}_{g.s.}$ and those obtained for ${}^6\text{Be}_{g.s.}$ [10] and ${}^{16}\text{Ne}_{g.s.}$ [11].

These data were obtained with the same detector setup and approximately the same beam E/A value, so the effect of the detector resolution and efficiency will be similar. All channels display features expected for $2p$ decay, most noticeably a suppression due to the Coulomb interaction when one of the protons and the core share a velocity vector (see $E_x/E_T \sim 0.56$, $\cos\theta_k = \pm 1$ in the Jacobi T representation) and when both protons share a velocity vector (see $E_x/E_T \sim 0.5$, $\cos\theta_k = -1$ in the Jacobi Y representation). It is apparent that the emitted protons have approximately the same energy, as the ridges in the Jacobi Y plots are centered near $E_x/E_T \sim 0.5$. This kinematic signature corresponds to a prompt $2p$ decay [22].

The results for ${}^{12}\text{O}$ are very similar to those for ${}^{16}\text{Ne}_{g.s.}$, and both differ in similar ways from the ${}^6\text{Be}$ results, having more yield for diproton-like decays (small E_x/E_T in the Jacobi

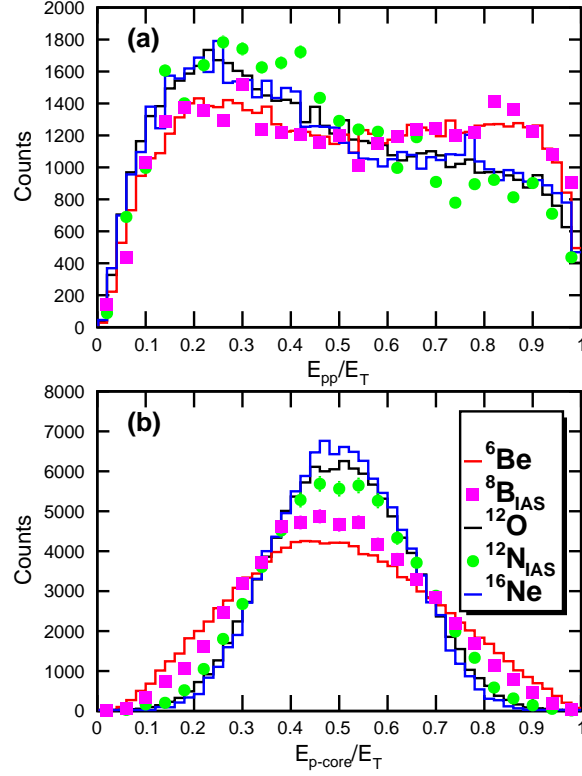


Figure 5.5: Projections of the (a) Jacobi T and (b) Jacobi Y 2D distributions on the energy axis. Ground-state $2p$ emitters are plotted as histograms while $2p$ emission from isobaric analogs is plotted as the data points.

T distributions and negative $\cos \theta_k$ values in the Jacobi Y distributions). A comparison of the correlations for these nuclei can be taken further by examining the projections of the 2D plots on their energy axis. These projections are shown as the histograms in Fig 5.5. The similarity of the $^{12}\text{O}_{g.s.}$ and $^{16}\text{Ne}_{g.s.}$ distributions are confirmed by these projections. These distributions confirm the predictions of the 3-body calculations of Grigorenko *et al.* [79].

Also included in Fig. 5.5 are projections for the $2p$ decays of $^{12}\text{N}_{IAS}$ (which will be further

Table 5.3: Decay energies for prompt $2p$ emitters in Fig. 5.5.

Nucleus	E_T [MeV]	Ref.
^6Be	1.372	[89]
$^8\text{B}_{IAS}$	1.313	[89]
$^{12}\text{O}_{g.s.}$	1.688(29)	this work
$^{12}\text{N}_{IAS}$	1.165(29)	this work
$^{16}\text{Ne}_{g.s.}$	1.466(20)	[11]

discussed in a later chapter) and ${}^8\text{B}_{IAS}$ [83]. The data can be divided into two groups that have similar projections: the lighter p -shell nuclei ${}^6\text{Be}_{g.s.}$ and ${}^8\text{B}_{IAS}$ and the heavier ${}^{12}\text{O}_{g.s.}$, ${}^{12}\text{N}_{IAS}$, and ${}^{16}\text{Ne}_{g.s.}$ systems. The decay energies for all systems are given in Table 5.3. The similarity of the heavy systems is expected, as all of them have significant $[s_{1/2}^2]_0$ contributions to their wavefunctions which dominates the $2p$ decay. ${}^6\text{Be}_{g.s.}$, however, is dominated by the $[p_{3/2}^2]_0$ component with some mixing with $[s_{1/2}^2]_0$ under the barrier, with the final distribution as a mixture of $[p_{3/2}^2]_0$ and $[s_{1/2}^2]_0$ components [90, 91].

Figure 5.6 shows the Jacobi Y momentum correlations for E_T bins centered on the three prominent peaks (0_1^+ , 2_1^+ , and 2_2^+) in the $2p+{}^{10}\text{C}$ invariant-mass spectra in Fig. 5.1(c). The 2_1^+ bin contains contributions from the shoulder state and the 2_2^+ bin contains a background contribution. Examination of the neighboring region to these peaks suggest these contributions have similar correlations. The correlations evolve from the prompt $2p$ decay for the ground state [Fig. 5.6(a)] to a sequential-like decay for the 2_2^+ state which displays two vertical ridges [Fig. 5.6(c)]. The latter decay is more complicated than the classical notion of sequential as we will see, but is it useful to determine which ${}^{11}\text{N}$ intermediate state these ridges are consistent with.

Figure 5.7 compares the experimental 2_2^+ correlations to simulations of sequential decay via the R -matrix formalism [92] through the $1/2^-$ [panel (c)] first-excited state and the $3/2^-$ [panel (d)] fourth-excited state of ${}^{11}\text{N}$. Both simulations produced ridges in similar locations to the experimental data. In these simulations, one ridge is vertical, corresponding to the second emitted proton whose relative energy with the core is independent of angle, and a sloping ridge, corresponding to the first emitted proton whose relative energy to the core depends of the recoil imparted by the second proton and thus dependent on $\cos\theta_k$. In the experimental data, the differentiation of the ridges into a vertical and sloping varieties is not obvious. It is possible that both ${}^{11}\text{N}$ intermediate states are involved and wash out this differentiation. For example, the correlations plot in Fig. 5.7(b) was obtained from incoherently adding the two decay paths with equal weight. If we have contribution from

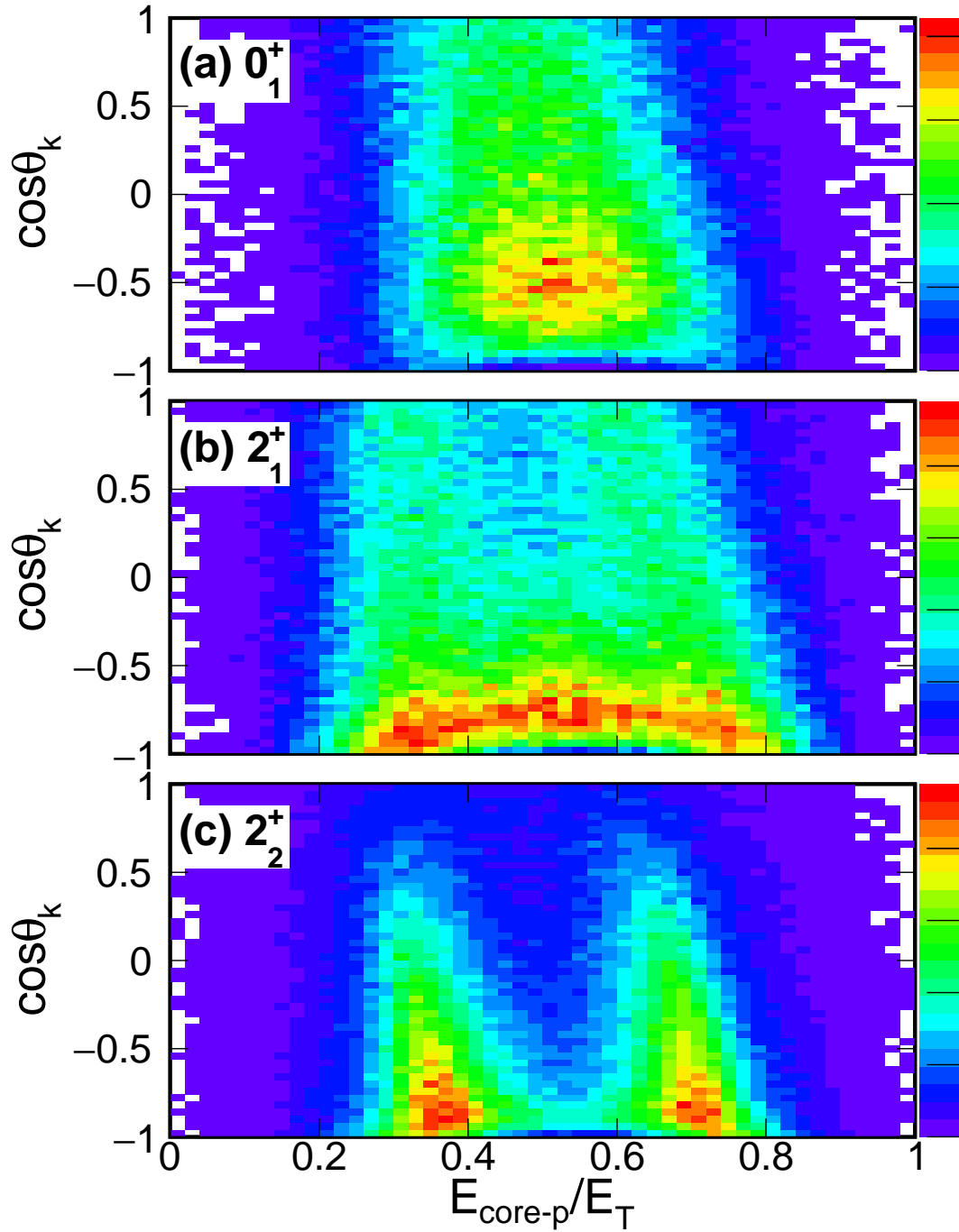


Figure 5.6: Jacobi Y momentum correlations for E_T bins centered on (a) 0_1^+ , (b) 2_1^+ , and (c) 2_2^+ states. The 2_1^+ results in (b) contained contributions from the shoulder state. The energy gates for the spectra are $1.43 < E_T < 2.02$ MeV for (a), $3.45 < E_T < 4.04$ MeV for (a), and $5.85 < E_T < 6.06$ MeV for (c).

the $3/2^-$ ^{11}N state, then it has a decay branch to the excited state of ^{10}C , producing yield in the shoulder state. This is discussed further in a later chapter.

While there is a sequential aspect to the 2_2^+ correlations in Fig. 5.6(c), the yield of the ridges decreases rapidly as $\cos \theta_k \rightarrow 1$. One expects a symmetric distribution about $\cos \theta_k = 0$ if there is no memory between the two decay steps, even if there is interference between the two decay paths as the two intermediate states have the same parity. Figure 5.8 shows the projection of the Jacobi Y distribution, corrected for the detection efficiency, as the square data points. The data are selected with a narrow, 1.4-MeV wide gate at the peak of the 2_2^+ state in an effort to reduce the background contribution. To estimate the remaining background, a gate was placed lower in energy, between the two 2^+ states (the triangular data points), and higher in energy, above the 2_2^+ state (open circular data points). The background distributions are scaled to give the total background contribution as is seen in the fits.

The data show a strong $\cos \theta_k$ dependence, with a maximum occurring close to where the relative angle between the two protons is $\theta_{pp} = 0$. The background distributions have significantly less θ_{pp} dependence, and thus is unable to explain all the θ_{pp} dependence seen in the peak region. It is clear that the decay path deviates from the notion of independent sequential decays in which the second decay has no memory of the first (apart from that dictated by angular-momentum conservation). A similar observation was found for the $2p$ decay of the 2_1^+ state in ^{16}Ne [93], where the preference for small relative angles between the protons was explained in the 3-body model as an interference between sequential and prompt decay components. The sequential decay of the ^{17}Ne second excited state also shows a preference for small θ_{pp} after the proton-proton final state interaction was considered, but the magnitude was much smaller than observed here [94]. In the ^{17}Ne case, the ^{16}F intermediate state had a much smaller decay width ($\Gamma \sim 20$ keV) than the two possible ^{11}N intermediate states we determined for the decay of the 2_2^+ state. This suggests that this memory effect diminishes as the time between the two sequential decays increases.

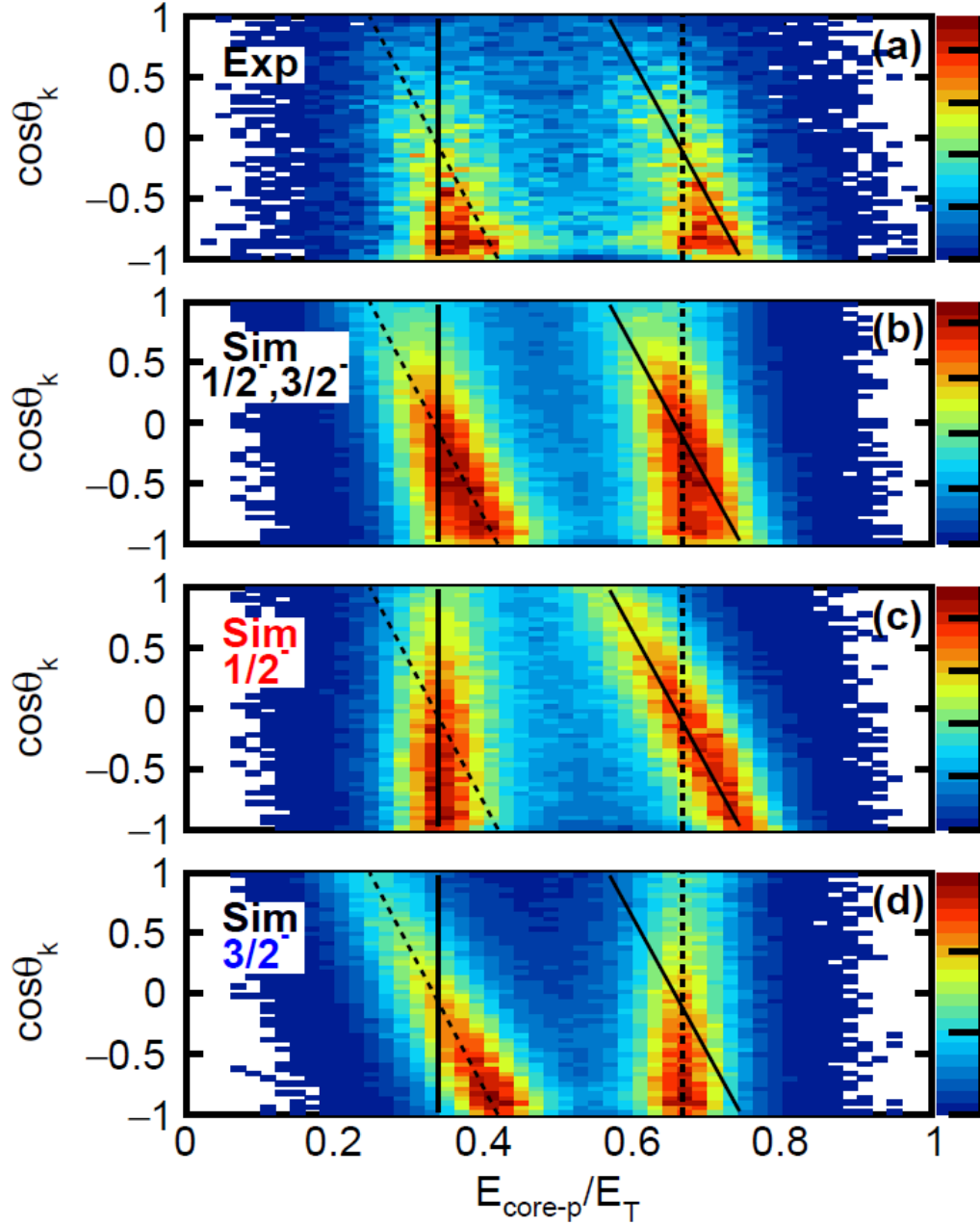


Figure 5.7: (a) Experimental 2D momentum correlations of the 2_2^+ state of ^{12}O , and simulated momentum correlations of sequential decay through (b) a combination of the $\frac{1}{2}^-$ and $\frac{3}{2}^-$ second and fifth excited states of ^{11}N , (c) the $\frac{1}{2}^-$ states alone, and (d) the $\frac{3}{2}^-$ state alone. The dashed lines show the expected ridgelines when decaying through the $3/2^-$ state, while the solid lines indicate the ridgelines expected when decaying through the $1/2^+$ state.

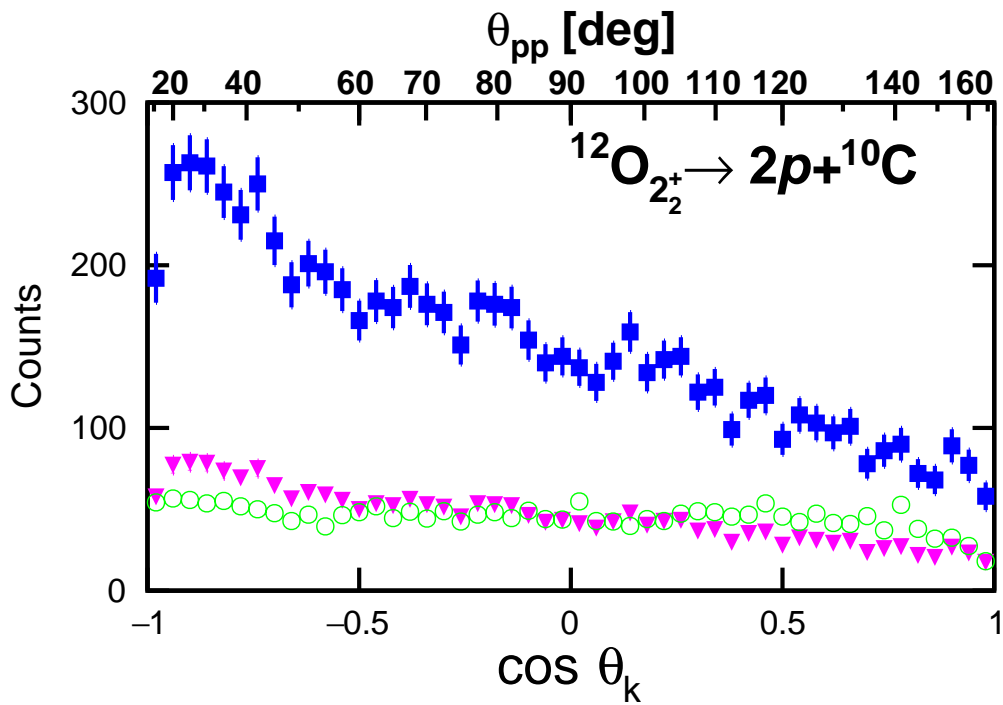


Figure 5.8: Efficiency-corrected projection of the Jacobi Y correlation plot for the 2_2^+ ^{12}O state on the $\cos \theta_k$ axis. Results are shown for (square data points) for a tight gate on the invariant-mass peak and for background gates on either side of this peak (triangles and open circles). An axis showing the relative angle θ_{pp} between the protons is also included.

Table 5.4: Structure of the the first third 2^+ states predicted with the Gamow coupled-channel approach [19]

2_1^+ , $E_T=3.803$ MeV, $\Gamma=0.132$ MeV		
65%		$(s_{1/2}, d_{5/2})$
23%		$(d_{5/2}, d_{5/2})$
11%		$(s_{1/2}, s_{1/2})$
2_2^+ , $E_T=5.150$ MeV, $\Gamma=1.027$ MeV		
94%		$(p_{1/2}, p_{3/2})$
1%		$(p_{1/2}, p_{1/2})$
2_3^+ , $E_T=6.235$ MeV, $\Gamma=1.982$ MeV		
55%		$(s_{1/2}, d_{3/2})$
29%		$(s_{1/2}, d_{5/2})$
4%		$(p_{3/2}, p_{1/2})$
2%		$(d_{5/2}, d_{5/2})$
2%		$(p_{3/2}, p_{3/2})$
2%		$(S_{1/2}, s_{1/2})$

5.4 Comparison to GCC predictions

The structure of ^{12}O states have recently been predicted with the Gamow coupled-channel approach [19], which treats the nucleus as a two protons interacting with a deformed ^{10}C core. The wave function of the protons is expanded using the Berggren basis, which includes bound and scattering states, thus considering the effects of the continuum. An initial comparison with the experiment levels of ^{12}O was made in [19] and the predicted ground-state width was found to be similar to the experimental value. It is interesting to see if the sequential-decay components of the observed 2^+ states are consistent with the predicted internal structure. The wavefunction components predicted for the three 2^+ states are listed in Table 5.4.

The 2_1^+ state has a sequential component which decays through the $J^\pi=1/2^+$ ground state of ^{11}N , consistent with the sequential removal of a d and then an s wave proton. This matches well with the largest component of the predicted wavefunction for this state in Table 5.4. This component and the next largest component $(d_{5/2}, d_{5/2})$ could also produce a sequential decay contribution through the $5/2^+$ state in ^{11}N (See Fig. 6.1), but as the decay energy of the first proton would be small, the barrier penetration fraction appears to have

suppressed it.

Our second observed 2^+ state at $E_T=6.5$ MeV is similar in energy to both the GCC predictions for the second and third 2^+ state. The two proposed sequential components deduced from the correlation plot both involve the emission of two p -wave protons and thus suggest that our observed 2_2^+ level is also the second 2^+ state in the calculations which is dominated by a $(p_{1/2}, p_{3/2})$ structure. Indeed the two sequential decay paths can then be interpreted as differing in the order in which the $p_{1/2}$ and $p_{3/2}$ proton are emitted.

Chapter 6

$^{11,12}\text{N}$

6.1 Introduction

The structure of $^{11,12}\text{N}$ is an interesting question to consider along with the structure of $^{11,12}\text{O}$. The sequentially decaying states of ^{12}O decay through intermediate states in ^{11}N , which makes understanding the energies and widths of ^{11}N a relevant and important question. The decay energy and width of the proton decaying ^{11}N ground state are not well defined. It is important to further investigate this state, as it is clear from the 2D momentum correlations for the first 2^+ state in ^{12}O that there is a sequential decay path through the ^{11}N ground state.

The isobaric analog state (IAS) of ^{12}O has been seen in ^{12}N [53]. The analog in ^{12}N undergoes prompt $2p$ decay to the isobaric analog of ^{10}C in ^{10}B . This was the second observed case of direct $2p$ decay from an IAS to another IAS, the first case being $^8\text{B}_{IAS} \rightarrow 2p + ^6\text{Li}_{IAS}$ [82, 83]. It is interesting to consider higher-lying analog states in ^{12}N and to investigate to which states in ^{10}B they decay.

The decay scheme shown in Fig. 6.1 shows the levels of interest in $^{11,12}\text{N}$. The scheme also shows the sequential and direct decay paths of the $2p$ decaying states in ^{12}O .

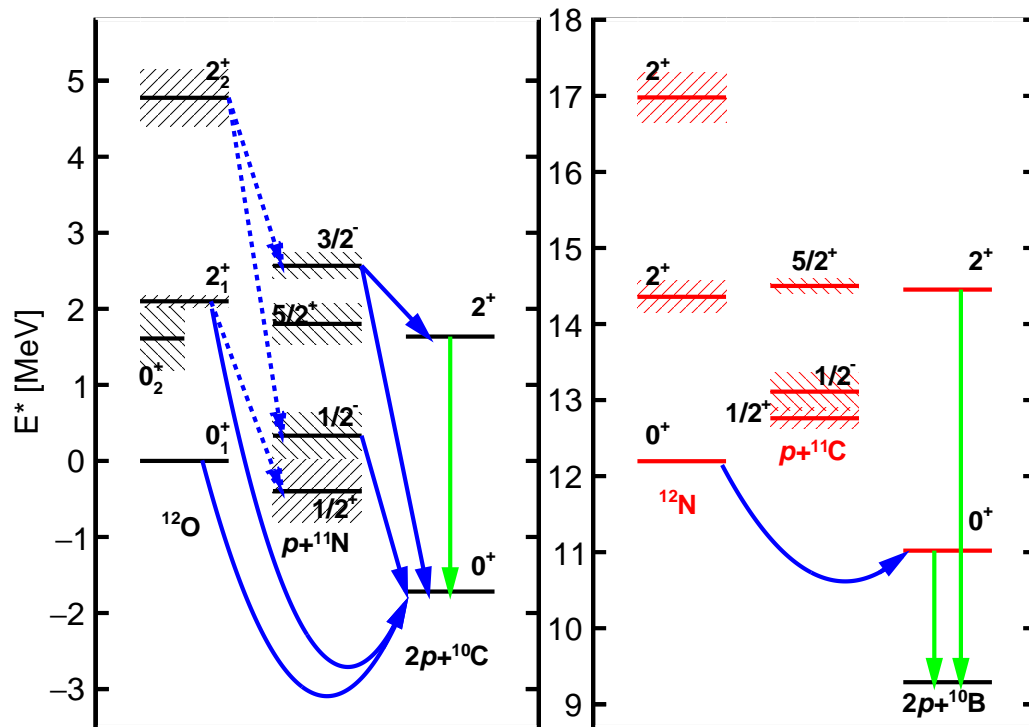


Figure 6.1: Levels of interest in the $1p$ decay of ^{11}N states, $2p$ decay of ^{12}O states, and their analogs in ^{12}N . Green arrows show γ -ray decays of importance, while observed $1p$ decays are shown as the straight blue arrows. The dashed curves show possible sequential decay paths of ^{12}O states investigated in this work. The curved blue arrows indicate direct $2p$ decay. The 0_2^+ ^{12}O state from [12] is also shown.

6.2 ^{11}N Structure

6.2.1 $p+^{10}\text{C}$ spectrum

The E_T spectrum from detected $p+^{10}\text{C}$ events is shown as the black histogram in Fig. 6.2(a). From this spectrum we have subtracted two types of contaminations. First, a fraction of ^{11}C fragments leak into the ^{10}C gate. To estimate the spectrum from such events, we have taken the detected $p+^{11}\text{C}$ events and analyzed them as if the ^{11}C fragment was ^{10}C . This spectrum is scaled by the probability of misidentification determined from the calibration beams to give the red histogram in Fig 6.2(a). Its magnitude is only significant at very small values of E_T . Secondly, $^{12}\text{O}\rightarrow 2p+^{10}\text{C}$ events in which one of the protons was not detected will also contribute to the detected $p+^{10}\text{C}$ events. To account for this, we have taken the detected $2p+^{10}\text{C}$ events and randomly thrown away one of the protons, scaling the subsequent $p+^{10}\text{C}$ invariant-mass spectra (blue histogram) based on the results of the Monte-Carlo simulation to appropriately represent the number of contaminated events from this process.

The contamination-subtracted spectrum is shown as the data points in Fig. 6.2(b). The labeled black arrows show the locations of levels listed in the ENSDF database. A strong peak for the $J^\pi=1/2^-$ first-excited state is observed, as is a smaller peak for the $J^\pi=3/2^-$ state. The $1/2^+$ (ground state) and $5/2^+$ levels, if present, are not resolved. The unlabeled red arrows show the locations of new peaks necessary to fit the spectrum. The dominant $1/2^-$ peak has a high-energy tail which cannot be explained by its expected line shape. In fitting the spectrum, we have assumed a new level just above the $1/2^-$ peak in order to reproduce the observed shape. More remarkable is the presence of a low-energy peak ($E_T \sim 1.1$ MeV) well below the nominal ground-state energy of $E_T=1.49$ MeV. It is unlikely that this is a true $p+^{10}\text{C}_{g.s.}$ resonance, as we would expect it to have been observed already. Rather the more reasonable explanation is that it represents a p decay to the $J^\pi=2^+$ first-excited state of ^{10}C which gamma decays ($E_\gamma=3.354$ MeV, see Fig. 6.1). Adding the γ energy moves this peak to the same energy as the $3/2^-$ level. Thus we conclude the $J^\pi=3/2^-$ level has proton

Table 6.1: Level parameters obtained from the fit to the $p+^{10}\text{C}$ invariant-mass spectrum of Fig. 6.2(b).

J_π	ENSDF		This Work		
	E_T [MeV]	Γ [keV]	E_T [MeV]	Γ [keV]	E^* [MeV]
$1/2_1^+$ $1/2_1^-$	2.220(30)	600(100)	2.216(5)	721(13)	0.726
?			2.563(10)	697(32)	1.073 or 4.416
$5/2^+$	3690(30)	540(40)			2.200
$3/2^-$	4.350(3)	340(40)	4.475(5)	340	3.986

decay branches to both the ground and first excited state of ^{10}C .

The solid curve in Fig. 6.2(b) shows a fit to the invariant-mass spectrum with 5 levels (6 peaks), including the known states indicated by the black arrows and one new level. R -matrix line shapes are used for all levels except for the new states where a simple Breit-Wigner shape is assumed, as the decay orbital angular momentum is unknown. The energies and widths of the unresolved $1/2^+$ and $5/2^+$ states were fixed to the ENSDF values, but their presence allows for a good fit with a smooth background (blue dashed curve). The fitted branching ratio of the $3/2^-$ state is $\Gamma_{p_0}/(\Gamma_{p_0} + \Gamma_{p_1}) = 0.64(6)$. Fitted energies and widths are listed in Table 6.1.

6.2.2 ^{11}N ground state

The correlations in Fig. 5.6(b) for the 2_1^+ state of ^{12}O are dominated by a banana-shaped structure in the diproton region ($\cos\theta_k < -0.5$). A look at the upper half of the correlation plot reveals the presence of two clear ridges suggesting a sequential-like decay component. As mentioned before, the sloping ridge corresponds to the emission of the first proton. The sloping ridge is the one on the right in Fig. 5.6(b), so this proton has more energy than the second one. As the decay scheme in Fig. 6.1 shows, the only level that the 2_1^+ state can decay through to give the correct energy ordering is the $1/2^+$ ground state of ^{11}N . These ridges are further investigated by the energy-projection of the relative energy between the emitted protons and the core, $E_{\text{core}-p}$, for $\cos\theta_k > 0.5$, plotted as the data points in Fig. 6.3.

The resonance energy and width of $^{11}\text{N}_{g.s.}$ is not well-defined as seen by the discrepancy

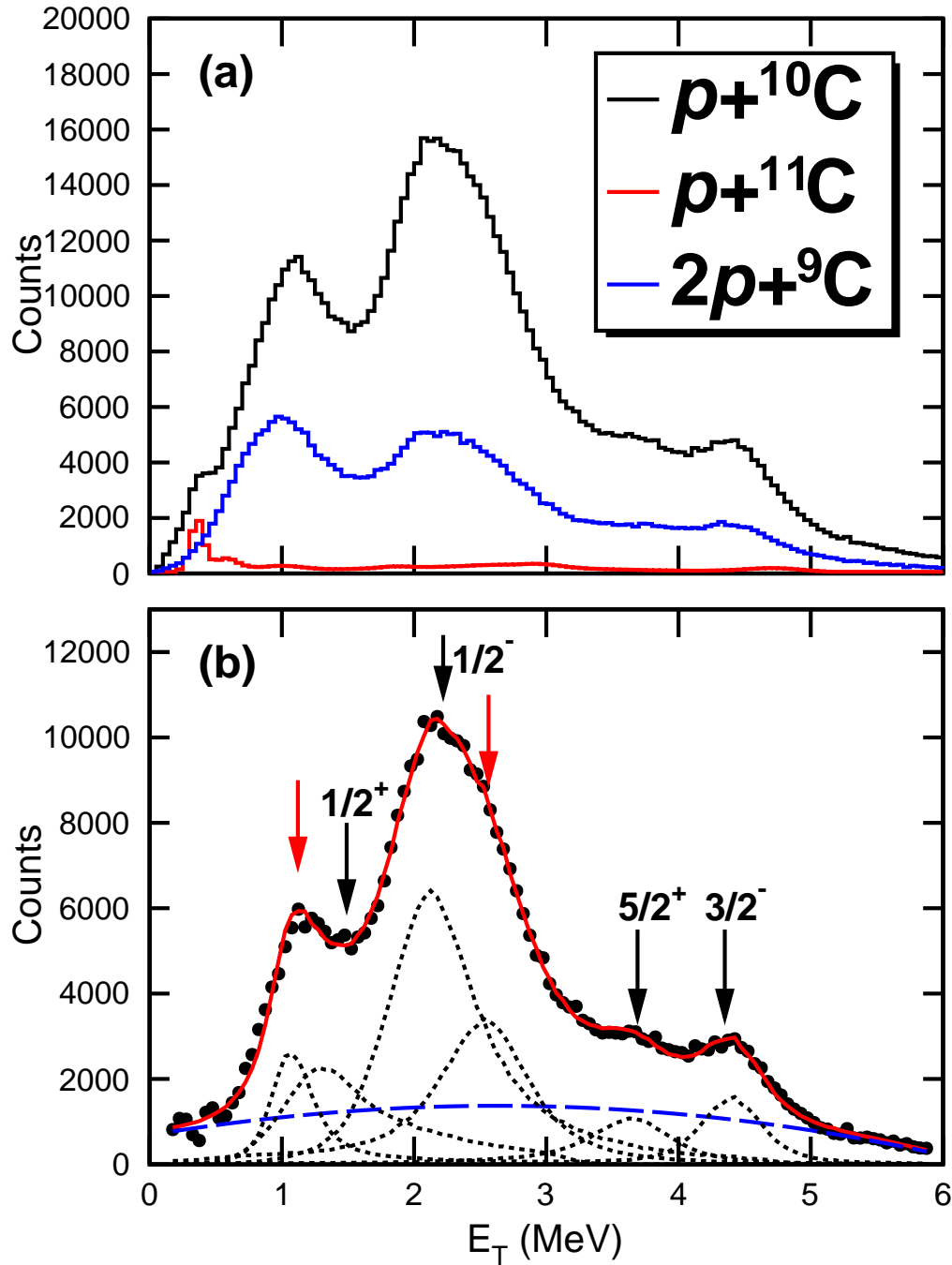


Figure 6.2: $p+^{10}\text{C}$ invariant-mass spectra. (a) The raw spectrum is shown by the black histogram. The red and blue histograms show estimates of the contamination from $p+^{11}\text{C}$ events where the ^{11}C fragment was misidentified as a ^{10}C and from $^{12}\text{O}\rightarrow 2p+^{10}\text{C}$ events where one of the protons was not detected. (b) Fit to the contamination-subtracted spectrum with known ^{11}N peaks in ENSDF indicated by the labeled black arrows and new peaks by the unlabeled red arrows. The fitted peaks for individual levels are shown as the dotted black curves, while the blue dashed curve is the fitted background. A $|\cos\theta_C| < 0.5$ gate was applied for all spectra.

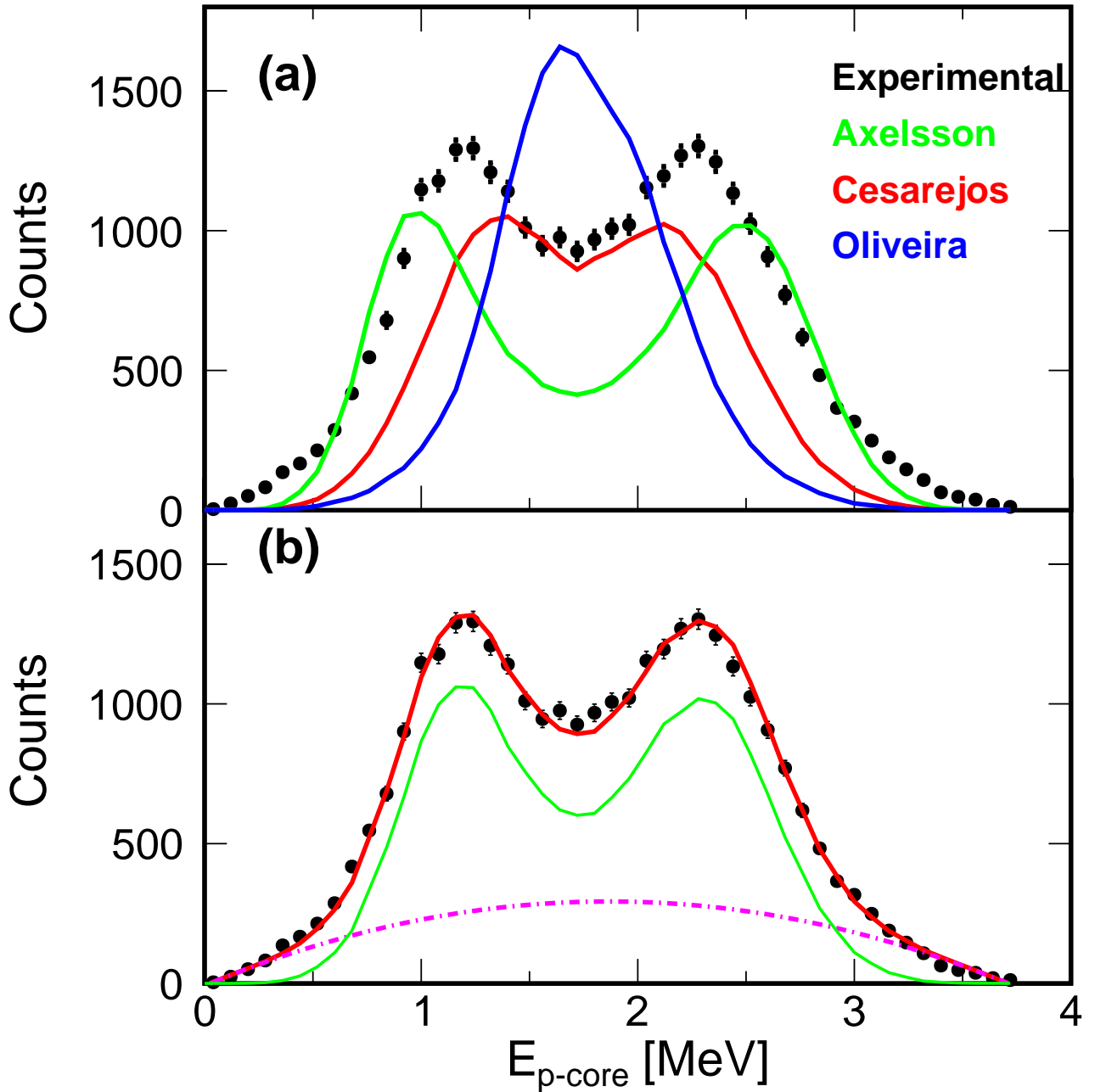


Figure 6.3: Jacobi projections of experimental (black dots) and simulated (solid curves) of sequential decays through $^{11}\text{N}_{g.s.}$ where $\cos\theta_k > 0.5$. The different colored curves in (a) correspond to the different literature parameters given in Table 6.2. The red solid curve in (b) corresponds to a new fit to the data. The parameters for this new fit are also given in Table 6.2. The pink dashed curve corresponds to the fitted background, and the solid green curve corresponds to the total fit after subtraction of the background.

Table 6.2: Decay energies and widths reported in the literature and in this work for the proton-decaying $1/2^+$ ground state of ^{11}N .

E_T [MeV]	Γ [MeV]	Authors	Ref.
1.30(4)	0.99^{+100}_{-200}	Axelsson, et al.	[95]
1.54(2)	0.83(3)	Casarejos, et al.	[97]
1.63(5)	0.4(1)	Oliveira, et al.	[96]
1.378(5)	0.779(12)	This work	

of level parameters from three studies [95, 96, 97] given in Table 6.2. By examining the sequential-component, it might be possible to clear up some of the confusion about the decay parameters of this state. The curves plotted in Fig. 6.3(a) show sequential predictions obtained with the three different parameter sets in Table 6.2. The experimental data does not appear to agree with a decay through the $^{11}\text{N}_{g.s}$ as described by [96]. It is also difficult to claim agreement with either [95] or [97], as the experimental peaks appear to lie directly between the two curves. Our data would suggest an intermediate resonance energy to those from [95, 97]. We provide our own fit to the data in Fig. 6.3(b). From the best fit to the data, we report a decay energy of 1.378(5) MeV and a width of 0.779(12) MeV for the proton-decaying ground state of ^{11}N .

6.3 ^{12}N structure

6.3.1 $2p+^{10}\text{B}$ channel

Known low-lying ^{12}N states were observed in the $p+^{11}\text{C}$ spectrum in Fig. 5.1(b). Higher-lying excited states can be found in the $2p+^{10}\text{B}$ spectrum in Fig. 6.4(b). This spectrum bears a strong resemblance to the $2p+^{10}\text{C}$ spectrum from ^{12}O decay which is also reproduced in panel (a) for convenience. Both spectra contain three prominent peaks with the same energy spacing between them. In addition, the second of these peaks in both cases has a low-energy shoulder. This surprising result suggests that all the peaks in the $2p+^{10}\text{B}$ spectrum are analogs of the observed ^{12}O levels. Indeed, the lowest-energy peak was also observed in the

Table 6.3: Fitted parameters for ^{12}N states observed in the $2p+^{10}\text{B}$ invariant-mass spectrum of Fig. 6.4(b), the $2p+\alpha+^6\text{Li}$ spectra in Figs. 6.5(c) and 6.5(d), and the $3p+^9\text{Be}$ spectrum in Fig. 6.6.

Observed Channel	Intermediate Channel	J^π	$E_{n\gamma}^* [\text{MeV}]$	$E^* [\text{MeV}]$	$\Gamma [\text{keV}]$	$\sigma \text{ (mb)}$
$2p+^{10}\text{B}$		0^+	10.502(4)	12.242 (4)	<100	0.164(6)
$2p+^{10}\text{B}$		2^+	12.574(4)	14.314 (4)	193(26)	1.04(2)
$2p+^{10}\text{B}$		2^+	15.252(11)	16.992(11)	420(120)	1.85(6)
$2p+\alpha+^6\text{Li}$	$\alpha+^8\text{B}_{IAS}$		18.408(66)	21.970(66)	649(49)	0.0635(4)
$2p+\alpha+^6\text{Li}$	$^6\text{Be}_{g.s.}+^6\text{Li}_{IAS}$		18.569(86)	22.131(86)	702(170)	0.1075(72)
$3p+^9\text{Be}$			22.158(23)	22.258(23)	138(79)	2.05(20)

invariant-mass study of Jager *et al.* [53] and it was argued that it was produced by the prompt $2p$ decay of the Isobaric Analog State (IAS) of ^{12}O in ^{11}N to the IAS in ^{10}B . The latter subsequently γ decays. This represented a second example of prompt $2p$ decay from one IAS to another [98]. The other example is the IAS of ^8C in ^8B which $2p$ decays to the IAS state in ^6Li where the γ ray from the decay of $^6\text{Li}_{IAS}$ was observed [83]. In both cases, prompt $2p$ decay was the only particle-decay mode which conserved both energy and isospin.

If these other states are also analog states ($T=2$), then the two higher-energy states are both $J^\pi=2^+$ and also involve $2p$ decay to the IAS of ^{10}B . The low-energy shoulder on the lowest 2^+ peak can again have contributions from three possible sources, i.e. from $T=2$, $J^\pi=0^+$ or 1^- levels or from a decay branch of a higher-energy 2^+ state which decays to the first $T=1$, $J^\pi=2^+$ state in ^{10}B (Fig. 6.1). The red solid curve in Fig. 6.4(b) shows a fit obtained with Breit-Wigner intrinsic line shapes and where the third origin of the low-energy shoulder is assumed. Figure 6.4(a) shows a similar fit to the $2p+^{10}\text{C}$ decay channel of ^{12}O , assuming a decay through the excited state of ^{10}C . The known energy of the first $T=1$, $J^\pi=2^+$ ^{10}B state is used to constrain its $E_{n\gamma}^*$ centroid relative to the fitted value for the second 2^+ state. The fitted branching ratio is 0.087(12) which is smaller than the corresponding number obtained for the $^{12}\text{O}\rightarrow 2p+^{10}\text{C}$ shoulder state.

Although the $2p+^{10}\text{B}$ and $2p+^{10}\text{C}$ spectra in Fig. 6.4 have similar structure, the obvious difference is the much smaller relative yield for the $^{12}\text{N}_{IAS}$ peak ($E_{n\gamma}^*=10.502$) compared to

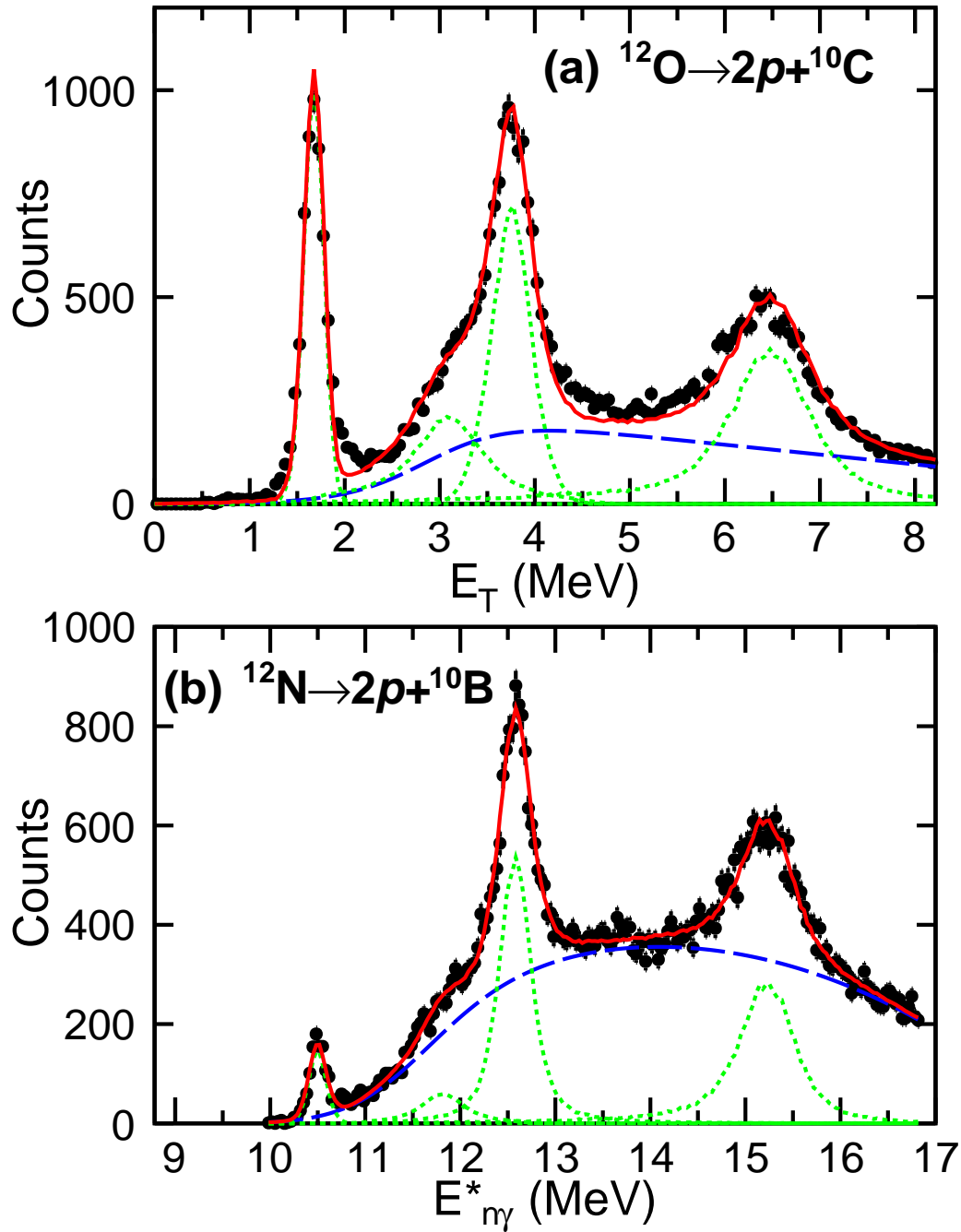


Figure 6.4: Comparison of invariant-mass spectra for the (a) $2p+^{10}\text{C}$ and (b) $2p+^{10}\text{B}$ exit channels. Fits using Breit-Wigner intrinsic line shapes are shown by the curves in both panels. A $|\cos\theta_C| < 0.2$ gate was applied for both spectra.

that for the other peaks. The cross sections for the 2_1^+ and 2_2^+ states have similar magnitudes for both the $^{12}\text{O}\rightarrow 2p+^{10}\text{C}$ and $^{12}\text{N}\rightarrow 2p+^{10}\text{B}$ spectra (compare values in Tables 5.2 and 6.3), with the ^{12}N values 15-20% lower in magnitude even if the shoulder yield is added to the contribution from the main 2_2^+ peak. Compared to this, the 0^+ ^{12}N state is reduced in magnitude by a factor of 4.4 relative to its ^{12}O analog.

The simplest explanation would be that $^{12}\text{N}_{IAS}$ has one or more other decay branches which account for most of the decay leaving the $2p$ branch with only $\sim 30\%$ of the yield. If these other branches involve particle emission, then they must violate isospin symmetry, but no candidate peaks were observed in other ^{11}N exit-channels. We cannot rule-out other particle-decay branches as some of these will have very low detection efficiency, e.g., single-proton decay to the $^{11}\text{C}_{g.s.}$ where the emitted proton will mostly travel to angles outside the detectors angular acceptance. Another possibility is that the $^{12}\text{N}_{IAS}$ has a significant M1 γ decay strength to the ground state which would satisfy the spin and isospin selection rules.

6.3.2 $2p+\alpha+^6\text{Li}$ channel

While the analogs of the low-lying ^{12}O levels have been found, we have also searched for the analog of the higher-lying ^{12}O level observed in the $4p+2\alpha$ channel. Given the large number of decay paths inferred for this state, it is reasonable to assume multiple exit-channels associated with the analog state, some of which would contain unbound neutrons. The analog of the fission-like $^6\text{Be}_{g.s.}+^6\text{Be}_{g.s}$ and $\alpha+^8\text{C}_{g.s.}$ channels in ^{12}O would be $^6\text{Be}_{g.s.}+^6\text{Li}_{IAS}$ and $\alpha+^8\text{B}_{IAS}$ which would populate the $2p+\alpha+^6\text{Li}+\gamma$ exit channel. No peaks are observed in the raw $2p+\alpha+^6\text{Li}$ invariant-mass spectrum, but with suitable gating the analogs can be found. The $2p+\alpha$ and $2p+^6\text{Li}$ subevents are shown in Fig. 6.5(a) and 6.5(b), respectively.

The peak observed in the $2p+^6\text{Li}$ exit channel [Fig. 6.5(b)] is consistent in energy and width to a peak observed following proton knockout from a ^9C beam. It was identified as a $^8\text{B}_{IAS}\rightarrow 2p+^6\text{Li}_{IAS}$ decay where the γ ray from the decay of $^6\text{Li}_{IAS}$ was observed in a subsequent experiment. Gating on the $^8\text{B}_{IAS}$ peak produces the $2p+\alpha+^6\text{Li}$ invariant-mass

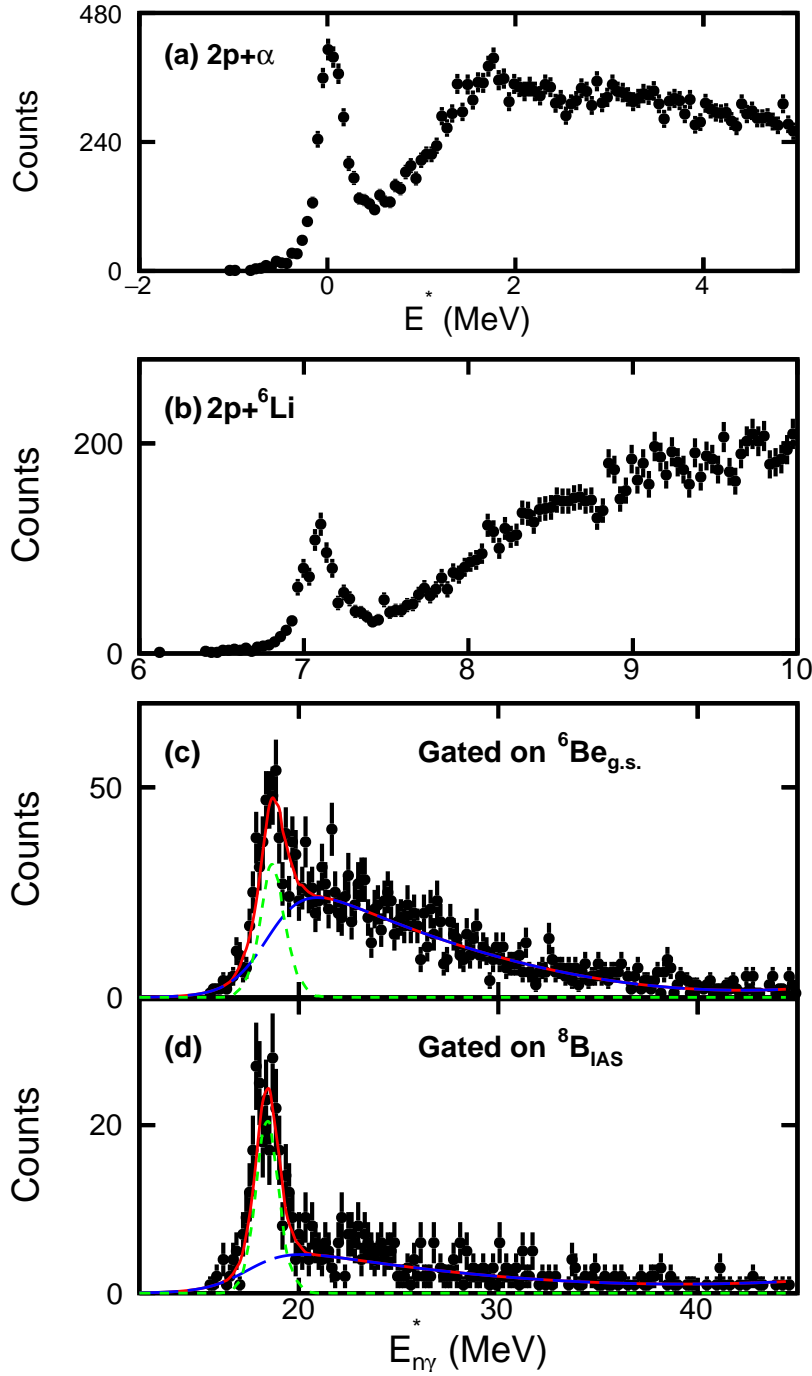


Figure 6.5: The upper panels show (a) $2p+\alpha$ and (b) $2p+{}^6\text{Li}$ invariant-mass spectra for these subevents. No $\cos\theta_C$ gate was applied. (c,d) show invariant-mass spectra obtained from the $2p+\alpha+{}^6\text{Li}$ events gated on the ${}^6\text{Be}_{g.s.}$ and ${}^8\text{B}_{IAS}$ invariant-mass peaks in (a) and (b), respectively. The curves in (c,d) are fits assuming a single Breit-Wigner lineshape.

spectrum in Fig. 6.5(d). Taking into account the energy of the unobserved gamma ray (3.563 MeV), the excitation energy of the $^{12}\text{N} \rightarrow \alpha + ^8\text{B}_{IAS}$ state is at 21.970(66) MeV.

A ^6Be ground-state peak is observed in the invariant-mass spectrum for the $2p + \alpha$ subevents [Fig. 6.5(a)]. Gating on this peak produces the invariant-mass spectrum in Fig. 6.5(c). In principle this peak could correspond to either a $^6\text{Be} + ^6\text{Li}_{g.s.}$ or $^6\text{Be}_{g.s.} + ^6\text{Li}_{IAS}$ decay. However, the fitted $E_{n\gamma}^*$ values and widths of the peaks in Figs. 6.5(c) and 6.5(d) (given in Table 6.3) are consistent, suggesting that they are decay branches of the same state. Thus the peak in Fig. 6.5(c) corresponds to the fission-like $^6\text{Be}_{g.s.} + ^6\text{Li}_{IAS}$ decay.

6.3.3 $3p + ^9\text{Be}$ channel

As the $^{12}\text{O} \rightarrow 4p + 2\alpha$ peak appears to have a significant probability of decaying to $^9\text{B}_{g.s.}$ intermediate states, its analog in ^{12}N could decay to the $3p + ^9\text{Be}$ exit channel. The invariant-mass spectrum for these events is shown in Fig. 6.6(b) and displays a well resolved peak at an excitation energy consistent with that inferred for the $^{12}\text{N} \rightarrow 2p + \alpha + ^6\text{Li}$ peaks. See Table 6.3 for comparison of peak parameters from Breit-Wigner fits. However the fitted intrinsic width of this state is considerably smaller than the ($T=2$) $2p + \alpha + ^6\text{Li}$ peaks, indicating that it must be associated with a different ^{12}N level. It may even be a $T=1$ state. However we suspect it is a $T=2$ state, implying that the observed peak in the analog spectrum, $^{12}\text{O} \rightarrow 4p + 2\alpha$, is a multiplet.

Further information on the decay of this state can be gleaned from the invariant-mass spectrum of the $p + ^9\text{Be}$ subevents in Fig. 6.6(c). A prominent peak at $E^* \sim 7.47$ MeV is observed which could be one or both of the $E^*=7.470$ -MeV ($J^\pi=2^+$, $T=0$) and $E^*=7.479$ -MeV ($J^\pi=2^-$, $T=1$) excited states of ^{10}B . The multiplicity of this peak is plotted as a function of ^{12}N excitation energy in Fig. 6.6(a). The smooth green dashed curve was fitted to excitation-energy bins beyond the peak region and suggests that there might be a small enhancement of this intermediate state at the peak energy. However, this curve is not well constrained for energies below the peak value. Nevertheless, it is clear that this intermediate-

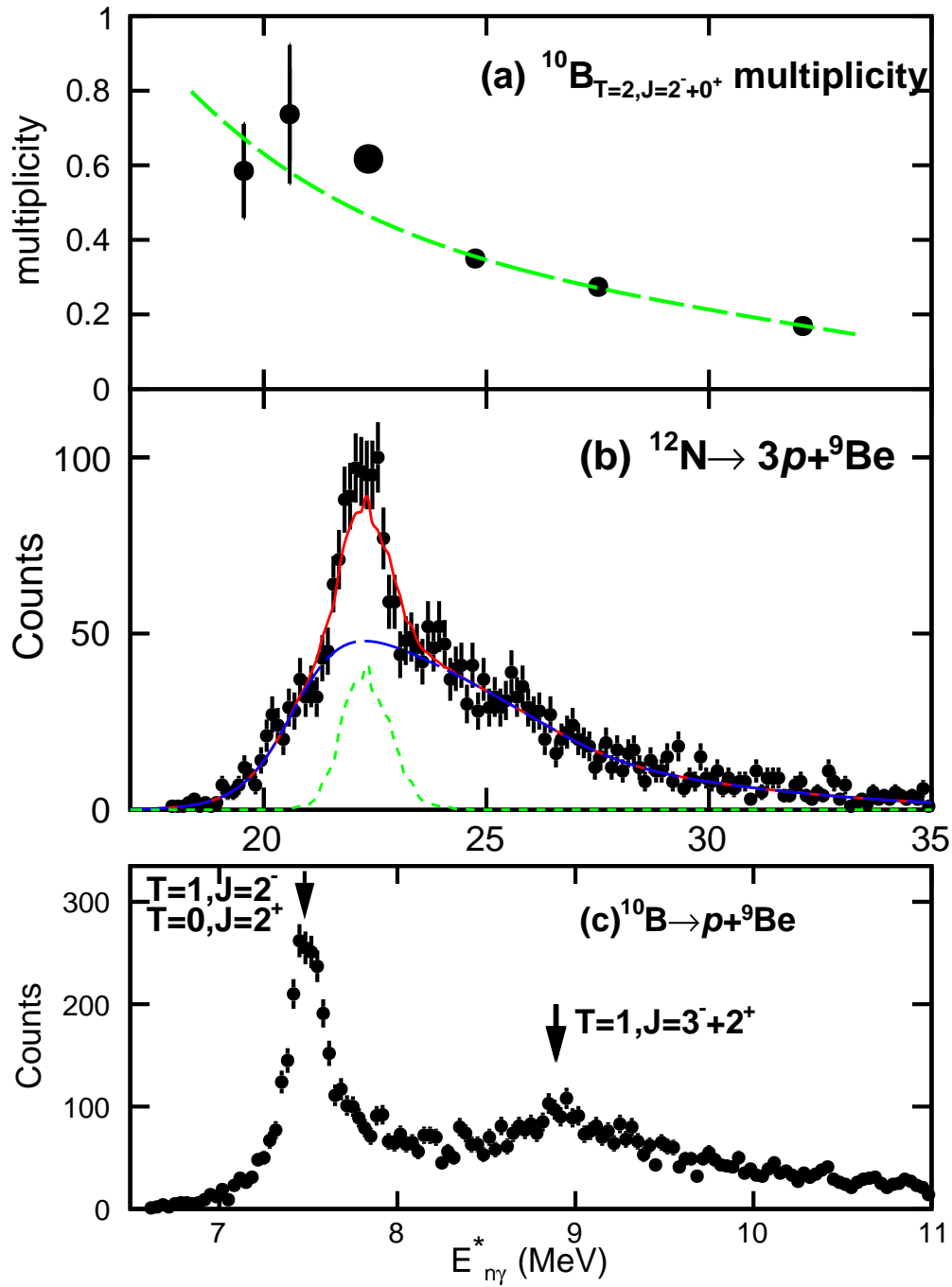


Figure 6.6: (a) The multiplicity of the low-energy peak in (c) as a function of excitation energy. The dashed blue curve is a smooth fit to the data points beyond the observed ^{12}N peak in (b), the experimental $3p+^9\text{Be}$ invariant-mass spectrum with a fit assuming a single Breit-Wigner level and smooth background (blue dashed curve). (c) Invariant-mass spectrum obtained from the $p+^9\text{Be}$ subevents. The energies of known ^{10}B levels are indicated. A $|\cos\theta_C| < 0.5$ gate was applied to both spectra.

state peak is associated with a significant fraction of the $^{12}\text{N} \rightarrow 3p + ^9\text{Be}$ peak yield. If the ^{12}N state is $T=2$ as suspected, then the intermediate state must be the $T=1$, $J^\pi=2^-$ state. We also see a suggestion of some smaller yield for the $T=1$, $J^\pi=3^-$ ($E^*=8.887$ MeV) and 2^+ ($E^*=8.895$ MeV) ^{10}B states in the $p + ^9\text{Be}$ spectrum in Fig. 6.6(c), but it is difficult to extract multiplicities as the relative magnitude of the background is much larger.

6.4 Analog States

To further explore the analog states in ^{12}O and ^{12}N we have looked at their consistency with the other $A=12$ quintet states. Figure 6.7 plots the levels scheme of the newly found levels relative to the energy of the lowest $T=2$, $J^\pi=0^+$ state. In addition, $T=2$ levels for ^{12}B [13] and ^{12}Be [14] are included. There is good consistency for the energy of the first $T=2$ $J^\pi=2^+$ state. The second such 2^+ state in ^{12}Be is not known, but a state at $E^*=4.580$ MeV has been assigned as either 2^+ or 3^- [14]. This state is at the right energy to be the mirror of the 2_2^+ state in ^{12}O and thus leads us to strongly favor the 2^+ assignment.

The masses in an isospin multiplet are expected to follow the isospin multiplet mass equation (IMME),

$$\Delta M = a + bT_z + cT_z^2, \quad (6.1)$$

if isospin is a good quantum number [99]. The largest deviations from this behavior have been found for $A=8$ and 9 [99, 100, 98]. Deviations from the IMME for $A=12$ quintet were previously examined in [53], but with our newer, more accurate measurement for ^{12}O and ^{12}N it is worth examining again. The mass excess for the quintets associated with the 0^+ and first and second 2^+ $T=2$ states are plotted in Fig. 6.8(a). Results for ^{12}C were taken from [14] and for the second 2^+ state of ^{12}Be , we have included the candidate state previously mentioned. The curves show fits with the quadratic IMME which can reproduce the data validating our assumption that the ^{12}N states are $T=2$.

Figure 6.8(b) shows deviations from the quadratic form for the two lower-energy quintets.

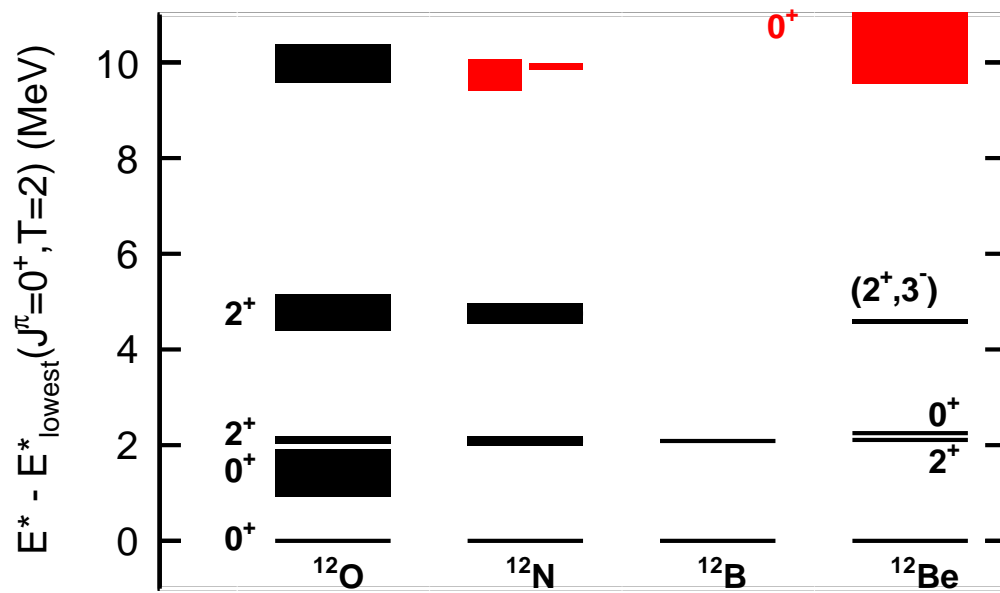


Figure 6.7: Level schemes for $A = 12$ and $T = 2$ states with excitation energy plotted relative to the first $J^\pi = 0^+$ state. The results for ^{12}O and ^{12}N are from this work, the ^{12}B levels are from [13], and the ^{12}Be levels from [14, 15].

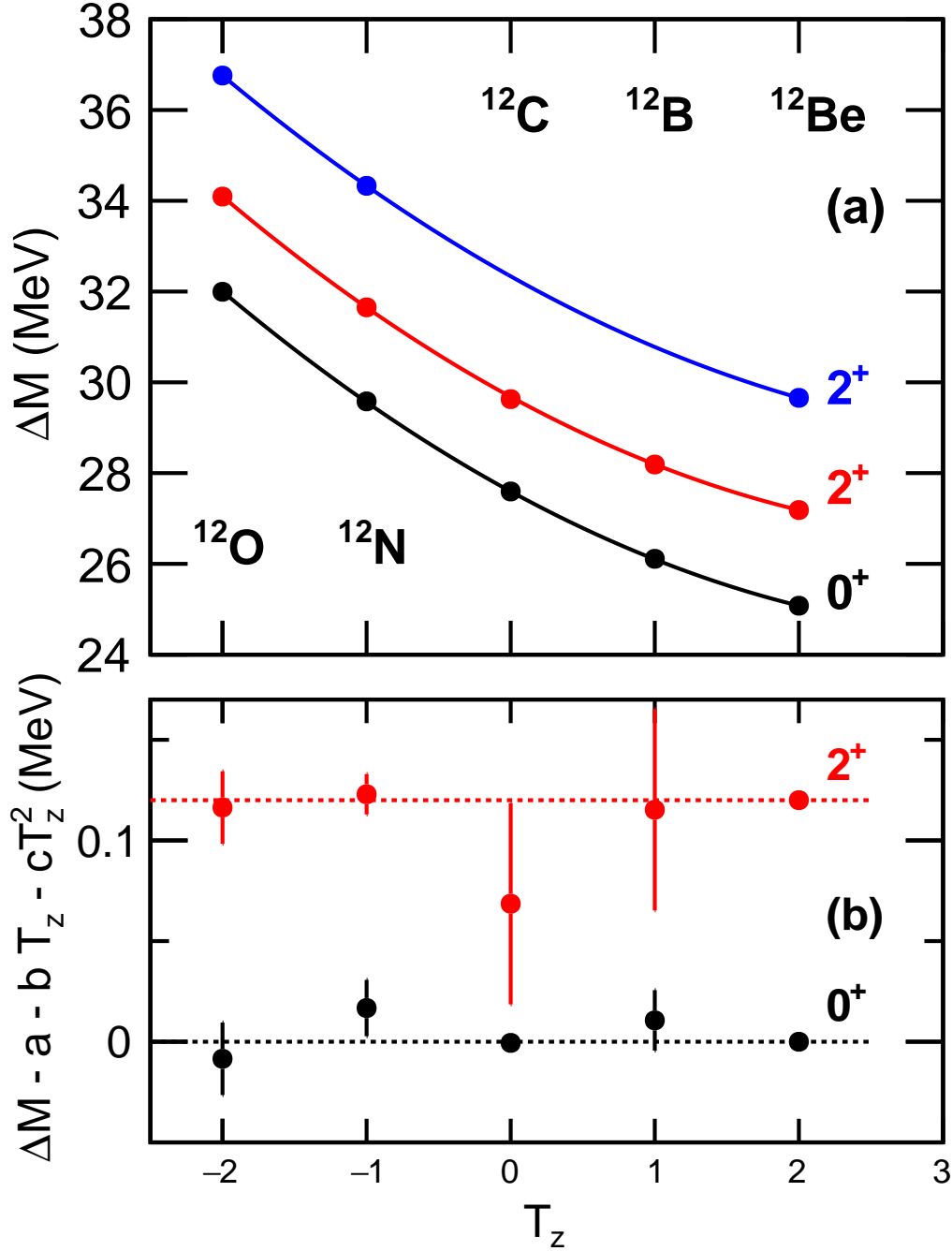


Figure 6.8: (a) Mass excesses of three lowest $A=12$ quintets as a function of isospin projection T_z . The curve through the data points are fits with the quadratic IMME [Eq. (6.1)]. (b) Deviations from the IMME fit for the lowest quintets. The results for the 2^+ states have been shifted up along the Y-axis for clarity. The statistical and systematic errors for the ^{12}O and ^{12}N data points from this work are of similar magnitude. We have combined them in quadrature for these fits.

The error bars on some of the points for the 2^+ states are too large to look for meaningful deviations from the IMME. In the case of the 0^+ states, if we include a cubic term (dT_z^3) to Eq. (6.1), then we find $d = 1.6(37)$ keV consistent with zero and small compared to values of $d=8.36(21)$ keV for the $A=8$ quintet and $d=6.33(16)$ keV for the $A = 9$ quartet [101]. There is thus no evidence for deviations from the quadratic IMME for the $A=12$ quintet.

The fission-like channels ${}^6\text{Be}_{g.s.} + {}^6\text{Be}_{g.s.}$, ${}^6\text{Be}_{g.s.} + {}^6\text{Li}_{IAS}$, $\alpha + {}^8\text{C}_{g.s.}$, and $\alpha + {}^8\text{B}_{IAS}$ remind us of the ${}^6\text{He} + {}^6\text{He}$ and $\alpha + {}^8\text{He}$ decay channels for levels in ${}^{12}\text{Be}$ observed in [102, 103] and which were associated with a molecular $\alpha:2n:\alpha$ band structure [102]. The lowest member of this band was subsequently found at $E^*=10.3$ MeV [104, 15] and shown to be $J^\pi=0^+$. The location of this level is plotted in Fig. 6.7 for comparison. While its excitation energy would be appropriate for an analog to the fission-like states we observed in ${}^{12}\text{O}$ and ${}^{12}\text{N}$, its quoted width of $\Gamma = 1.5(2)$ MeV is too large to be consistent as higher T_Z systems are closer to stability and thus should have smaller widths. In any case these fission-like decay modes suggest these states have strong cluster structure.

Chapter 7

^{10}N

7.1 Introduction

The nuclide ^{10}N , which is proton unbound in its ground state, has been the subject of very few experimental studies. The ENSDF database [14] only presents information from one study by Hooker *et al.* [16], where level energies and widths for the ground and first excited state were deduced from resonant proton scattering on ^9C . These two states were found to be *s*-wave resonances and thus should correspond to $J^\pi=1^-$ and 2^- , but their energy order could not be determined.

The mirror of ^{10}N , ^{10}Li , is neutron-unbound but the description of its ground state is complicated by the likely presence of a virtual state [105, 106]. Understanding of the n - ^9Li interaction is also important for understanding the iconic nucleus ^{11}Li which has an extended neutron halo [40]. In the same sense, the ^{10}N resonances are important in understanding the structure of the newly discovered ^{11}O system [107]. The ground and excited states of this nucleus undergo $2p$ decay and the ^{10}N levels represent possible intermediate states in sequential-decay branches [60, 19].

This chapter presents a new data on the low-lying ^{10}N states created in multi-nucleon knockout reactions from a fast beam of ^{13}O . Fitting of the invariant-mass spectrum provides

resonance parameters (energy and width) of the first excited state for both the possible level orderings. When these constraints are applied to the resonance-scattering data of Hooker *et al.* [16], a favored ordering of the two low-lying states in ^{10}N emerges.

7.2 Invariant-mass Spectra

The invariant masses M_{inv} of detected $p+^9\text{C}$ coincidences were determined and the decay kinetic energy of ^{10}N states was obtained as by subtracting the masses of the decay products, i.e., $E_T = M_{inv} - M_p - M_{^9\text{C}}$. The spectrum in Fig. 7.1(a) shows the raw E_T spectrum determined for $|\cos\theta_p| < 0.5$ where θ_p is the emission angle relative to the beam in the ^{10}N center-of-mass frame. This gate on transverse emission improves the invariant-mass resolution as demonstrated in [28]. We have identified three sources of contamination which are also shown in this figure.

The light output of the CsI(Tl) crystals from the calibration beams show a low-energy tail due nuclear reactions in the crystals. This tail causes some heavier carbon isotopes to be misidentified as ^9C . To estimate this component, we have analyzed $p+^{10}\text{C}$ and $p+^{11}\text{C}$ events as if the detected carbon fragment was ^9C . These distributions were scaled by the magnitude of the contamination determined with the calibration beams ($\sim 0.5\%$). The largest contribution from this effect comes from the proton decay of the $J^\pi=2_1^+$ first-excited state of ^{12}N which produces the peak at $E_T \sim 330$ keV. Two-neutron knockout reaction produce ^{11}O states which decay to the $2p+^9\text{C}$ channel [107]. If only one of the two proton is detected, then these events will populate the experimental $p+^9\text{C}$ spectrum. We have taken the detected $2p+^9\text{C}$ events and randomly removed one of the protons to give a $p+^9\text{C}$ invariant mass. This invariant distribution was scaled based on our Monte Carlo simulations to give the correct magnitude of this contamination.

The contamination-subtracted distribution is plotted as the data-points in Figs. 7.1(b) and 7.1(c). The spectrum contains one wide peak with a maximum at $E_T \sim 2.6$ MeV.

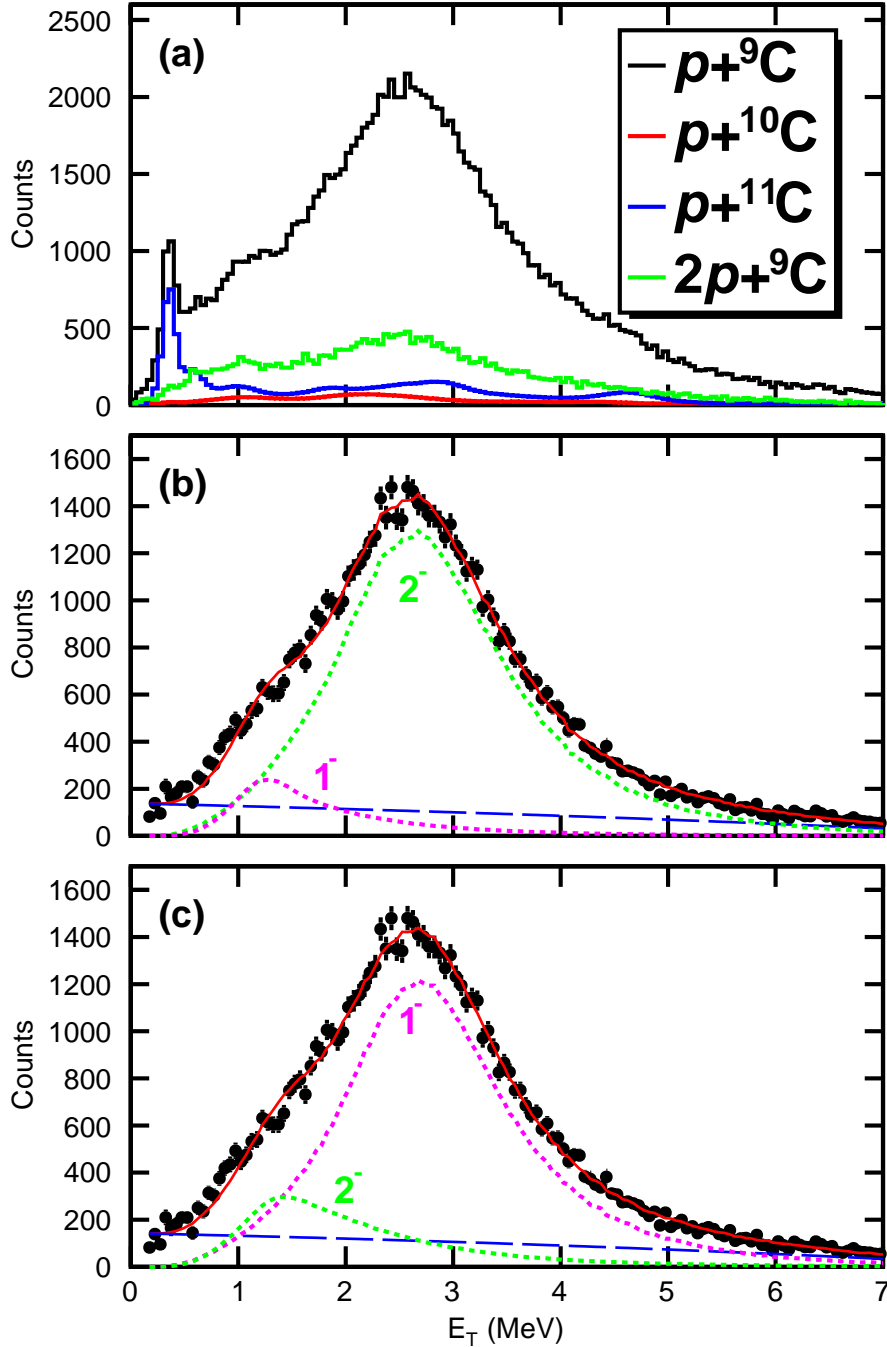


Figure 7.1: (a) Raw experimental $p+{}^9\text{C}$ invariant-mass distribution (black) and the estimated contamination from $p+{}^{10}\text{C}$ and $p+{}^{11}\text{C}$ events where the carbon fragment was misidentified as ${}^9\text{C}$. The contamination from ${}^{11}\text{O}\rightarrow 2p+{}^9\text{C}$ events where only one of the two protons is detected is also shown. (b,c) Contamination-subtracted spectrum (data points) with two-level fits (solid red curve). The contribution from each level is shown as the dotted curves while the fitted smooth background is shown as the blue-dashed curve. The fits are shown for ground-state lineshapes expected for (b) a $J^\pi=1^-$ level or (c) a $J^\pi=2^-$ level.

Based on the level parameters determined in the resonance-scattering experiment, this peak is dominated by the decay of the first-excited state, with only minor contribution from the ground-state decay at the lower E_T values. As such, this data can be used to better constrain the excited-state level parameters and these can subsequently be used to further constrain the analysis of the resonance-scattering data. We have thus fit the invariant-mass spectrum as the sum of two R -matrix lines shapes. The ground-state parameters are fixed to the values obtained in the resonance-scattering analysis while the excited-state values are allowed to vary. This fitting was performed with the two ground-state solutions of [16], i.e. where the 1^- or the 2^- level is the ground state

In the isolated level approximation [92], the lineshape for a channel λ is given by

$$D(E) \propto \frac{\Gamma_\lambda(E)}{(E_\lambda + \Delta_\lambda(E) - E)^2 + \frac{1}{4}\Gamma_\lambda(E)^2} \quad (7.1)$$

where energy-dependent decay width is

$$\Gamma_\lambda(E) = 2P_c(E)\gamma_{\lambda c}^2 \quad (7.2)$$

and

$$\Delta_\lambda(E) = -(S_c(E) - S_c(E_\lambda))\gamma_{\lambda c}^2. \quad (7.3)$$

Here $P_c(E)$ are the penetration factors and $S_c(E)$ are the shift functions given in [92] and, following [16], we set the channel radius $a_c=5$ fm. The fit parameters include the magnitude of each level, the width and centroid of the excited state and some parameters describing a smooth background. These lineshapes were used in the Monte Carlo simulations to incorporate the effect of the detector efficiency and resolution.

The fits are shown as the solid red curves in Figs. 7.1(b) and 7.1(c) with contributions from the individual levels shown as the dotted curves and the blue-dashed curve is the fitted background. Excellent agreement with the experimental data is obtain with both ground-

state solutions. The fitted R -matrix parameters are listed in Table 7.1. We point out that the excitation energy and the reduced width for the first excited state are well defined by the invariant mass spectrum and they are almost independent on the specific spin-parity assignment.

7.3 Discussion

In the original R -matrix fit of $p+{}^9\text{C}$ resonance scattering data of Hooker et al [16], excitation energies and reduced widths for both the ground and the first excited states were considered as free parameters. The two solutions (2^- g.s. and 1^- excited state, and 1^- g.s. and 2^- excited state) produced almost identical fits shown as a solid black curve in Fig. 7.2 (normalized $\chi^2=1.3$ in both cases). However now using the invariant-mass-deduced paired values of the c.m. energy and reduced width (for the first excited state) yields a noticeable difference between the $2^-/1^-$ and $1^-/2^-$ solutions. The 2^- ground-state solution, shown as a red-dashed curve in Fig. 7.2, reproduces the resonance scattering excitation function better than the 1^- ground-state solution. The latter is visually worse (blue-dotted curve in Fig. 7.2) and has $\chi^2=3.6$ vs $\chi^2=2.1$ for the 2^- ground-state solution.

Therefore, by combining the two different data sets, the $p+{}^9\text{C}$ resonance scattering and the $p+{}^9\text{C}$ invariant-mass spectrum produced in multi-nucleon knockout reactions with fast ${}^{13}\text{O}$ beam, the preferred 2^- spin-parity assignment was obtained for the ground state of ${}^{10}\text{N}$.

The preferred 2^- spin-parity assignment is not surprising. The relevant systematics for neighboring odd-odd nuclei are shown in Table 7.2. In every case the spin-spin interaction between a valence proton(neutron) in the $2s_{1/2}$ shell and an unpaired $1p_{3/2}$ -shell neutron(proton) in the core makes the higher spin partner more bound (or less unbound). The corresponding 2^- and 1^- states are well known in ${}^{12}\text{N}$, ${}^{12}\text{B}$, and ${}^{10}\text{B}$ [108, 109]. In ${}^8\text{B}$ the 2^- state has been observed as a broad resonance [110], but the 1^- state has not been found, so it is very likely that it is more unbound. The recent measurements of the ${}^7\text{Be}+p$ s-wave

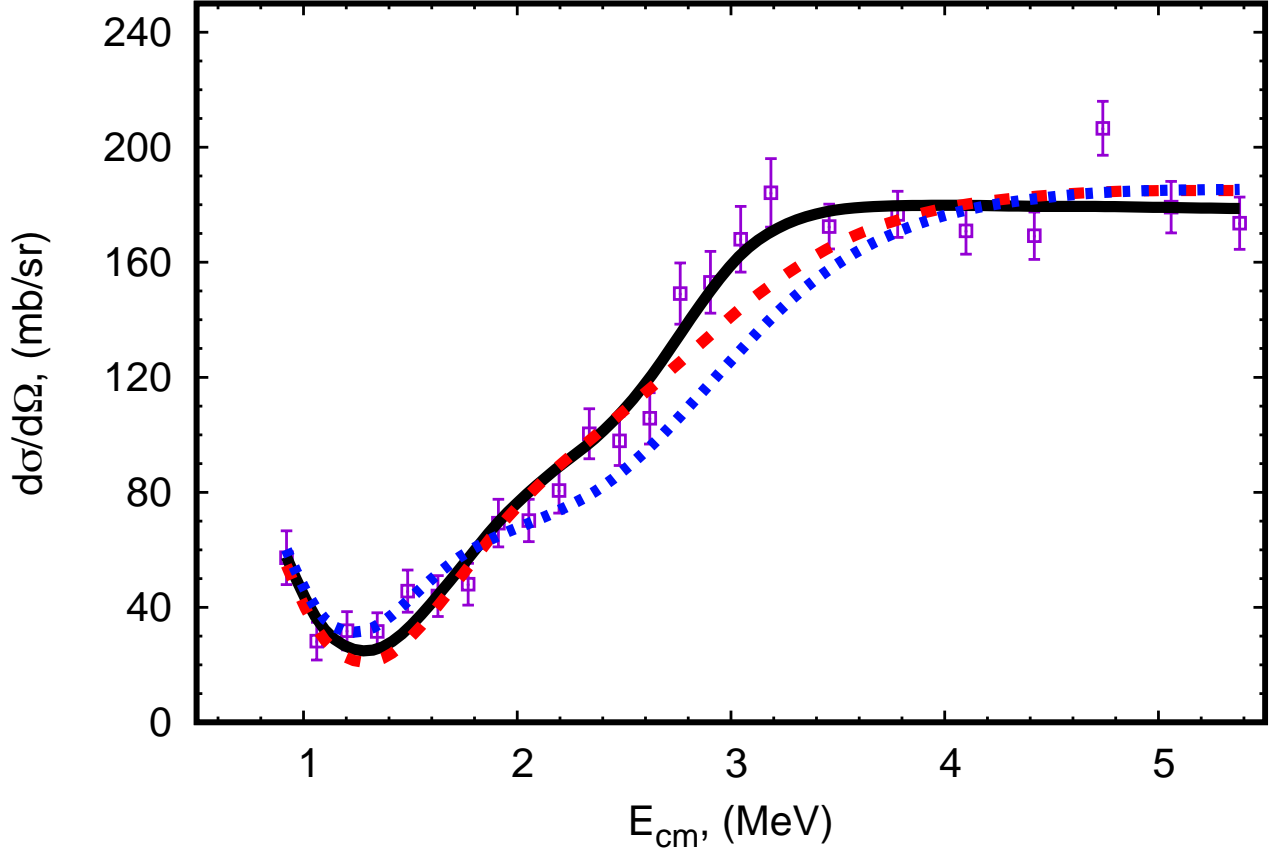


Figure 7.2: Excitation function for ${}^9\text{C}+p$ resonance elastic scattering. Data is from Ref. [16]. The black solid curve is the best R-matrix fit from Ref. [16] that was obtained using 2^- g.s. and 1^- excited state spin-parity assignment for the two broad s-wave resonances. (The $1^-/2^-$ solution is almost identical, so it is not shown). The red dashed curve is the 2^- ground state and 1^- excited state and the blue dotted curve is the 1^- ground state and 2^- excited state, but with parameters for the excited state taken from the invariant mass fit (Table 7.1).

Table 7.1: Fitted R -matrix parameters for the 1^- and 2^- state with the two energy orderings. The centroid and width of the states calculated from the pole ($E_{pole} - i\frac{\Gamma_{pole}}{2}$) of the S -matrix are also shown.

J_π	E_λ MeV	$\gamma_{\lambda c}$ MeV ^{1/2}	E_{pole} MeV	Γ_{pole} MeV
2 ⁻ ground-state solution				
2 ⁻	1.741	1.281	1.268	1.130
1 ⁻	3.078(28)	0.966(26)	2.681	2.151
1 ⁻ ground-state solution				
1 ⁻	1.450	1.133	1.191	0.976
2 ⁻	3.062(32)	1.009(22)	2.596	2.820

Table 7.2: Systematics for splitting due to interaction between a 2s1/2-shell valence proton(neutron) with a 1p3/2-shell unpaired neutron(proton) in light nuclei.

State	Excitation Energy MeV	Ref.
¹² N, ¹¹ C(3/2 ⁻)+p(2s1/2)		
2 ⁻	1.19	[108]
1 ⁻	1.80	[108]
¹² B, ¹¹ B(3/2 ⁻)+n(2s1/2)		
2 ⁻	1.67	[108]
1 ⁻	2.62	[108]
¹⁰ B, (⁹ Be(3/2 ⁻)+p(2s1/2)) × (⁹ B(3/2 ⁻) + n(2s1/2))		
2 ⁻	5.11	[109]
1 ⁻	6.873	[109]
⁸ B, (⁷ Be(3/2 ⁻)+p(2s1/2))		
2 ⁻	3.5 ($a_{2^-} = -3.2(5)$ fm)	[110, 111]
1 ⁻	$a_{1^-} = 17(1)$ fm	[111]

scattering lengths [111], $a_{2^-} = -3.2(5)$ fm and $a_{1^-} = 17(1)$ fm, clearly indicate stronger attraction for the 2⁻ partial wave.

This finding is consistent with Nordheim's second jj coupling rule [112] (nominally for unpaired nucleons in the same Schmidt class) that higher resultant spins are favored. This rule is made stronger, and unambiguous, by the Brennan-Bernstein revisions [113] where, when either the proton or neutron has $j=1/2$, the ground state is the additive (i.e. the greater) spin. This is true for all cases in Table 7.2. (The actual ground state of ¹⁰B follows from the same rule when the single-particle configurations are both p-shell.)

In using the invariant-mass lineshape from knock-out reactions to constrain resonance-scattering we are assuming there is no reaction dependence. This is certainly true for narrow resonances, however for very wide resonances some dependence has been predicted. For example, a large dependence of the lineshape was predicted for the second 2^+ state in ${}^6\text{Be}$ ($\Gamma \sim 7$ MeV), formed in neutron knockout reactions from a ${}^7\text{Be}$ beam, depending on the assumed structure of ${}^7\text{Be}$ [114]. However for the narrower 2_1^+ state ($\Gamma=1.1$ MeV), the effect was minor. In this work, the excited ${}^{10}\text{N}$ state has width of $\Gamma=2-3$ MeV so there is a possibility of a modest effect which may cast some uncertainty on our final results. A modest reaction dependence might explain the somewhat worse fit when the invariant-mass parameters were used (for the first excited state) as compared to the original unconstrained fit. Until this effect can be better characterized, the present result still represents the best constraint on the spin-parity assignments for the ${}^{10}\text{N}$ levels.

In conclusion, an analysis that utilizes both ${}^9\text{C}+p$ resonance scattering and invariant-mass data favors the spin-parity of the ${}^{10}\text{N}$ ground state to be 2^- . Even for the truly exotic nucleus, Nordheim's rules, still rule.

Chapter 8

Experimental Verification of the JSIR-BVM Approach for Computing Proton Stopping Power Ratios

8.1 Background

8.1.1 Goals

Proton-beam therapy is of major clinical interest because of the rapid dose fall-off at the end of the proton-beam range. This feature of proton beams allows for the sparing of healthy tissue distal to the tumor site, or clinical target volume (CTV), and for increased dose uniformity. These advantages depend, however, on accurate alignment with the distal edge of the CTV. Current clinical practice dictates an additional 2-3.5% margin on the proton range calculated from single energy CT-based stopping power mappings [115, 116, 117]. Thus, improving proton therapy's efficacy requires improving patient-specific stopping power ratio (SPR) mapping.

Dual-energy CT (DECT) methods have been developed for estimating SPR distributions. DECT techniques scan at two energies in an effort to extract two independent properties

of the scanned material, often electron density (ρ_e) and effective atomic number (Z_{eff}), as variations in these quantities lead to more robust SPR estimation than the single energy calibration method [118, 119, 120]. This method involves mapping single energy CT Hounsfield units (a quantitative standard scale used for describing radiodensity) to SPR for biological tissues by use of a calibration curve [121]. What this chapter presents is the experimental verification of a new, very accurate, non-image-based iterative reconstruction method of proton stopping power ratios.

8.1.2 The JSIR-BVM

Sinogram-based DECT methods have been shown to better compensate for the polychromatic nature of CT x-ray beams and improve performance over image-based reconstruction models [122, 123]. As mentioned in the introduction, a sinogram is defined as the Radon transform of the attenuation coefficient plotted with detector index and the rotation angle of the source-detector pair as independent variables. The sinogram can then be reconstructed into a cross-sectional image of the scanned material.

In the past, a linear basis vector model (BVM) has been investigated that parameterizes tissue properties as a linear combination of two basis materials [124, 125, 126]. The model has been shown to accurately approximate monoenergetic proton cross-sections and proton SPRs. This model can be used in conjunction with a model-based joint statistical reconstruction (JSIR) algorithm, the dual-energy alternating minimization (DEAM) algorithm [127], to reconstruct SPR maps from sinogram data. The DEAM algorithm is an iterative algorithm that reconstructs quantitatively accurate images based on a CT forward model. Previous studies have shown that that JSIR-BVM approach provides more accurate and precise proton SPR mapping than image- or sinogram-based decomposition approaches [128] and that the approach could be used on raw DECT data exported from a clinical scanner to accurately reconstruct proton SPRs [129].

Proton SPR is linked to DECT measurements by using the BVM to parametrize the

photon linear attenuation coefficient and stopping power as a linear combination of two dissimilar basis materials [124, 125, 126]. This approach is directly applied by reconstructing two images of the BVM weights using the DEAM algorithm and estimating electron density and mean excitation energy from the reconstructed BVM weights. These quantities are then used to calculate the SPR using Eq. 1.7. To reconstruct the images of the BVM weights from dual-energy sinogram data, the DEAM considers a statistical, polychromatic CT model to reconstruct both BVM images by solving a penalized maximum likelihood estimation (MLE) problem. Maximum likelihood estimation is used to estimate a set of parameters (in our case, the BVM weights) that best model observed data. MLE obtains these parameters by maximizing a likelihood function, though, as will be discussed shortly, one can also minimize the difference between observed data and the statistical model.

The statistics of energy integrating detectors in clinical CT scanners are approximately Poissonian [130], so the obtained transmission data, $d_j(y)$, are independently Poisson distributed with means

$$Q_j(y : \boldsymbol{\mu}) = I_{0,j}(y) \sum_E \psi_j(y, E) e^{-\sum_x h(y|x)\mu(x,E)} + \gamma_j(y), \quad (8.1)$$

where $I_{0,j}(y)$ is the unattenuated source intensity spectrum for each detector, $\psi_j(y, E)$ is the normalized detector-response weighted spectrum of the j th scan, $\gamma_j(y)$ is the mean of the background events (scattered radiation), and $h(y|x)$ is the effective length of the intersection of the ray path (y) and the image pixel (x). The scanner's bow-tie filter, a filter placed after the source that is intended to reshape and equalize the x-ray flux across different detector channels during a clinical scan of a patient, creates a detector dependence in the source intensities and spectra.

In the BVM, the x-ray linear attenuation coefficient for human tissue is represented by a linear combination of basis materials,

$$\mu(x, E) = c_1(x)\mu_1(E) + c_2(x)\mu_2(E) \quad (8.2)$$

where $\mu_i(E)$ are the linear attenuation coefficients of the basis materials and $c_i(x)$ are the corresponding tissue-specific BVM weights. Equation 8.2 can be combined with Eq. 8.1 to yield

$$Q_j(y : \mathbf{c}) = I_{0,j}(y) \sum_E \psi_j(y, E) e^{-\sum_x h(y|x) \sum_{i=1}^2 c_i(x) \mu_i(E)} + \gamma_j(y). \quad (8.3)$$

The MLE of the BVM components is found by converting the maximization of the the Poisson log-likelihood function to an equivalent problem [131], the minimization of the I -divergence (a measure of the discrepancy between two nonnegative functions) between the measured transmission data \mathbf{d}_j and the estimated mean values \mathbf{Q}_j ,

$$d_I(\mathbf{d}_j || \mathbf{Q}_j) = \sum_y \left(d_j(y) \log \frac{d_j(y)}{Q_j(y)} - d_j(y) + Q_j(y) \right). \quad (8.4)$$

To enforce image smoothness, a regularization term is also employed. The objective function of the minimization problem, including this regularization term, is then

$$g(\mathbf{c}_1, \mathbf{c}_2) = \sum_{j=L,H} d_I(\mathbf{d}_j || \mathbf{Q}_j) + \lambda \sum_{i=1}^2 R(\mathbf{c}_i), \quad (8.5)$$

where λ determines the level of regularization, controlling the trade-off between image smoothness and data fitting. $R(\mathbf{c}_i)$ is a term that penalizes differences between neighboring pixels.

Direct minimization of Eq. 8.5 is difficult, so the DEAM algorithm instead alternatively minimizes a decomposed surrogate function during each iteration, ensuring a monotonic decrease of the objective function. See Ref. [127] for details on the DEAM.

8.1.3 The BVM for Computing Proton SPR

The electron density and mean excitation energy used for calculating SPR are obtained from the reconstructed BVM weight images. The electron density for a tissue can be easily

calculated by the linear combination [125]

$$\hat{\rho}_e(x) = c_1(x)\rho_{e,1} + c_2(x)\rho_{e,2}, \quad (8.6)$$

where $\rho_{e,i}$ are the electron densities of the basis materials weighted by the BVM weights obtained from the images. This relationship can be extended to non-biological materials with similar compositions to tissues, which is relevant for the experiments presented in this chapter.

The I -value, however, cannot be determined directly from CT images. We use an estimation that relates the logarithm of the I -value to the weighted-component ratio

$$r_c(x) = \frac{c_1(x)\rho_{e,1}}{c_1(x)\rho_{e,1} + c_2(x)\rho_{e,2}}. \quad (8.7)$$

This has been shown to be a robust estimation method [129]. Thus, the estimated I -value is

$$\hat{I}(x) = \exp(a \cdot r_c(x) + b), \quad (8.8)$$

where a and b are fitted parameters.

8.2 Experimental Methods

8.2.1 CT Experiment

Rigid cylindrical PVC containers, of length 10 cm and diameter 5 cm, containing the liquids in Table I were scanned on a Phillips Brilliance Big Bore CT scanner. The composition and densities of the materials are also given in Table I. The compositions were determined by measuring the mass of the solute and the mass of the deionized water solvent at the time of production. The densities were determined by measuring the mass of 100mL samples of the materials on a quantitative balance. The set-up for the scan of the three soft tissue

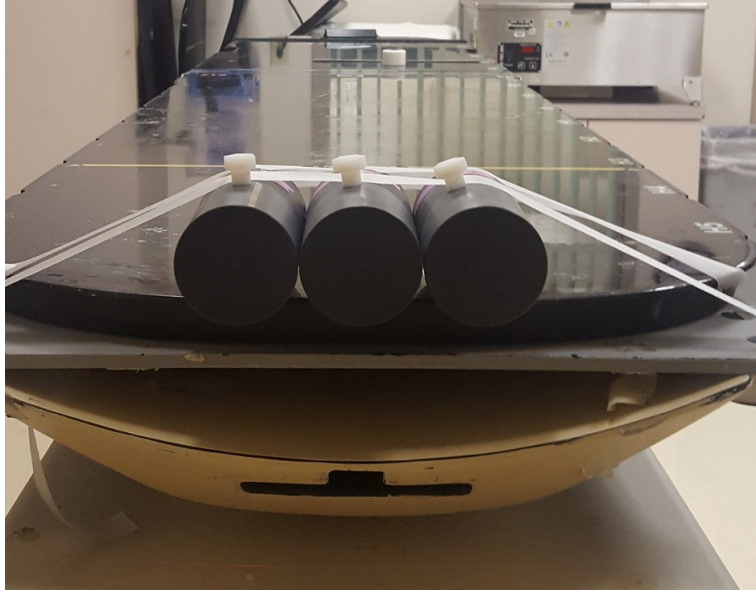


Figure 8.1: A front-view image of the bottles containing the three soft tissue surrogates in their scan geometry. The x-ray source is above the bottles out of the frame, and the detector array is below out of the frame.

surrogates is shown in Fig. 8.1.

The materials are intended to serve as tissue surrogates, and are divided into two categories, bony and soft tissue. The bony materials are aqueous K_2HPO_4 solutions and the soft tissue materials are composed of water and alcohols. A container containing no material, only air, was also scanned.

The materials were scanned at 4 different beam collimations: 3 mm, 6 mm, 12 mm, and 24 mm. The tube potentials were set to 90 kVp (600 mA·s) and 140 kVp (200 mA·s). The potentials listed are the endpoint (maximum) energies of the emitted polychromatic x-rays. All data presented here were obtained by analyzing the scans with 3 mm collimation. The spectra of the two endpoint energies were determined using the equivalent spectrum method, as explained in [132]. The spectra were measured by fitting the Birch-Marshall model to measured beam transmission profiles through varying-thickness aluminum and copper attenuators. This scan protocol is very similar to the one discussed in [129].

Table 8.1: A summary of the properties of the aqueous solutions used in these experiments.

Category	Material	Composition	Density (g/mL)
Soft	Ethanol	C ₂ H ₅ OH	0.789
	n-Propanol	C ₃ H ₇ OH	0.803
	n-Butanol	C ₄ H ₉ OH	0.826
	Water	H ₂ O	0.997
Bony	KP-1	K ₂ HPO ₄ (10.26%)	1.085
	KP-2	K ₂ HPO ₄ (20.81%)	1.174
	KP-3	K ₂ HPO ₄ (28.96%)	1.261
	KP-4	K ₂ HPO ₄ (34.64%)	1.338

8.2.2 Proton Experiment

The stopping power ratios of the liquid samples were measured directly using a MEVION S250 superconducting synchrocyclotron. A proton beam was delivered with a water penetrating depth of 25 cm and was collimated to a 25 cm² square using brass blockers. The containers filled with the samples were sandwiched between the brass collimator and a water tank outfitted with a moving ion chamber. The proton beam was passed through each sample individually, and an IBA PPC05 parallel plane ion chamber was scanned along the beam path, measuring the delivered dose to find the Bragg peak. The ion chamber was set to measure the dose along the beam path in 1 mm steps, measuring at each point for 2 seconds. When the location of the Bragg peak was found, each point in the Bragg region was then measured for 8 seconds to sample the dose in the region with higher statistics. The experimental setup is shown in Fig. 8.2. The ion chamber's isocenter is located right next to the proximal tank wall, near where the blockers are placed.

The location of the Bragg peak is directly related to the range of the incident protons. The range, defined as the distance traveled by a charged particle before stopping, of particle radiation in matter is determined by the kinetic energy of the particle and the stopping power of the material it passes through. By passing a proton beam of constant energy through samples with different stopping powers, the stopping power ratio (*SPR*) of each

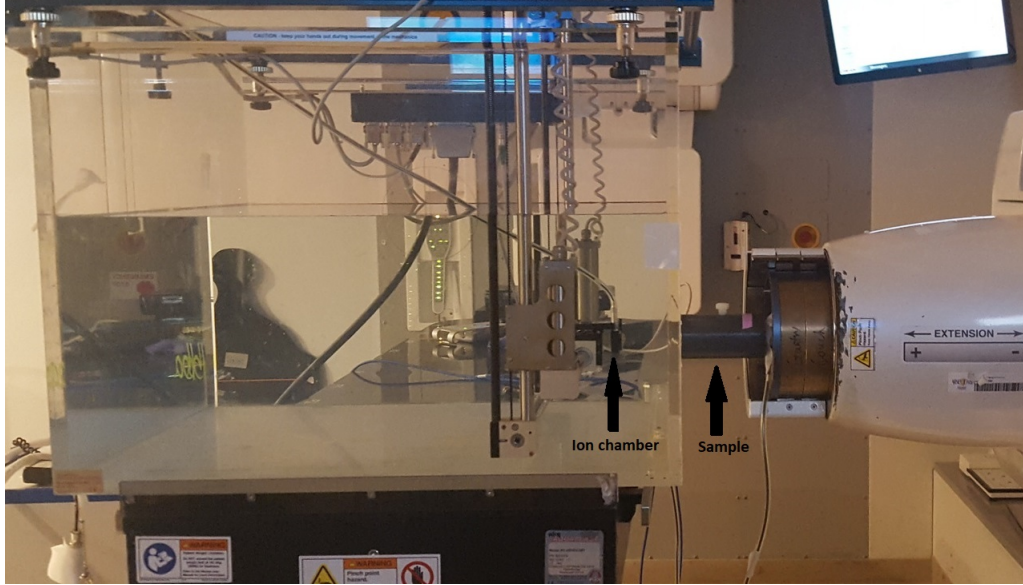


Figure 8.2: The setup used for the proton stopping power measurements. The water tank is on the left, with the the ion chamber apparatus near the right wall. The sample is sandwiched between where the blockers are placed and the water tank.

sample relative to water can be determined, as defined by the equation

$$SPR = \frac{R_{air} - R_{sample}}{R_{air} - R_{water}}, \quad (8.9)$$

where R_{air} is the range after passing through air, R_{sample} is the range through the sample, and R_{water} is the range through water.

An alternate formulation of the SPR is

$$SPR = \frac{R_{air} - R_{sample}}{L}, \quad (8.10)$$

where L is the inner length of the container. A useful check of our method is to investigate if the relationship $L = R_{air} - R_{water}$ holds. The value extracted for $R_{air} - R_{water}$ is 99.77 mm. This is within the tolerance of our bottles which were manufactured to have an active inner length of 100.00 ± 0.25 mm, which lends confidence in this approach.

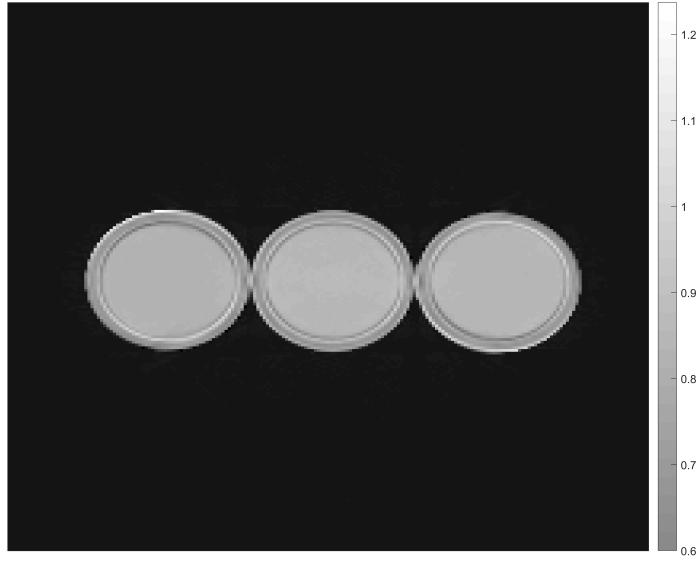


Figure 8.3: A reconstructed proton SPR map of the alcohol samples. The z-axis is the reconstructed proton SPR.

8.3 Analysis and Results

A proton SPR map reconstructed using the JSIR-BVM of the soft tissue samples pictured in Fig. 8.1 is shown in Fig. 8.3. The material-specific I-value parameterization is the same as in [129]. For reference, it is defined as

$$\ln I = \begin{cases} -1.746r_c + 5.835, & r_c \geq 0.75, \\ -0.269r_c + 4.551, & r_c < 0.75. \end{cases} \quad (8.11)$$

Using this parameterization and Eqs. 8.6 and 8.7, it is possible to define the SPR for the tissue surrogates as

$$SPR = \begin{cases} 1.056 \cdot c_1 + 0.973 \cdot c_2, & r_c \geq 0.75, \\ 1.033 \cdot c_1 + 1.154 \cdot c_2, & r_c < 0.75, \end{cases} \quad (8.12)$$

where c_1 and c_2 are the reconstructed weights.

Figure 8.4 shows three normalized dose depth curves created using data taken from the

Table 8.2: The reconstructed properties of the tissue surrogates and a comparison of the theoretical, the reconstructed, and the directly measured SPR.

Material	$\rho_e/\rho_{e,w}$	I (eV)	Theoretical SPR	Reconstructed SPR	Experimental SPR
Ethanol	0.804	63.1	0.820	0.824	0.825
n-Propanol	0.821	61.5	0.840	0.844	0.843
n-Butanol	0.826	60.5	0.847	0.856	0.851
Water	0.997	75.3	1.000	1.000	
KP-1	1.076	80.6	1.068	1.073	1.066
KP-2	1.165	86.7	1.146	1.145	1.151
KP-3	1.235	91.7	1.207	1.203	1.200
KP-4	1.288	95.5	1.253	1.249	1.253

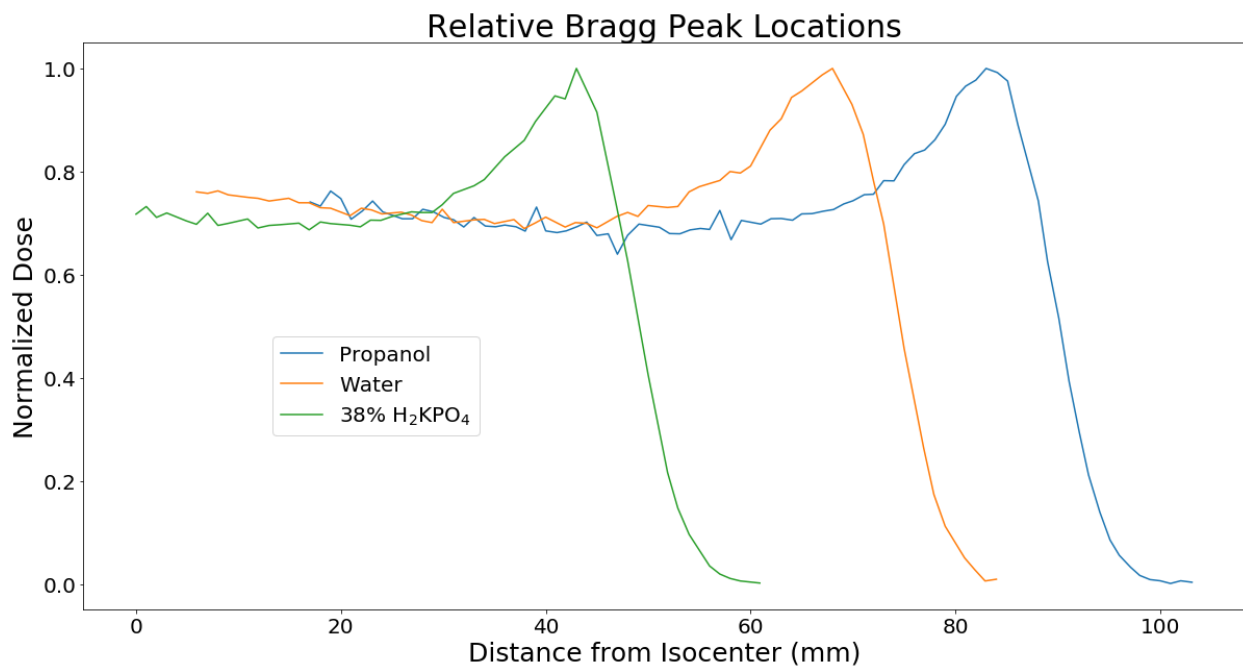


Figure 8.4: Normalized data taken using the setup shown in Fig. 8.2 for three different samples, denoted by the colored curves. The location of the Bragg peak clearly shifts between samples, moving closer to the proton source as the stopping power of the materials increase.

experimental setup in Fig. 8.2 for three different samples. The Bragg peaks for the three materials are clearly seen. It is also clear that they are spread out relative to each other, with the bony tissue surrogate (the K_2HPO_4) located closer to the isocenter than water, and quite far from the Bragg peak of the soft tissue surrogate, propanol. This conforms to our expectation, that by passing protons through a uniform path length of materials with varying stopping powers, we can shift the detected Bragg peak. For the purposes of this experiment, a Bragg peak location at a smaller distance relative to the isocenter corresponds to a material with a higher relative stopping power ratio.

The Bragg peak locations are used as the ranges in Eq. 8.9. The location of the Bragg peak for each material is determined by fitting the normalized dose-depth curve with a sum of five Gaussians and minimizing the equation

$$\min_x f(x) = 1 - \sum_{i=1}^5 a_i \exp -\frac{(x - b_i)^2}{c_i^2}, \quad (8.13)$$

where a_i , b_i , and c_i are fitted parameters. This is equivalent to finding the maximum point of the fitted function, which corresponds to the peak dose delivered.

Table 8.2 shows the reconstructed electron density ratios, mean excitation energies, the resulting SPR values, and the experimentally measured SPR values. A full error analysis has not been carried out for the experimental values, but there appears to be good agreement between the three values for most of the surrogates.

It is useful and illustrative to compare the water equivalent path length (WEPL) of the reconstructed images and ones generated using the directly measured value of the stopping power ratio. The WEPL is defined as a distance traveled by a beam of charged particles passed through matter that is equivalent to the distance were the charged particles to pass through water. The WEPL is computed by taking the Radon transform of the reconstructed SPR image for 150 parallel beams of width 1 mm for every degree, essentially integrating SPR along a beam path. This was done for both the reconstructed images of the bottles and

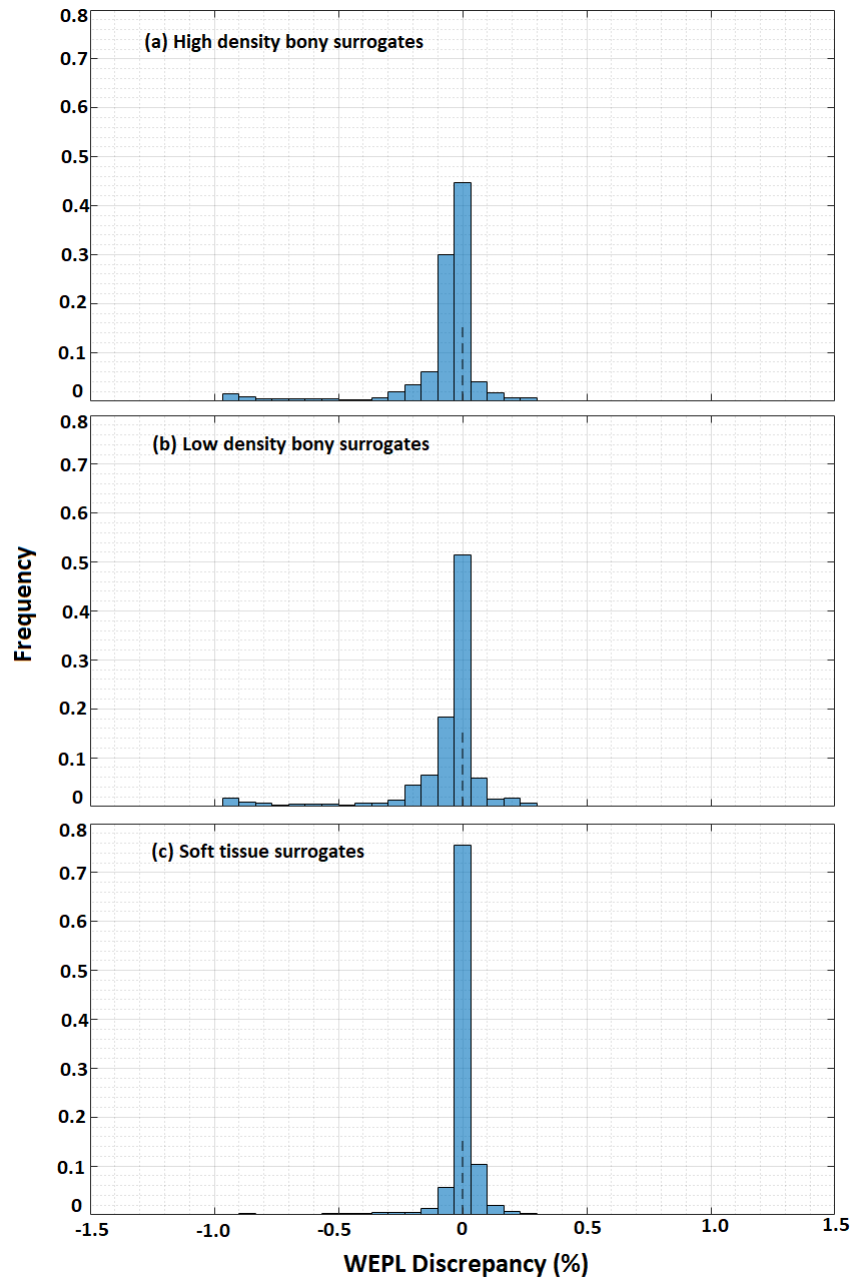


Figure 8.5: The WEPL discrepancy between the reconstructed SPR images and the SPR measured using the proton therapy machine for (a) the two highest-density bony tissue surrogates, (b) the two lower-density bony tissue surrogates, and (c) the three soft tissue surrogates.

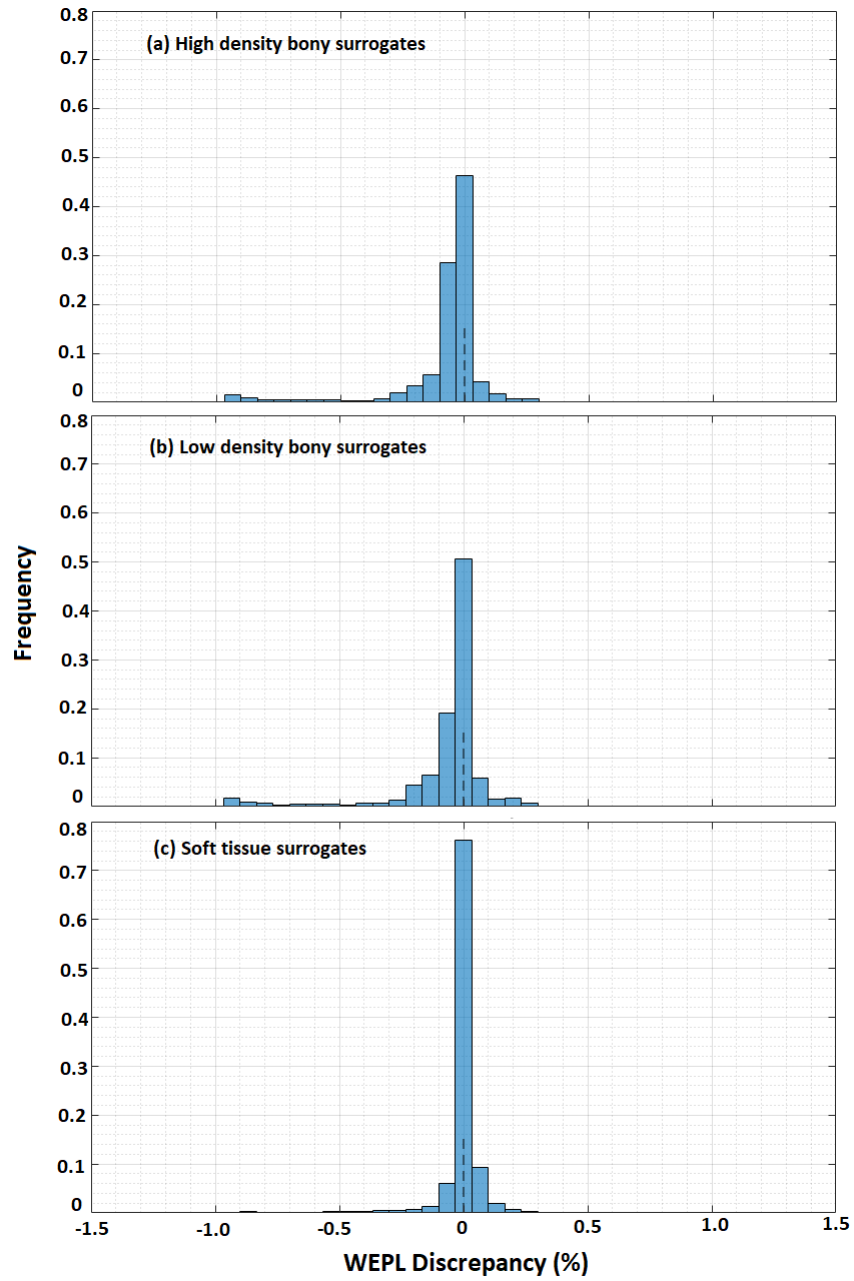


Figure 8.6: The WEPL discrepancy between the reconstructed SPR images and the theoretical SPR for (a) the two highest-density bony tissue surrogates, (b) the two lower-density bony tissue surrogates, and (c) the three soft tissue surrogates.

Table 8.3: The means of the WEPL distributions shown in Figs 8.5 and 8.6. They are very near zero.

	Experimental (%)	Theoretical (%)
High Density Bony	-0.075	-0.073
Low Density Bony	-0.066	-0.067
Soft	-0.002	-0.005

a simulated image that set every pixel inside the bottle to be the experimentally measured value of the SPR for each tissue surrogate. Figure 8.5 shows the difference between the WEPL for these two situations.

It is also useful to compare the WEPL of the reconstructed images and that of a simulated image using the theoretical values obtained from the known compositions and densities of the tissue surrogates. This case is shown in Fig. 8.6. The distributions are peaked closely around zero, indicating good agreement between the three cases. The mean values of the distributions are shown in Table 8.3. There are outliers associated with edge artifacts at the border of the bottles that are omitted from the distributions and the statistics presented in Table 8.3.

8.4 Conclusions

The JSIR-BVM has previously been shown to reconstruct SPR maps with very low error compared to theoretical values [128, 129]. This work presents a threefold comparison between SPR values for selected tissue surrogate samples calculated using a theoretical model, reconstructed using the JSIR-BVM, and directly measured using a clinical proton machine. There is good agreement between all three cases.

Chapter 9

Conclusion

The invariant-mass method is an excellent tool for assessing the structure of light particle-decaying nuclei, giving us the ability to determine the decay energy and intrinsic widths of these short-lived nuclei. In the case of $2p$ decay, we are also granted a window into the dynamics of the decay, extracting information about the type of decay (prompt vs. sequential) and determining the decay path for sequentially decaying states.

In this work, I have presented results for a number of proton-decaying nuclei. A new sequentially $2p$ -decaying state in ^{12}O was observed for the first time. The evolution in decay type for states in ^{12}O was shown, as a sequence from fully prompt to fully sequential $2p$ decay was observed with increasing decay energy. The analog states of the 4 observed peaks in the $2p+^{10}\text{C}$ were also found in the $2p+^{10}\text{B}$ decay channel of ^{12}N . The decay of these analog states mark another instance of the decay of an isobaric analog state to another isobaric analog state, a rare phenomenon. Fission-like decays were also observed for a high-lying state in ^{12}O and its analog in ^{12}N . This work also presents the first observation of the $2p$ -decaying ^{11}O , the lightest isotope of oxygen ever observed and the mirror of the classic halo nucleus ^{11}Li . The Gamow Coupled Channel model predicts four states of ^{11}O that are close together in energy that provide an excellent fit to the observed $2p$ decay energy spectrum.

The field looks forward to the experimental program of FRIB, which will provide even

more exotic and intense radioactive beams, particularly on the neutron-rich side of the chart. The invariant-mass method will continue to be important in this program as we are granted pure beams which will grant access to heavier particle-decaying nuclei on both sides of the chart.

This work also presents preliminary results for the experimental verification of a method of iteratively reconstructing proton stopping power ratios (SPR) using dual-energy CT data. This new method produces more accurate SPR maps than image-based method, and has the potential to improve dose uniformity and tissue sparing during proton radiation therapy.

Glossary

BVM: basis vector model - A parameterization of tissue properties using two dissimilar materials as a basis. The tissue is expressed as a linear combination of these materials.

DECT: dual-energy computed tomography - The use of two different energies in a computed tomography scan to extract two independent properties of scanned material.

CTV: clinical target volume - The volume containing the tumor and a margin for sub-clinical disease spread that cannot be fully imaged.

HUs: Hounsfield units - A scale for describing radiodensity. An HU is defined as

$$HU = 1000 \times \frac{\mu - \mu_{water}}{\mu_{water} - \mu_{air}}, \quad (1)$$

where μ is the average linear attenuation coefficient inside a voxel, μ_{water} is the linear attenuation coefficient of water, and μ_{air} is the linear attenuation coefficient of air. In this scale, the HU of water is 0 and the HU of air is -1000. The Hounsfield unit was initially developed in an effort to reliably compare CT data from scan-to-scan and across scanners.

SP: stopping power - The energy-dependent, material specific rate of energy loss as charged particles move through matter.

SPR: stopping power ratio - The ratio of a material's stopping power to that of water.

WEPL: water equivalent path length - The distance that is equivalent to that measured in water [133]. Calculated by taking the Radon transform of a beam path through a reconstructed SPR image.

Bibliography

- [1] TUNL Nuclear Data Evaluation Project, "Energy Level Diagram, A=11".
- [2] M. Pfützner, M. Karny, L. V. Grigorenko, and K. Riisager, "Radioactive decays at limits of nuclear stability," *Rev. Mod. Phys.*, vol. 84, pp. 567–619, Apr 2012.
- [3] L. V. Grigorenko, T. D. Wisner, K. Mercurio, R. J. Charity, R. Shane, L. G. Sobotka, J. M. Elson, A. H. Wuosmaa, A. Banu, M. McCleskey, L. Trache, R. E. Tribble, and M. V. Zhukov, "Three-body decay of ${}^6\text{Be}$," *Phys. Rev. C*, vol. 80, p. 034602, Sep 2009.
- [4] M. Pandey and S. Raghavan, "DNA double-strand break repair in mammals," *Journal of Radiation and Cancer Research*, vol. 8, no. 2, pp. 93–97, 2017.
- [5] H. Paganetti and T. Bortfeld, "Proton therapy," in *New Technologies in Radiation Oncology* (W. Schlegel, T. Bortfeld, and A.-L. Grosu, eds.), pp. 345–363, Berlin, Heidelberg: Springer Berlin Heidelberg, 2006.
- [6] G. Kohl, "The evolution and state-of-the-art principles of multislice computed tomography," *Proceedings of the American Thoracic Society*, vol. 2, pp. 470–6, 499, 02 2005.
- [7] B. Abdelwahhab, Z. Messali, and A. Elmoataz, "A novel kernel-based regularization-technique for pet image reconstruction," *Technologies*, vol. 5, p. 37, 06 2017.
- [8] I. Tanihata, H. Hamagaki, O. Hashimoto, Y. Shida, N. Yoshikawa, K. Sugimoto, O. Yamakawa, T. Kobayashi, and N. Takahashi, "Measurements of interaction cross sections

- and nuclear radii in the light p -shell region,” *Phys. Rev. Lett.*, vol. 55, pp. 2676–2679, Dec 1985.
- [9] J. Tanaka, R. Kanungo, M. Alcorta, N. Aoi, H. Bidaman, C. Burbadge, G. Christian, S. Cruz, B. Davids, A. D. Varela, J. Even, G. Hackman, M. Harakeh, J. Henderson, S. Ishimoto, S. Kaur, M. Keefe, R. Krcken, K. Leach, J. Lighthall, E. P. Rodal, J. Randhawa, P. Ruotsalainen, A. Sanetullaev, J. Smith, O. Workman, and I. Tanihata, “Halo-induced large enhancement of soft dipole excitation of ^{11}Li observed via proton inelastic scattering,” *Physics Letters B*, vol. 774, pp. 268 – 272, 2017.
- [10] I. A. Egorova, R. J. Charity, L. V. Grigorenko, Z. Chajecski, D. Coupland, J. M. Elson, T. K. Ghosh, M. E. Howard, H. Iwasaki, M. Kilburn, J. Lee, W. G. Lynch, J. Manfredi, S. T. Marley, A. Sanetullaev, R. Shane, D. V. Shetty, L. G. Sobotka, M. B. Tsang, J. Winkelbauer, A. H. Wuosmaa, M. Youngs, and M. V. Zhukov, “Democratic decay of ^6Be exposed by correlations,” *Phys. Rev. Lett.*, vol. 109, p. 202502, Nov 2012.
- [11] K. W. Brown, R. J. Charity, L. G. Sobotka, Z. Chajecski, L. V. Grigorenko, I. A. Egorova, Y. L. Parfenova, M. V. Zhukov, S. Bedoor, W. W. Buhro, J. M. Elson, W. G. Lynch, J. Manfredi, D. G. McNeel, W. Reviol, R. Shane, R. H. Showalter, M. B. Tsang, J. R. Winkelbauer, and A. H. Wuosmaa, “Observation of long-range three-body Coulomb effects in the decay of ^{16}Ne ,” *Phys. Rev. Lett.*, vol. 113, p. 232501, Dec 2014.
- [12] D. Suzuki, H. Iwasaki, D. Beaumel, M. Assié, H. Baba, Y. Blumenfeld, F. de Oliveira Santos, N. de Séréville, A. Drouart, S. Franchoo, J. Gibelin, A. Gillibert, S. Giron, S. Grévy, J. Guillot, M. Hackstein, F. Hammache, N. Keeley, V. Lapoux, F. Maréchal, A. Matta, S. Michimasa, L. Nalpas, F. Naqvi, H. Okamura, H. Otsu, J. Pancin, D. Y. Pang, L. Perrot, C. M. Petrache, E. Pollacco, A. Ramus, W. Rother, P. Roussel-Chomaz, H. Sakurai, J.-A. Scarpaci, O. Sorlin, P. C. Srivastava, I. Stefan,

- C. Stodel, Y. Tanimura, and S. Terashima, “Second 0^+ state of unbound ^{12}O : Scaling of mirror asymmetry,” *Phys. Rev. C*, vol. 93, p. 024316, Feb 2016.
- [13] R. J. Charity, S. A. Komarov, L. G. Sobotka, J. Clifford, D. Bazin, A. Gade, J. Lee, S. M. Lukyanov, W. G. Lynch, M. Mocko, S. P. Lobastov, A. M. Rogers, A. Sanetullaev, M. B. Tsang, M. S. Wallace, R. G. T. Zegers, S. Hudan, C. Metelko, M. A. Famiano, A. H. Wuosmaa, and M. J. van Goethem, “Investigation of particle-unbound excited states in light nuclei with resonance-decay spectroscopy using a ^{12}Be beam,” *Phys. Rev. C*, vol. 78, p. 054307, Nov 2008.
- [14] “Evaluated nuclear structure data file (ensdf).” <http://www.nndc.bnl.gov/ensdf/>.
- [15] Z. H. Yang, Y. L. Ye, Z. H. Li, J. L. Lou, J. S. Wang, D. X. Jiang, Y. C. Ge, Q. T. Li, H. Hua, X. Q. Li, F. R. Xu, J. C. Pei, R. Qiao, H. B. You, H. Wang, Z. Y. Tian, K. A. Li, Y. L. Sun, H. N. Liu, J. Chen, J. Wu, J. Li, W. Jiang, C. Wen, B. Yang, Y. Liu, Y. Y. Yang, P. Ma, J. B. Ma, S. L. Jin, J. L. Han, and J. Lee, “Helium-helium clustering states in ^{12}Be ,” *Phys. Rev. C*, vol. 91, p. 024304, Feb 2015.
- [16] J. Hooker, G. Rogachev, V. Goldberg, E. Koshchiy, B. Roeder, H. Jayatissa, C. Hunt, C. Magana, S. Upadhyayula, E. Uberseder, and A. Saastamoinen, “Structure of ^{10}N in $^9\text{C}+p$ resonance scattering,” *Physics Letters B*, vol. 769, pp. 62 – 66, 2017.
- [17] F. Ajzenberg-Selove, “Energy levels of light nuclei $A = 11-12$,” *Nucl. Phys. A*, vol. 506, no. 1, pp. 1 – 158, 1990.
- [18] L. G. Sobotka, W. W. Buhro, R. J. Charity, J. M. Elson, M. F. Jager, J. Manfredi, M. H. Mahzoon, A. M. Mukhamedzhanov, V. Eremenko, M. McCleskey, R. G. Pizzone, B. T. Roeder, A. Spiridon, E. Simmons, L. Trache, M. Kurokawa, and P. Navrátil, “Proton decay of excited states in ^{12}N and ^{13}O and the astrophysical $^{11}\text{C}(p,\gamma)^{12}\text{N}$ reaction rate,” *Phys. Rev. C*, vol. 87, p. 069902, Jun 2013.

- [19] S. M. Wang, W. Nazarewicz, R. J. Charity, and L. G. Sobotka, “Structure and decay of the extremely proton-rich nuclei $^{11,12}\text{O}$,” *Phys. Rev. C*, vol. 99, p. 054302, May 2019.
- [20] C. F. v. Weizsäcker, “Zur theorie der kernmassen,” *Zeitschrift für Physik*, vol. 96, pp. 431–458, Jul 1935.
- [21] R. J. Charity, L. G. Sobotka, K. Hagino, D. Bazin, M. A. Famiano, A. Gade, S. Hudan, S. A. Komarov, J. Lee, S. P. Lobastov, S. M. Lukyanov, W. G. Lynch, C. Metelko, M. Mocko, A. M. Rogers, H. Sagawa, A. Sanetullaev, M. B. Tsang, M. S. Wallace, M. J. van Goethem, and A. H. Wuosmaa, “Double isobaric analog of ^{11}Li in ^{11}B ,” *Phys. Rev. C*, vol. 86, p. 041307, Oct 2012.
- [22] V. Goldansky, “On neutron-deficient isotopes of light nuclei and the phenomena of proton and two-proton radioactivity,” *Nuclear Physics*, vol. 19, pp. 482 – 495, 1960.
- [23] H. Bethe, “Zur theorie des durchgangs schneller korpuskularstrahlen durch materie,” *Annalen der Physik*, vol. 397, no. 3, pp. 325–400, 1930.
- [24] J. L. Prince and J. M. Links, *Medical imaging signals and systems*. Pearson Education, 2015.
- [25] T. Teranishi, S. Shimoura, Y. Ando, M. Hirai, N. Iwasa, T. Kikuchi, S. Moriya, T. Motobayashi, H. Murakami, T. Nakamura, T. Nishio, H. Sakurai, T. Uchibori, Y. Watanabe, Y. Yanagisawa, and M. Ishihara, “Isobaric analog state of ^{11}Li ,” *Physics Letters B*, vol. 407, no. 2, pp. 110 – 114, 1997.
- [26] D. Morrissey, B. Sherrill, M. Steiner, A. Stolz, and I. Wiedenhoever, “Commissioning the A1900 projectile fragment separator,” *Nuclear Instruments and Methods in Physics Research Section B: Beam Interactions with Materials and Atoms*, vol. 204, pp. 90 – 96, 2003. 14th International Conference on Electromagnetic Isotope Separators and Techniques Related to their Applications.

- [27] D. Bazin, V. Andreev, A. Becerril, M. Dolans, P. Mantica, J. Ottarson, H. Schatz, J. Stoker, and J. Vincent, “Radio frequency fragment separator at NSCL,” *Nuclear Instruments and Methods in Physics Research Section A: Accelerators, Spectrometers, Detectors and Associated Equipment*, vol. 606, no. 3, pp. 314 – 319, 2009.
- [28] R. J. Charity, K. W. Brown, J. Elson, W. Reviol, L. G. Sobotka, W. W. Buhro, Z. Chajewski, W. G. Lynch, J. Manfredi, R. Shane, R. H. Showalter, M. B. Tsang, D. Weisshaar, J. Winkelbauer, S. Bedoor, D. G. McNeel, and A. H. Wuosmaa, “Invariant-mass spectroscopy of ^{18}Ne , ^{16}O , and ^{10}C excited states formed in neutron-transfer reactions,” *Phys. Rev. C*, vol. 99, p. 044304, Apr 2019.
- [29] M. Wallace, M. Famiano, M.-J. van Goethem, A. Rogers, W. Lynch, J. Clifford, F. De-launay, J. Lee, S. Labostov, M. Mocko, L. Morris, A. Moroni, B. Nett, D. Oostdyk, R. Krishnasamy, M. Tsang, R. de Souza, S. Hudan, L. Sobotka, R. Charity, J. Elson, and G. Engel, “The high resolution array (hira) for rare isotope beam experiments,” *Nuclear Instruments and Methods in Physics Research Section A: Accelerators, Spectrometers, Detectors and Associated Equipment*, vol. 583, no. 2, pp. 302 – 312, 2007.
- [30] <http://www.micronsemiconductor.co.uk/>.
- [31] A. M. Poskanzer, S. W. Cosper, E. K. Hyde, and J. Cerny, “New isotopes: ^{11}Li , ^{14}B , and ^{15}B ,” *Phys. Rev. Lett.*, vol. 17, pp. 1271–1274, Dec 1966.
- [32] P. G. Hansen and B. Jonson, “The neutron halo of extremely neutron-rich nuclei,” *EPL (Europhysics Letters)*, vol. 4, no. 4, p. 409, 1987.
- [33] M. Smith, M. Brodeur, T. Brunner, S. Ettenauer, A. Lapierre, R. Ringle, V. L. Ryjkov, F. Ames, P. Bricault, G. W. F. Drake, P. Delheij, D. Lunney, F. Sarazin, and J. Dilling, “First penning-trap mass measurement of the exotic halo nucleus ^{11}Li ,” *Phys. Rev. Lett.*, vol. 101, p. 202501, Nov 2008.

- [34] C. Bachelet, G. Audi, C. Gaulard, C. Guénaut, F. Herfurth, D. Lunney, M. de Saint Simon, and C. Thibault, “New binding energy for the two-neutron halo of ^{11}Li ,” *Phys. Rev. Lett.*, vol. 100, p. 182501, May 2008.
- [35] C. Bachelet, G. Audi, C. Gaulard, C. Guenaut, F. Herfurth, D. Lunney, M. De Saint-Simon, and C. Thibault, “Mass measurement of short-lived halo nuclides,” *European Physical Journal A*, vol. 25, 09 2005.
- [36] T. Kobayashi, O. Yamakawa, K. Omata, K. Sugimoto, T. Shimoda, N. Takahashi, and I. Tanihata, “Projectile fragmentation of the extremely neutron-rich nucleus ^{11}Li at 0.79 gev/nucleon,” *Phys. Rev. Lett.*, vol. 60, pp. 2599–2602, Jun 1988.
- [37] J. Hüfner and M. C. Nemes, “Relativistic heavy ions measure the momentum distribution on the nuclear surface,” *Phys. Rev. C*, vol. 23, pp. 2538–2547, Jun 1981.
- [38] T. Moriguchi, A. Ozawa, S. Ishimoto, Y. Abe, M. Fukuda, I. Hachiuma, Y. Ishibashi, Y. Ito, T. Kuboki, M. Lantz, D. Nagae, K. Namihira, D. Nishimura, T. Ohtsubo, H. Ooishi, T. Suda, H. Suzuki, T. Suzuki, M. Takechi, K. Tanaka, and T. Yamaguchi, “Density distributions of ^{11}Li deduced from reaction cross-section measurements,” *Phys. Rev. C*, vol. 88, p. 024610, Aug 2013.
- [39] R. Sánchez, W. Nörtershäuser, G. Ewald, D. Albers, J. Behr, P. Bricault, B. A. Bushaw, A. Dax, J. Dilling, M. Dombisky, G. W. F. Drake, S. Götte, R. Kirchner, H.-J. Kluge, T. Kühl, J. Lassen, C. D. P. Levy, M. R. Pearson, E. J. Prime, V. Ryjkov, A. Wojtaszek, Z.-C. Yan, and C. Zimmermann, “Nuclear charge radii of $^{9,11}\text{Li}$: The influence of halo neutrons,” *Phys. Rev. Lett.*, vol. 96, p. 033002, Jan 2006.
- [40] I. J. Thompson and M. V. Zhukov, “Effects of ^{10}Li virtual states on the structure of ^{11}Li ,” *Phys. Rev. C*, vol. 49, pp. 1904–1907, Apr 1994.
- [41] H. Simon, D. Aleksandrov, T. Aumann, L. Axelsson, T. Baumann, M. J. G. Borge, L. V. Chulkov, R. Collatz, J. Cub, W. Dostal, B. Eberlein, T. W. Elze, H. Emling,

- H. Geissel, A. Grünschloss, M. Hellström, J. Holeczek, R. Holzmann, B. Jonson, J. V. Kratz, G. Kraus, R. Kulesa, Y. Leifels, A. Leistenschneider, T. Leth, I. Mukha, G. Münzenberg, F. Nickel, T. Nilsson, G. Nyman, B. Petersen, M. Pfützner, A. Richter, K. Riisager, C. Scheidenberger, G. Schrieder, W. Schwab, M. H. Smedberg, J. Stroth, A. Surowiec, O. Tengblad, and M. V. Zhukov, “Direct experimental evidence for strong admixture of different parity states in ^{11}Li ,” *Phys. Rev. Lett.*, vol. 83, pp. 496–499, Jul 1999.
- [42] H. Esbensen, K. Hagino, P. Mueller, and H. Sagawa, “Charge radius and dipole response of ^{11}Li ,” *Phys. Rev. C*, vol. 76, p. 024302, Aug 2007.
- [43] E. Garrido, D. V. Fedorov, and A. S. Jensen, “Angular correlations in breakup of three-body halo nuclei,” *Phys. Rev. C*, vol. 58, pp. R2654–R2658, Nov 1998.
- [44] N. Shulgina, B. Jonson, and M. Zhukov, “ ^{11}Li structure from experimental data,” *Nuclear Physics A*, vol. 825, no. 3, pp. 175 – 199, 2009.
- [45] A. Korshennikov, E. Kuzmin, E. Nikolskii, C. Bertulani, O. Bochkarev, S. Fukuda, T. Kobayashi, S. Momota, B. Novatskii, A. Ogloblin, A. Ozawa, V. Pribora, I. Tanihata, and K. Yoshida, “Elastic and inelastic scattering of exotic nuclei,” *Nuclear Physics A*, vol. 616, no. 1, pp. 189 – 200, 1997. Radioactive Nuclear Beams.
- [46] M. Zinser, F. Humbert, T. Nilsson, W. Schwab, H. Simon, T. Aumann, M. Borge, L. Chulkov, J. Cub, T. Elze, H. Emling, H. Geissel, D. Guillemaud-Mueller, P. Hansen, R. Holzmann, H. Irnich, B. Jonson, J. Kratz, R. Kulesa, Y. Leifels, H. Lenske, A. Magel, A. Mueller, G. Mnzenberg, F. Nickel, G. Nyman, A. Richter, K. Riisager, C. Scheidenberger, G. Schrieder, K. Stelzer, J. Stroth, A. Surowiec, O. Tengblad, E. Wajda, and E. Zude, “Invariant-mass spectroscopy of ^{10}Li and ^{11}Li ,” *Nuclear Physics A*, vol. 619, no. 1, pp. 151 – 176, 1997.

- [47] H. Simon, M. Meister, T. Aumann, M. Borge, L. Chulkov, U. D. Pramanik, T. Elze, H. Emling, C. Forssn, H. Geissel, M. Hellstrm, B. Jonson, J. Kratz, R. Kulesa, Y. Leifels, K. Markenroth, G. Mnzenberg, F. Nickel, T. Nilsson, G. Nyman, A. Richter, K. Riisager, C. Scheidenberger, G. Schrieder, O. Tengblad, and M. Zhukov, “Systematic investigation of the drip-line nuclei ^{11}Li and ^{14}Be and their unbound subsystems ^{10}Li and ^{13}Be ,” *Nuclear Physics A*, vol. 791, no. 3, pp. 267 – 302, 2007.
- [48] M. Gornov, Y. Gurov, S. Lapushkin, P. Morokhov, V. Pechkurov, T. Pedlar, K. Seth, J. Wise, and D. Zhao, “Excited states of ^{11}Li ,” *Physical Review Letters*, vol. 81, pp. 4325–4328, 11 1998.
- [49] H. T. Fortune, “Structure of $^{11}\text{Li}(\text{g.s.})$ and an excited $3/2^-$ state,” *Phys. Rev. C*, vol. 91, p. 017303, Jan 2015.
- [50] B. A. Chernyshev, Y. B. Gurov, V. S. Karpukhin, L. Y. Korotkova, S. V. Lapushkin, R. V. Pritula, and V. G. Sandukovsky, “Spectroscopy of the heavy lithium isotopes $^{10-12}\text{Li}$,” *The European Physical Journal A*, vol. 49, p. 68, Jun 2013.
- [51] I. Tanihata, “Neutron halo nuclei,” *Journal of Physics G: Nuclear and Particle Physics*, vol. 22, no. 2, p. 157, 1996.
- [52] K. Hagino and H. Sagawa, “Pairing correlations in nuclei on the neutron-drip line,” *Phys. Rev. C*, vol. 72, p. 044321, Oct 2005.
- [53] M. F. Jager, R. J. Charity, J. M. Elson, J. Manfredi, M. H. Mahzoon, L. G. Sobotka, M. McCleskey, R. G. Pizzone, B. T. Roeder, A. Spiridon, E. Simmons, L. Trache, and M. Kurokawa, “Two-proton decay of ^{12}O and its isobaric analog state in ^{12}N ,” *Phys. Rev. C*, vol. 86, p. 011304, Jul 2012.
- [54] N. Michel, W. Nazarewicz, M. Poszajczak, and T. Vertse, “Shell model in the complex energy plane,” *Journal of Physics G: Nuclear and Particle Physics*, vol. 36, no. 1, p. 013101, 2009.

- [55] N. Michel, W. Nazarewicz, J. Okolowicz, and M. Poszajczak, “Open problems in the theory of nuclear open quantum systems,” *Journal of Physics G: Nuclear and Particle Physics*, vol. 37, no. 6, p. 064042, 2010.
- [56] L. V. Grigorenko, I. G. Mukha, I. J. Thompson, and M. V. Zhukov, “Two-proton widths of ^{12}o , ^{16}ne , and three-body mechanism of thomas-ehrmann shift,” *Phys. Rev. Lett.*, vol. 88, p. 042502, Jan 2002.
- [57] N. Michel, W. Nazarewicz, and M. Płoszajczak, “Isospin mixing and the continuum coupling in weakly bound nuclei,” *Phys. Rev. C*, vol. 82, p. 044315, Oct 2010.
- [58] H. T. Fortune and R. Sherr, “Potential-model estimate of the mass of $^{11}O_{g.s.}$,” *Phys. Rev. C*, vol. 88, p. 034326, Sep 2013.
- [59] F. C. Barker, “ ^{12}O ground-state decay by 2He emission,” *Phys. Rev. C*, vol. 63, p. 047303, Mar 2001.
- [60] H. T. Fortune, “Energy and width of $^{11}O(g.s.)$,” *Phys. Rev. C*, vol. 99, p. 051302, May 2019.
- [61] S. M. Wang, N. Michel, W. Nazarewicz, and F. R. Xu, “Structure and decays of nuclear three-body systems: The gamow coupled-channel method in jacobi coordinates,” *Phys. Rev. C*, vol. 96, p. 044307, Oct 2017.
- [62] S. M. Wang and W. Nazarewicz, “Puzzling two-proton decay of ^{67}Kr ,” *Phys. Rev. Lett.*, vol. 120, p. 212502, May 2018.
- [63] M. F. de la Ripelle, “The potential harmonic expansion method,” *Annals of Physics*, vol. 147, no. 2, pp. 281 – 320, 1983.
- [64] A. Kievsky, S. Rosati, M. Viviani, L. E. Marcucci, and L. Girlanda, “A high-precision variational approach to three- and four-nucleon bound and zero-energy scattering

- states,” *Journal of Physics G: Nuclear and Particle Physics*, vol. 35, p. 063101, may 2008.
- [65] D. Thompson, M. Lemere, and Y. Tang, “Systematic investigation of scattering problems with the resonating-group method,” *Nuclear Physics A*, vol. 286, no. 1, pp. 53 – 66, 1977.
- [66] S. Cwiok, J. Dudek, W. Nazarewicz, J. Skalski, and T. Werner, “Single-particle energies, wave functions, quadrupole moments and g-factors in an axially deformed woods-saxon potential with applications to the two-centre-type nuclear problems,” *Computer Physics Communications*, vol. 46, no. 3, pp. 379 – 399, 1987.
- [67] R. G. Thomas, “On the determination of reduced widths from the one-level dispersion formula,” *Phys. Rev.*, vol. 81, pp. 148–149, Jan 1951.
- [68] J. B. Ehrman, “On the displacement of corresponding energy levels of ^{13}C and ^{13}N ,” *Phys. Rev.*, vol. 81, pp. 412–416, Feb 1951.
- [69] N. Auerbach and N. Vinh Mau, “About coulomb energy shifts in halo nuclei,” *Phys. Rev. C*, vol. 63, p. 017301, Dec 2000.
- [70] K. Fosse, W. Nazarewicz, Y. Jaganathen, N. Michel, and M. Płoszajczak, “Nuclear rotation in the continuum,” *Phys. Rev. C*, vol. 93, p. 011305, Jan 2016.
- [71] R. IdBetan, R. Liotta, N. Sandulescu, and T. Vertse, “A shell model representation with antibound states,” *Physics Letters B*, vol. 584, no. 1, pp. 48 – 57, 2004.
- [72] N. Michel, W. Nazarewicz, M. Płoszajczak, and J. Rotureau, “Antibound states and halo formation in the gamow shell model,” *Phys. Rev. C*, vol. 74, p. 054305, Nov 2006.
- [73] J. Smith, T. Baumann, D. Bazin, J. Brown, P. DeYoung, N. Frank, M. Jones, Z. Kohley, B. Luther, B. Marks, A. Spyrou, S. Stephenson, M. Thoennessen, and A. Volya,

- “Neutron correlations in the decay of the first excited state of ^{11}Li ,” *Nuclear Physics A*, vol. 955, pp. 27 – 40, 2016.
- [74] R. Kanungo, A. Sanetullaev, J. Tanaka, S. Ishimoto, G. Hagen, T. Myo, T. Suzuki, C. Andreoiu, P. Bender, A. A. Chen, B. Davids, J. Fallis, J. P. Fortin, N. Galinski, A. T. Gallant, P. E. Garrett, G. Hackman, B. Hadinia, G. Jansen, M. Keefe, R. Krücken, J. Lighthall, E. McNeice, D. Miller, T. Otsuka, J. Purcell, J. S. Randhawa, T. Roger, A. Rojas, H. Savajols, A. Shotter, I. Tanihata, I. J. Thompson, C. Unsworth, P. Voss, and Z. Wang, “Evidence of soft dipole resonance in ^{11}Li with isoscalar character,” *Phys. Rev. Lett.*, vol. 114, p. 192502, May 2015.
- [75] S. A. Sofianos, S. A. Rakityansky, and G. P. Vermaak, “Subthreshold resonances in few-neutron systems,” *Journal of Physics G: Nuclear and Particle Physics*, vol. 23, no. 11, p. 1619, 1997.
- [76] A. M. Mukhamedzhanov, B. F. Irgaziev, V. Z. Goldberg, Y. V. Orlov, and I. Qazi, “Bound, virtual, and resonance s -matrix poles from the schrödinger equation,” *Phys. Rev. C*, vol. 81, p. 054314, May 2010.
- [77] V.D. Efros and J.M. Bang, “The first excited states of ^9Be and ^9B ,” *Eur. Phys. J. A*, vol. 4, no. 1, pp. 33–39, 1999.
- [78] J. Okołowicz, M. Płoszajczak, and W. Nazarewicz, “On the origin of nuclear clustering,” *Prog. Theor. Phys. Supp.*, vol. 196, pp. 230–243, 2012.
- [79] L. V. Grigorenko, I. G. Mukha, I. J. Thompson, and M. V. Zhukov, “Two-proton widths of ^{12}O , ^{16}Ne , and three-body mechanism of Thomas-Ehrman shift,” *Phys. Rev. Lett.*, vol. 88, p. 042502, Jan 2002.
- [80] N. Michel, W. Nazarewicz, and M. Płoszajczak, “Isospin mixing and the continuum coupling in weakly bound nuclei,” *Phys. Rev. C*, vol. 82, p. 044315, Oct 2010.

- [81] R. A. Kryger, A. Azhari, M. Hellström, J. H. Kelley, T. Kubo, R. Pfaff, E. Ramakrishnan, B. M. Sherrill, M. Thoennessen, S. Yokoyama, R. J. Charity, J. Dempsey, A. Kirov, N. Robertson, D. G. Sarantites, L. G. Sobotka, and J. A. Winger, “Two-proton emission from the ground state of ^{12}O ,” *Phys. Rev. Lett.*, vol. 74, pp. 860–863, Feb 1995.
- [82] R. J. Charity, J. M. Elson, J. Manfredi, R. Shane, L. G. Sobotka, B. A. Brown, Z. Chajecki, D. Coupland, H. Iwasaki, M. Kilburn, J. Lee, W. G. Lynch, A. Sanetullaev, M. B. Tsang, J. Winkelbauer, M. Youngs, S. T. Marley, D. V. Shetty, A. H. Wuosmaa, T. K. Ghosh, and M. E. Howard, “Investigations of three-, four-, and five-particle decay channels of levels in light nuclei created using a ^9C beam,” *Phys. Rev. C*, vol. 84, p. 014320, Jul 2011.
- [83] K. W. Brown, W. W. Buhro, R. J. Charity, J. M. Elson, W. Reviol, L. G. Sobotka, Z. Chajecki, W. G. Lynch, J. Manfredi, R. Shane, R. H. Showalter, M. B. Tsang, D. Weisshaar, J. R. Winkelbauer, S. Bedoor, and A. H. Wuosmaa, “Two-proton decay from the isobaric analog state in ^8B ,” *Phys. Rev. C*, vol. 90, p. 027304, Aug 2014.
- [84] Fortune, H. T., “Nature of the $E_n = 1.24$ MeV state in ^{12}Be ,” *Eur. Phys. J. A*, vol. 52, no. 1, p. 11, 2016.
- [85] H. T. Fortune, “Splitting of strengths in neutron removal from ^{13}O ,” *Journal of Physics G: Nuclear and Particle Physics*, vol. 43, no. 11, p. 115102, 2016.
- [86] H. T. Fortune and R. Sherr, “Structure of $2^+, T = 2$ states in $A = 12$ nuclei,” *Phys. Rev. C*, vol. 83, p. 044313, Apr 2011.
- [87] R. J. Charity, J. M. Elson, J. Manfredi, R. Shane, L. G. Sobotka, Z. Chajecki, D. Coupland, H. Iwasaki, M. Kilburn, J. Lee, W. G. Lynch, A. Sanetullaev, M. B. Tsang, J. Winkelbauer, M. Youngs, S. T. Marley, D. V. Shetty, A. H. Wuosmaa, T. K. Ghosh,

- and M. E. Howard, “Isobaric multiplet mass equation for $A = 7$ and 8 ,” *Phys. Rev. C*, vol. 84, p. 051308, Nov 2011.
- [88] R. J. Charity, K. Mercurio, L. G. Sobotka, J. M. Elson, M. Famiano, A. Banu, C. Fu, L. Trache, and R. E. Tribble, “Decay of ^{10}C excited states above the $2p + 2\alpha$ threshold and the contribution from “democratic” two-proton emission,” *Phys. Rev. C*, vol. 75, p. 051304, May 2007.
- [89] M. Wang, G. Audi, F. Kondev, W. J. Huang, S. Naimi, and Xing Xu, “The AME2016 atomic mass evaluation (II). tables, graphs and references,” *Chin. Phys. C*, vol. 41, p. 030003, 2017.
- [90] L. V. Grigorenko and M. V. Zhukov, “Two-proton radioactivity and three-body decay. II. exploratory studies of lifetimes and correlations,” *Phys. Rev. C*, vol. 68, p. 054005, Nov 2003.
- [91] L. V. Grigorenko, T. D. Wiser, K. Mercurio, R. J. Charity, R. Shane, L. G. Sobotka, J. M. Elson, A. H. Wuosmaa, A. Banu, M. McCleskey, L. Trache, R. E. Tribble, and M. V. Zhukov, “Three-body decay of ^6Be ,” *Phys. Rev. C*, vol. 80, p. 034602, Sep 2009.
- [92] A. M. Lane and R. G. Thomas, “R-matrix theory of nuclear reactions,” *Rev. Mod. Phys.*, vol. 30, pp. 257–353, Apr 1958.
- [93] K. W. Brown, R. J. Charity, L. G. Sobotka, L. V. Grigorenko, T. A. Golubkova, S. Bedoor, W. W. Buhro, Z. Chajecski, J. M. Elson, W. G. Lynch, J. Manfredi, D. G. McNeel, W. Reviol, R. Shane, R. H. Showalter, M. B. Tsang, J. R. Winkelbauer, and A. H. Wuosmaa, “Interplay between sequential and prompt two-proton decay from the first excited state of ^{16}Ne ,” *Phys. Rev. C*, vol. 92, p. 034329, Sep 2015.
- [94] R. J. Charity, K. W. Brown, J. Okołowicz, M. Płoszajczak, J. M. Elson, W. Reviol, L. G. Sobotka, W. W. Buhro, Z. Chajecski, W. G. Lynch, J. Manfredi, R. Shane,

- R. H. Showalter, M. B. Tsang, D. Weisshaar, J. R. Winkelbauer, S. Bedoor, and A. H. Wuosmaa, “Spin alignment following inelastic scattering of ^{17}Ne , lifetime of ^{16}F , and its constraint on the continuum coupling strength,” *Phys. Rev. C*, vol. 97, p. 054318, May 2018.
- [95] L. Axelsson, M. J. G. Borge, S. Fayans, V. Z. Goldberg, S. Grévy, D. Guillemaud-Mueller, B. Jonson, K. M. Källman, T. Lönnroth, M. Lewitowicz, P. Manngård, K. Markenroth, I. Martel, A. C. Mueller, I. Mukha, T. Nilsson, G. Nyman, N. A. Orr, K. Riisager, G. V. Rogatchev, M. G. Saint-Laurent, I. N. Serikov, O. Sorlin, O. Tengblad, F. Wenander, J. S. Winfield, and R. Wolski, “Study of the unbound nucleus ^{11}N by elastic resonance scattering,” *Phys. Rev. C*, vol. 54, pp. R1511–R1514, Oct 1996.
- [96] J. M. Oliveira, A. Lépine-Szily, H. G. Bohlen, A. N. Ostrowski, R. Lichtenthäler, A. Di Pietro, A. M. Laird, G. F. Lima, L. Maunoury, F. de Oliveira Santos, P. Roussel-Chomaz, H. Savajols, W. Trinder, A. C. C. Villari, and A. de Vismes, “Observation of the ^{11}N ground state,” *Phys. Rev. Lett.*, vol. 84, pp. 4056–4059, May 2000.
- [97] E. Casarejos, C. Angulo, P. J. Woods, F. C. Barker, P. Descouvemont, M. Aliotta, T. Davinson, P. Demaret, M. Gaeleens, P. Leleux, Z. Liu, M. Loiselet, A. S. Murphy, A. Ninane, I. A. Roberts, G. Ryckewaert, J. S. Schweitzer, and F. Vanderbist, “Low-lying states in the unbound ^{11}N nucleus,” *Phys. Rev. C*, vol. 73, p. 014319, Jan 2006.
- [98] R. J. Charity, J. M. Elson, J. Manfredi, R. Shane, L. G. Sobotka, B. A. Brown, Z. Chajecki, D. Coupland, H. Iwasaki, M. Kilburn, *et al.*, “Investigations of three-, four-, and five-particle decay channels of levels in light nuclei created using a ^9C beam,” *Phys. Rev. C*, vol. 84, p. 014320, Jul 2011.
- [99] W. Benenson and E. Kashy, “Isobaric quartets in nuclei,” *Rev. Mod. Phys.*, vol. 51, pp. 527–540, Jul 1979.

- [100] Y. H. Lam, B. Blank, N. A. Smirnova, J. B. Bueb, and M. S. Antony, “The isobaric multiplet mass equation for $A=71$ revisited,” *At. Data Nucl. Tables*, vol. 99, no. 6, pp. 680 – 703, 2013.
- [101] J. Britz, A. Pape, and M. Antony, “Coefficients of the isobaric mass equation and their correlations with various nuclear parameters,” *At. Data Nucl. Tables*, vol. 69, no. 1, pp. 125 – 159, 1998.
- [102] M. Freer, E. Casarejos, L. Achouri, C. Angulo, N. I. Ashwood, N. Curtis, P. Demaret, C. Harlin, B. Laurent, M. Milin, N. A. Orr, D. Price, R. Raabe, N. Soić, and V. A. Ziman, “ $\alpha : 2n : \alpha$ molecular band in ^{10}Be ,” *Phys. Rev. Lett.*, vol. 96, p. 042501, Jan 2006.
- [103] R. J. Charity, S. A. Komarov, L. G. Sobotka, J. Clifford, D. Bazin, A. Gade, J. Lee, S. M. Lukyanov, W. G. Lynch, M. Mocko, S. P. Lobastov, A. M. Rogers, A. Sanetullaev, M. B. Tsang, M. S. Wallace, S. Hudan, C. Metelko, M. A. Famiano, A. H. Wuosmaa, and M. J. v. Goethem, “Particle decay of ^{12}Be excited states,” *Phys. Rev. C*, vol. 76, p. 064313, Dec 2007.
- [104] Z. H. Yang, Y. L. Ye, Z. H. Li, J. L. Lou, J. S. Wang, D. X. Jiang, Y. C. Ge, Q. T. Li, H. Hua, X. Q. Li, F. R. Xu, J. C. Pei, R. Qiao, H. B. You, H. Wang, Z. Y. Tian, K. A. Li, Y. L. Sun, H. N. Liu, J. Chen, J. Wu, J. Li, W. Jiang, C. Wen, B. Yang, Y. Y. Yang, P. Ma, J. B. Ma, S. L. Jin, J. L. Han, and J. Lee, “Observation of enhanced monopole strength and clustering in ^{12}Be ,” *Phys. Rev. Lett.*, vol. 112, p. 162501, Apr 2014.
- [105] M. Chartier, J. Beene, B. Blank, L. Chen, A. Galonsky, N. Gan, K. Govaert, P. Hansen, J. Kruse, V. Maddalena, M. Thoennessen, and R. Varner, “Identification of the ^{10}Li ground state,” *Physics Letters B*, vol. 510, no. 1, pp. 24 – 28, 2001.

- [106] M. Cavallaro, M. De Napoli, F. Cappuzzello, S. E. A. Orrigo, C. Agodi, M. Bondí, D. Carbone, A. Cunsolo, B. Davids, T. Davinson, A. Foti, N. Galinski, R. Kanungo, H. Lenske, C. Ruiz, and A. Sanetullaev, “Investigation of the ^{10}Li shell inversion by neutron continuum transfer reaction,” *Phys. Rev. Lett.*, vol. 118, p. 012701, Jan 2017.
- [107] T. B. Webb, S. M. Wang, K. W. Brown, R. J. Charity, J. M. Elson, J. Barney, G. Cerizza, Z. Chajeki, J. Estee, D. E. M. Hoff, S. A. Kuvin, W. G. Lynch, J. Manfredi, D. McNeel, P. Morfouace, W. Nazarewicz, C. D. Pruitt, C. Santamaria, J. Smith, L. G. Sobotka, S. Sweany, C. Y. Tsang, M. B. Tsang, A. H. Wuosmaa, Y. Zhang, and K. Zhu, “First observation of unbound ^{11}O , the mirror of the halo nucleus ^{11}Li ,” *Phys. Rev. Lett.*, vol. 122, p. 122501, Mar 2019.
- [108] J. H. Kelley, J. E. Purcell, and S. C. G., “Energy levels of light nuclei $A = 12$,” *Nucl. Phys. A*, vol. 968, p. 71, 2017.
- [109] D. R. Tilley *et al.*, “Energy levels of light nuclei $A = 8, 9, 10$,” *Nucl. Phys. A*, vol. 745, p. 155, 2004.
- [110] G. V. Rogachev *et al.*, “Proton elastic scattering from ^7Be at low energies,” *Phys. Rev. C*, vol. 64, p. 061601, 2001.
- [111] S. N. Paneru *et al.*, “s-wave scattering lengths for the $^7\text{Be}+p$ system from an R-matrix analysis,” *Phys. Rev. C*, vol. 99, p. 045807, 2019.
- [112] L. W. Nordheim *Rev. Mod. Phys.*, vol. 23, p. 322, 1951.
- [113] M. H. Brennan and A. M. Bernstein, “jj coupling model in odd-odd nuclei,” *Phys. Rev.*, vol. 120, pp. 927–933, Nov 1960.
- [114] L. V. Grigorenko, I. A. Egorova, R. J. Charity, and M. V. Zhukov, “Sensitivity of three-body decays to the reactions mechanism and the initial structure by example of ^6Be ,” *Phys. Rev. C*, vol. 86, p. 061602, Dec 2012.

- [115] M. F. Moyers, D. W. Miller, D. A. Bush, and J. D. Slater, “Methodologies and tools for proton beam design for lung tumors,” *International Journal of Radiation Oncology*Biography*Physics*, vol. 49, no. 5, pp. 1429 – 1438, 2001.
- [116] H. Paganetti, “Range uncertainties in proton therapy and the role of monte carlo simulations,” *Physics in Medicine and Biology*, vol. 57, pp. R99–R117, may 2012.
- [117] P. C. Park, X. R. Zhu, A. K. Lee, N. Sahoo, A. D. Melancon, L. Zhang, and L. Dong, “A beam-specific planning target volume (ptv) design for proton therapy to account for setup and range uncertainties,” *International Journal of Radiation Oncology*Biography*Physics*, vol. 82, no. 2, pp. e329 – e336, 2012.
- [118] M. Yang, G. Virshup, J. Clayton, X. R. Zhu, R. Mohan, and L. Dong, “Theoretical variance analysis of single- and dual-energy computed tomography methods for calculating proton stopping power ratios of biological tissues,” *Physics in Medicine and Biology*, vol. 55, pp. 1343–1362, feb 2010.
- [119] M. Yang, X. R. Zhu, P. C. Park, U. Titt, R. Mohan, G. Virshup, J. E. Clayton, and L. Dong, “Comprehensive analysis of proton range uncertainties related to patient stopping-power-ratio estimation using the stoichiometric calibration,” *Physics in Medicine and Biology*, vol. 57, pp. 4095–4115, jun 2012.
- [120] N. Hnemohr, H. Paganetti, S. Greulich, O. Jkel, and J. Seco, “Tissue decomposition from dual energy ct data for mc based dose calculation in particle therapy,” *Medical Physics*, vol. 41, no. 6Part1, p. 061714, 2014.
- [121] U. Schneider, E. Pedroni, and A. Lomax, “The calibration of CT hounsfield units for radiotherapy treatment planning,” *Physics in Medicine and Biology*, vol. 41, pp. 111–124, jan 1996.

- [122] J.-. Tremblay, S. Bedwani, and H. Bouchard, “A theoretical comparison of tissue parameter extraction methods for dual energy computed tomography,” *Medical Physics*, vol. 41, no. 8Part1, p. 081905, 2014.
- [123] G. Vilches-Freixas, J. M. Ltang, N. Ducros, and S. Rit, “Optimization of dual-energy CT acquisitions for proton therapy using projection-based decomposition,” *Medical Physics*, vol. 44, no. 9, pp. 4548–4558, 2017.
- [124] J. F. Williamson, S. Li, S. Devic, B. R. Whiting, and F. A. Lerma, “On two-parameter models of photon cross sections: Application to dual-energy ct imaging,” *Medical Physics*, vol. 33, no. 11, pp. 4115–4129, 2006.
- [125] D. Han, J. V. Siebers, and J. F. Williamson, “A linear, separable two-parameter model for dual energy CT imaging of proton stopping power computation,” *Medical Physics*, vol. 43, no. 1, pp. 600–612, 2016.
- [126] D. Han, M. A. Porras-Chaverri, J. A. O’Sullivan, D. G. Politte, and J. F. Williamson, “Technical note: On the accuracy of parametric two-parameter photon cross-section models in dual-energy ct applications,” *Medical Physics*, vol. 44, no. 6, pp. 2438–2446, 2017.
- [127] J. A. O’Sullivan and J. Benac, “Alternating minimization algorithms for transmission tomography,” *IEEE Transactions on Medical Imaging*, vol. 26, pp. 283–297, March 2007.
- [128] S. Zhang, D. Han, D. G. Politte, J. F. Williamson, and J. A. O’Sullivan, “Impact of joint statistical dual-energy CT reconstruction of proton stopping power images: Comparison to image- and sinogram-domain material decomposition approaches,” *Medical Physics*, vol. 45, no. 5, pp. 2129–2142, 2018.
- [129] S. Zhang, D. Han, J. F. Williamson, T. Zhao, D. G. Politte, B. R. Whiting, and J. A. OSullivan, “Experimental implementation of a joint statistical image reconstruc-

- tion method for proton stopping power mapping from dual-energy ct data,” *Medical Physics*, vol. 46, no. 1, pp. 273–285, 2019.
- [130] G. M. Lasio, B. R. Whiting, and J. F. Williamson, “Statistical reconstruction for x-ray computed tomography using energy-integrating detectors,” *Physics in Medicine and Biology*, vol. 52, pp. 2247–2266, apr 2007.
- [131] I. Csiszar, “Why least squares and maximum entropy? an axiomatic approach to inference for linear inverse problems,” *Ann. Statist.*, vol. 19, pp. 2032–2066, 12 1991.
- [132] J. D. Evans, B. R. Whiting, J. A. OSullivan, D. G. Politte, P. H. Klahr, Y. Yu, and J. F. Williamson, “Prospects for in vivo estimation of photon linear attenuation coefficients using postprocessing dual-energy CT imaging on a commercial scanner: Comparison of analytic and polyenergetic statistical reconstruction algorithms,” *Medical Physics*, vol. 40, no. 12, p. 121914, 2013.
- [133] C. Ma and L. Wang, *Equivalent Path Length*, pp. 224–224. Berlin, Heidelberg: Springer Berlin Heidelberg, 2013.